HELIUM DROPLETS: UNIQUE NANOREACTORS FOR THE INVESTIGATION OF MOLECULAR DOPANTS

Thesis submitted for the degree of

Doctor of Philosophy

at the University of Leicester

by

Benjamin Shepperson MChem (Leicester)

Department of Chemistry

University of Leicester

December 2012

HELIUM DROPLETS: UNIQUE NANOREACTORS FOR THE

INVESTIGATION OF MOLECULAR DOPANTS

Benjamin Shepperson

ABSTRACT

Both pulsed and continuous sources of helium nanodroplets were employed for the investigation of molecular dopants. The doped helium droplets were investigated with the use of a range of techniques including electron impact ionization mass spectrometry, electronic spectroscopy and infrared (vibrational) spectroscopy.

Electron impact mass spectrometry was used to investigate the influence of droplet size ($<N> = 4000 - 80\ 000$ helium atoms) and dopant species on the formation of helium cluster cations. The abundance of larger helium cluster cations, produced from pure helium droplets, was found to increase with droplet size until an asymptotic limit was reached for $<N> = 50\ 000$ helium atoms. The effect of a dopant species was shown to alter the He_n^+ / He_2^+ ($n \geq 3$) signal ratio for smaller droplet sizes and was attributed to the potential energy gradient created by the cation-dopant interaction, and its potential to draw the positive charge towards the centre of the droplet. Core-shell particles, consisting of a water core and a co-dopant outer shell, were produced using a sequential pickup technique and were analysed with electron impact ionization. Of the co-dopants used O_2, N_2, C_6D_6 and CO_2 were found to provide a softening effect on the ionization of the water clusters, whilst CO and NO increased the fragmentation of some water cluster sizes. Results from *ab initio* calculations of $[X(H_2O)_2]^+$ cluster ions, where $X = CO$, N_2, Ar and CO_2, support the experimental results.

A new method for recording electronic spectra of species that reside in long-lived metastable states inside the helium droplets was demonstrated using the electronic excitation of toluene into its S_1 state as an example. In another spectroscopic study, infrared depletion spectroscopy was used to record vibrational spectra of water-methane clusters. From a comparison of predicted vibrational frequencies from *ab initio* calculations with the experimental spectra, possible structures for the $CH_4(H_2O)_n$, for $n = 1\text{-}3$, were identified.

TABLE OF CONTENTS

LIST OF TABLES

ACKNOWLEDGEMENTS

AUTHORS DECLARATION

The work in this thesis was conducted by the author in the Department of Chemistry at the University of Leicester during the period between September 2008 and September 2012 and is original unless otherwise acknowledged in the text or references.

None of the work has been submitted for another degree at this or any other university.

Signed _____   Date_____

CHAPTER 1

INTRODUCTION

In the study of transient species such as atoms, molecular radicals and ions, maintaining a suitable concentration of the species of interest is an inherent difficulty. It was not until the discovery of cryogenic matrix isolation by George C. Pimentel in 1954 that an efficient method to isolate short-lived species was devised.[1] In these early experiments isolation was achieved by co-deposition of the matrix and the active species onto a surface cooled low enough to condense the matrix immediately. Since its introduction, cryogenic matrix isolation has become a well-established method for the study of transient species.[2,3] Another method for isolating atoms and molecules to prevent rapid reaction, is with the use of atomic or molecular beams. A free jet molecular beam is a neutral beam of atoms/molecules extracted from an under expanded, supersonic, continuum jet expansion, which is achieved from a high-pressure gas source expanding into a low-pressure ambient gas.[4] The free jet expansion of a seeded supersonic beam not only cools molecules, but also provides a suitable flow field for investigating clustering and condensation kinetics of seeded molecules.[4]

Whilst the isolation of transient species at low temperatures (1~80 K) is readily achieved by using liquid matrices such as noble gases (xenon, krypton, and argon)[5,6] and carbon dioxide, methods for isolating single atoms and molecules in liquid helium-4 are hindered due to its low solubility for impurities. The ability to study single atoms and molecules in a liquid helium matrix is of particular interest to experimentalists because of its unique ability to remain in a liquid phase even at temperatures close to absolute zero. This unusual feature arises from a combination of the light nuclear mass and the relatively weak van der Waals interactions between the helium particles.

Another remarkable property of liquid helium is that at temperatures below 2.19 K it undergoes a unique phase transition to a superfluid state (a liquid phase with no measurable viscosity). The ability to study the behaviour of microscopic species in a superfluid environment presents many exciting possibilities. It is known from experiments probing the macroscopic behaviour of superfluid helium-4 that many unusual phenomena are observed, such as a vanishingly small viscosity and no change in the moment of inertia of a rotating disk as the temperature of helium is lowered. An added advantage is that helium is completely transparent in the entire spectral range from the far IR to the vacuum UV.

The question of how molecule sized species would behave in a superfluid environment was not answered until the mid 1990's when Jan Peter Toennies reported that ultra cold helium droplets (T= 0.37 K),[7] formed in the free-jet expansion of pre-cooled helium gas, could readily pick up foreign molecules introduced into the path of the droplet beam. By recording the infrared spectrum of OCS molecules picked up by both superfluid helium-4 droplets and non-superfluid helium-3 droplets, Toennies was able to demonstrate the microscopic manifestation of superfluidity in helium-4 droplets by the observation of narrow rotational lines, which implies that OCS molecules inside the droplets are free to rotate unhindered, whereas in helium-3 droplets the rotational lines merged into a single broad feature, as expected for a classical liquid.[8]

Recently the use of helium droplets for isolation experiments has become increasingly popular owing to their extraordinary ability to pick-up virtually any atom or molecule, either individually or in the form of clusters and suspend them in an environment in which the captured species can rotate freely. Although some experiments in helium droplets are hindered due to the inability to vary the droplet temperature, over the past few years a variety of species, including simple organic

molecules and metals, have been embedded inside helium droplets for experiments ranging from mass spectrometry and high resolution spectroscopy[9,10] to the deposition of nanoparticles.[11]

The following sections of this chapter will present an introduction to helium nanodroplets discussing the superfluid nature of bulk liquid helium below 2.17 K (1.1), the formation of superfluid helium nanodroplets (1.2), doping foreign molecules in helium droplets (1.3), electron impact ionization in helium droplets (1.4), the charge transfer process within a helium droplet (1.5), the charge transfer process within a doped helium droplet (1.6), the spectroscopy of helium droplets (1.7) and finally a description of the aims and structure of the remainder of the thesis will be given in section 1.8.

1.1. SUPERFLUIDITY

At present the two isotopes of helium, ^{4}He and ^{3}He, are the only two materials that have been successfully prepared as superfluids. These two isotopes are unique as they are able to remain in a liquid state even down to temperatures close to absolute zero, whereas all other elements and compounds will eventually freeze into solid phases well before this temperature is attained. This remarkable property arises from a combination of the light nuclear masses and the relatively weak van der Waals interactions between the helium atoms. Liquid helium-4 possesses two different liquid phases above and below a temperature of 2.17 K, which are referred to as He I and He II respectively. The transition between the two phases is often referred to as the lambda point (T_λ) due to the similarity between the Greek letter lambda λ and the characteristic singularity in the specific heat at the He I and II boundary (Figure 1.1.).[12]
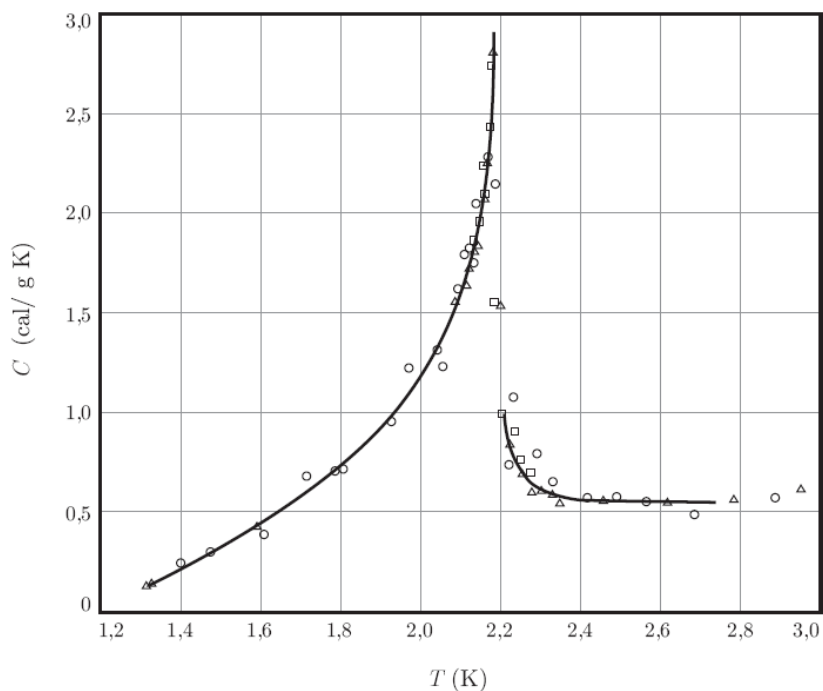
Figure 1.1. Specific heat of liquid helium under its own vapour pressure.[12]

Above the transition temperature and below the boiling point of 4.22 K ^{4}He exists in a normal colourless liquid state, the helium I phase, (He^I) and exhibits properties common to other cryogenic liquids. For example, it boils when heated, has a measureable viscosity and contracts with decreasing temperature. The situation changes dramatically when ^{4}He is cooled below 2.2 K, where instead of solidifying it undergoes a unique phase transition to a superfluid state (a liquid state with no measureable viscosity). This phase of helium, He II, was firmly demonstrated for the first time by Pyotr Kapitza, John F. Allen and Don Misener in 1938, where it was shown that there was no measurable resistance to the flow of He^{II} through small diameter (10^{-4} cm) capillaries.[13]

Superfluid ^{4}He exhibits a range of remarkable properties, such as a very high heat conductivity, a vanishingly small viscosity and many other unusual effects such as the He fountain and the film flow and creep phenomenon.[14] To account for the last of these,

even though liquid He^{II} has no measurable viscosity it still possesses surface tension that allows for the liquid to creep up and along a container without any frictional resistance to flow. The very high thermal conductivity of He^{II} means that it boils without bubbling. It is a quantum mechanical phenomenon in which heat dissipation occurs by a wave-like motion rather than a conventional diffusion process. This process is often referred to as second sound, due to the similarities between the wavelike motion of heat and sound waves in air. Another important experiment, reported by Andronikashvili in 1946,[15] involved the use of a compact disk torsional oscillator immersed in He^{II}. It was observed that the moment of inertia of the disks did not increase on reduction of the temperature, contrary to expectations for a viscous classical liquid, but instead decreased quickly below T_λ. This result demonstrated that the superfluid fraction had no effect on the moment of inertia and thus provided supportive evidence for superfluid behaviour.

Although ^{3}He and ^{4}He atoms have identical electronic properties, they exhibit completely different properties at low temperatures. This is not a result of the difference in their nuclear mass, but occurs because ^{4}He is a spin zero boson, while ^{3}He is a spin 1/2 fermion (due to an odd number of spin 1/2 constituents in the nucleus).[16] Whilst they both possess superfluid phases ^{3}He undergoes a phase transition to a superfluid state at 2.7 mK, three orders of magnitude lower than ^{4}He. Another difference between the two isotopes is that ^{3}He possesses more than one distinct superfluid phase, two of which were observed by Osheroff *et al*. in 1972.[17]

1.2.   FORMATION AND CHARACTERISATION OF LIQUID HELIUM DROPLETS

The formation of liquid helium droplets was first observed as a mist, due to the rapid Joule Thompson cooling of helium gas, in an early attempt at the liquefaction of helium by Kamerlingh Onnes in 1908.[18] At present the most common method to produce liquid helium droplets is with a free jet expansion of cryogenically cooled helium (^{4}He) gas, which was introduced by Becker *et al.*[19] in 1961, and has since become a well-established and widely used technique for the analysis of foreign species in liquid helium. Helium droplets can be readily produced with the use of either a continuous or pulsed source. In both cases helium gas is expanded through a small nozzle (nozzle diameter of 5 µm–20 µm for a continuous source and ~ 0.5 mm for a pulsed source) at low stagnation temperatures ($T_0 \leq 25$ K) and high pressures ($P_0 \geq 20$ bar).[20,21] The expanded helium gas is then cooled by the adiabatic change in state to ambient temperatures and pressures below the critical point of helium ($T_c = 5.2$ K, $P_c = 2.27$ bar), where condensation to form small droplets occurs.[9] At distances more than a few mm from the source, three-body collisions between helium atoms in the expansion begin to cease, resulting in a beam consisting of helium atoms and liquid droplets. The latter are rapidly cooled by evaporative cooling until a steady-state temperature of 0.37 K is reached.[9] Helium droplets have also been formed by expanding gaseous ^{3}He through a cryogenically cooled nozzle, and were reported to have a lower steady-state temperature of 0.15 K.[10] Since the temperature of the droplets is not low enough to provide a superfluid environment, experiments using ^{3}He droplets are not as useful for studying the rotation of molecules when compared to ^{4}He. Consequently, the remainder of this chapter will focus on ^{4}He droplets. A schematic diagram for the production and detection of helium droplets with mass spectrometry is shown in Figure 1.2.

$P_0 \geq 20$ bar

$T_0 \leq 25$ K

Pulsed droplet source   Skimmer   Pickup cell   Ionization in mass spectrometer
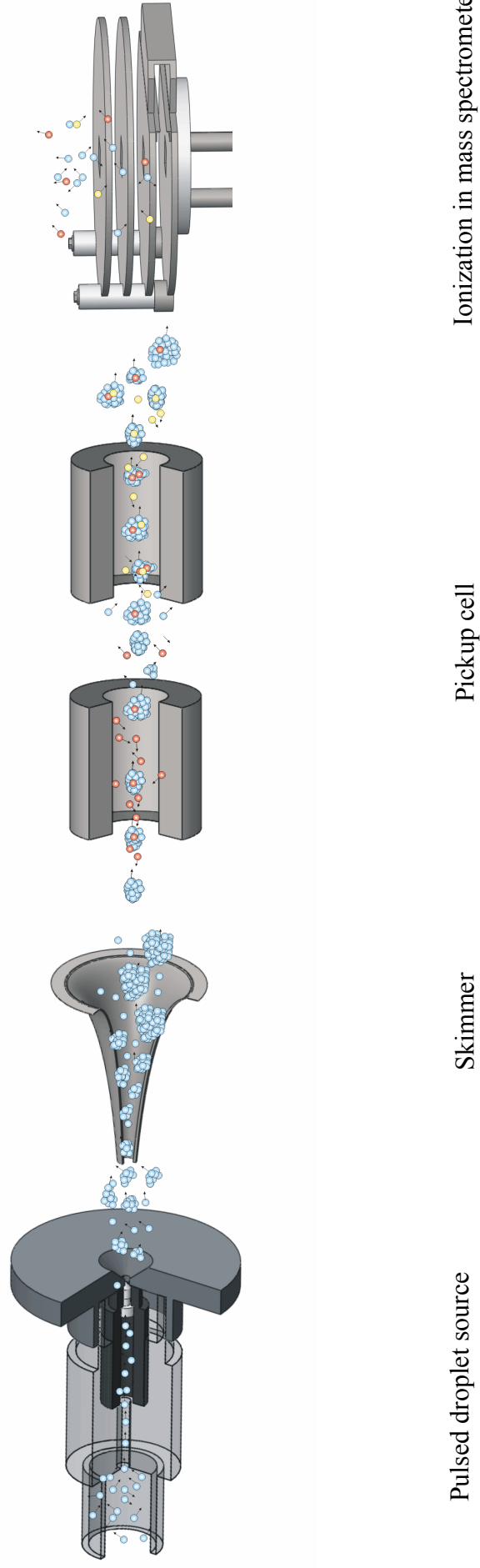
Figure 1.2. Schematic diagram of the molecular beam apparatus for the formation of doped helium droplets. Droplets are produced by the free jet expansion of helium gas from a pulsed droplet source. They then pick up foreign molecules through collisions in the pick up cells and can be detected by a mass spectrometer with an electron-impact ionizer.

The expansion of helium into a vacuum can be classified into three quantitatively different expansion regimes (assuming isentropic conditions).

1. *Subcritical* – The initial state of the expansion proceeds through a region on the high temperature side of the critical point and is well within the gaseous region of the phase diagram. Subsequent cooling by the adiabatic change in state along isentropes in the phase diagram results in temperatures and pressures well below the critical point, leading to an extensive condensation to droplets.[9] Further evaporative cooling of the droplets results in the final expansion consisting of a few helium atoms and small droplets with a mean size of $<N> \leq 10^4$ atoms.[9]

2. *Critical* – The expansion proceeds directly through or near the critical point in which neither significant evaporation (clusters formed by condensation of the gas phase) nor significant fragmentation (droplets formed by fragmentation of the liquid phase) is expected to occur.

3. *Supercritical* – The initial state of the expansion is well within the liquid region of the phase diagram. In this regime liquid helium passes through the nozzle, which subsequently breaks up into large droplets. These droplets are then further cooled by the same evaporative process as the smaller droplets. Under supercritical conditions a bimodal droplet size distribution is observed consisting of both large ($<N> > 10^6$) and small droplets ($<N> \leq 10^5$) with the former being the more predominant fraction.

The velocities of helium droplets formed under subcritical conditions with a continuous source have been measured by recording time-dependent mass spectra of He_2^+ after heating the cryogenic nozzle with a short laser pulse (10 ns). The measured velocities of the droplets were found to range from 294 – 457 m/s for clusters formed with stagnation conditions 20 bar and from 11 – 18 K.[22] For droplets formed under supercritical conditions velocities ranging from 100 – 50 m/s are observed.

1.3. CAPTURING FOREIGN MOLECULES INSIDE HELIUM DROPLETS

Foreign molecules can be confined as either single molecules or clusters, inside or on the surface of liquid droplets. Droplet doping is typically achieved by passing the droplet beam through a scattering or pickup region containing the vapour of the species of interest. In order to introduce materials that have a low vapour pressure, such as metals and large organic materials, a heated cell is required to vaporise the material. Recently metals have been vaporised with the use of a heated tungsten filament coated with a layer of the metal under study. This technique allows for a large range of metals with sufficient vapour pressure at temperatures of up to 2300 K to be studied.[11] The pickup probability of a foreign species, with the probability that k atoms/molecules will be picked up, can be estimated according to the following Poisson distribution:[23]

$$P_k = \frac{(\rho \sigma l)^k}{k!} \exp(-\rho \sigma l) \qquad (1.1)$$

where ρ is the density of the foreign species in the pickup cell, σ is the cross sectional area of the droplets (which is calculated as $15.5 <N>^{2/3}$ Å^2 for ^{4}He assuming a uniform density close to bulk liquid helium),[10] and l is the length of the pickup region.[22]

The capture of foreign species generally results in the evaporative loss of helium atoms from the surface of the helium droplet (a result of the initial kinetic and internal energy of the colliding species being transferred to the surrounding helium cage), which decreases the size of the initial droplet. In a free jet expansion of a molecular beam such as argon, nucleation of the foreign species occurs early in the expansion, with the excess energy being carried away by two-body collisions. It is this cooling that facilitates the formation of clusters into their lowest energy configuration. The situation is considerably different for a molecule picked up by a helium droplet. Instead of cooling via two body collisions, the captured foreign molecule is rapidly cooled by evaporative loss of helium atoms from the surface of the droplet (1 eV of heat released into the droplet corresponds to the evaporation of around 1600 ^{4}He atoms), which ultimately leads to the foreign species reaching the temperature (0.37 K)[7] of the surrounding helium cage.

The superfluid environment provided by a helium droplet enables a captured species to move freely and rotate unhindered within its interior. It is this property that allows molecules to coagulate and form clusters resulting from the van der Waals forces between them. The average time between the capture of foreign species is on the order of tens of microseconds, so it can be reasonably assumed that the foreign species is completely cooled between capture events.[24] Consequently, a trimer of a certain species will form when a cold monomer combines with a cold dimer and so on for larger clusters. The processes following multiple pickup events are illustrated in Figure 1.3. Work carried out by Nauta *et al.*[24,25] on H_2O and HCN has shown that this unique process gives rise to the formation of remarkable structures, such as a cyclic structure of the water hexamer (the structural motif of ice I_h) and a polymer chain of HCN molecules not seen in standard gas phase molecular beams.
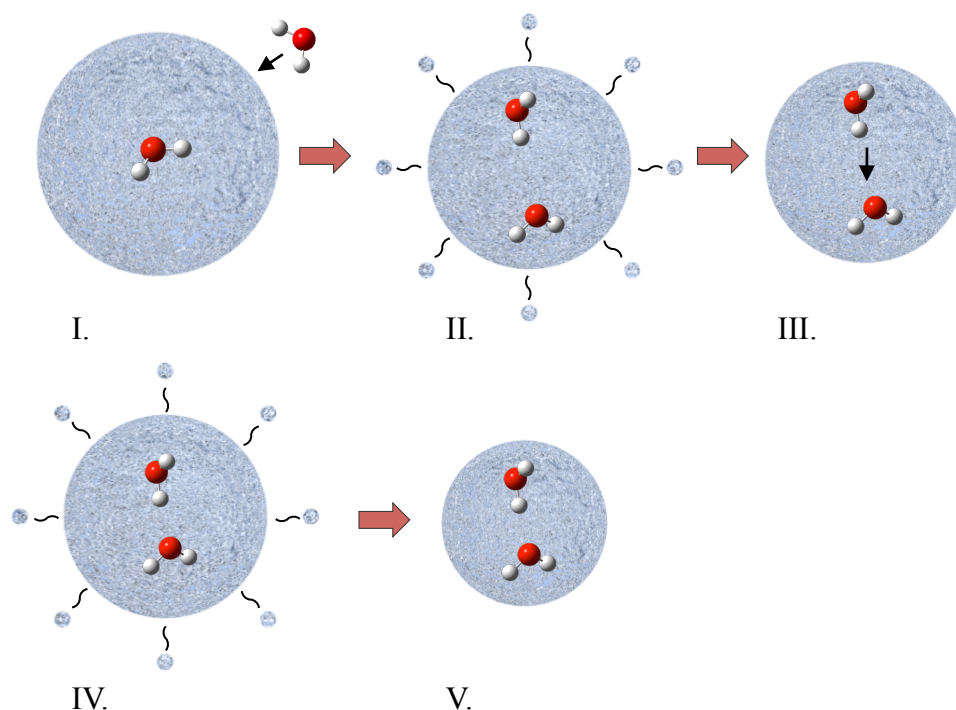
Figure 1.3. Formation of molecular clusters inside a helium droplet following the pick up of an individual molecule. I. A second species approaches a singly doped droplet. II. The initial kinetic and internal energy of the incoming molecule is removed through evaporative loss of helium atoms. III. The two foreign species are drawn together and oriented by the van der Waals forces between them. IV. Once bound the binding energy is removed by further evaporative loss of helium atoms. V. The two captured species reside as an ultra cold (0.37 K) complex.

1.3.1. Dopant location: surface or interior

The capture of foreign molecules by helium droplets results in two possible outcomes. The first is that the foreign species becomes solvated within the interior of the droplet and the second is that it resides on the surface. Whether the former or latter of these outcomes will occur is dependent on the value of the chemical potential (μ) (the binding energy of the solvated species to the entire droplet).[10] A negative value of μ indicates that the captured species will become completely immersed inside the helium droplet and such species are called "heliophilic". Results from both theoretical

and experimental studies have shown that most closed shell atoms and molecules are heliophilic.[10] Atoms and molecules having positive values of μ are called "Heliophobic" and are expected to reside on the surface of the droplet. Alkali metal atoms are examples of helophobic particles and have been found to form dimples on the surface of helium droplets.[26]

The Ancilotto parameter is a dimensionless parameter, which can be used to estimate whether a species will become solvated or reside on the droplets surface.[27] It links the gain in energy from the interaction of the solvated species with the surrounding helium cage and the energy required to create a cavity in the helium droplet (Equation 1.2).[27]

$$\lambda = \frac{\rho \varepsilon R_m}{2^{\frac{1}{6}} \gamma} \qquad (1.2)$$

Where γ, ρ, ε, and R_m is the surface tension of the liquid, the number density, the well depth and the equilibrium bond length of the corresponding solvent solute particle potential respectively. Atoms and molecules with λ values less than 1.9 will reside on the surface and those with values greater than 1.9 will reside in the interior of the droplet.[10]

1.4.   ELECTRON IMPACT IONIZATION OF HELIUM NANODROPLETS

Mass spectrometry is widely regarded as a valuable tool for providing an insight into the composition of species in the gaseous, liquid and solid phases. The main reason behind the wide applicability of mass spectrometry to compounds and mixtures of various sizes is due to the many different ionization methods available, such as electrospray ionization, Matrix Assisted Laser Desorption Ionization (MALDI),

chemical ionization, photoionization and the commonly used electron impact ionization (EI). In a typical electron impact ionization experiment there are two possible outcomes following a collision of a molecule (M) with an electron (*e*). The most probable outcome is that the collision results in electron ejection, yielding an odd-electron positively charged cation radical $[M]^{+\bullet}$ of equal mass to the original molecule.

$$M + e \rightarrow [M]^{+\bullet} + 2e \qquad (1.3)$$

The alternative and less likely outcome is that an electron may be captured by the molecule to give a negative anion radical, $[M]^{-\bullet}$.

$$M + e \rightarrow [M]^{-\bullet} \qquad (1.4)$$

The cation radical formed in the first pathway is known as the molecular ion (generally EI ionization mass spectrometers are set up to only observe positive ions). In the usual mode of operation 70 eV electrons are used to fragment the molecule under study, which produces a large amount of excess energy, which can result in further fragmentation of the molecular ion. The fragmentation pattern obtained is referred to as a molecular fingerprint and is extremely valuable for determining the initial form of the species of interest. Although the assignment of fragment peaks may be useful for simple molecules, it is often problematic for the analysis of larger molecules and mixtures.

The two types of fragmentation pathways commonly observed are:

$$[M]^{+\bullet} \rightarrow A^+ \text{ (even electron cation)} + B^\bullet \text{ (radical)} \qquad (1.5)$$

and

$$[M]^{+\bullet} \rightarrow C^{+\bullet} \text{ (cation radical)} + D \text{ (neutral molecule)} \qquad (1.6)$$
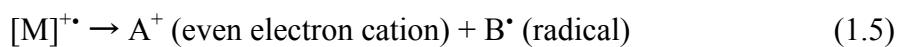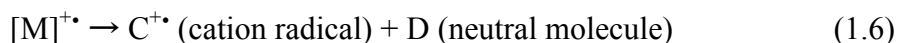
Fragmentation of the parent ion can be reduced by simply cooling the neutral molecule prior to the ionization event. One such way to achieve this is with a free jet expansion of a rare gas such as argon.[4] The limitation of this approach is that it only reduces the thermal component of the excess energy and is insufficient to cool the internal energy resulting from the ionization process. The use of liquid helium droplets as a matrix for cooling foreign species before and after the ionization event has been shown to be a much more efficient method.[28] After introducing the foreign species into the droplet cooling of the neutral molecule occurs by the transfer of its thermal and internal energy into the surrounding liquid, which results in the evaporative loss of helium atoms. If the size of the helium droplet is sufficiently large after the ionization event it is likely that the internal energy of the captured species is cooled by further evaporation of helium atoms, reducing the fragmentation of the parent ion.

1.5.   CHARGE TRANSFER WITHIN HELIUM DROPLETS

The method for the charge transfer mechanism that occurs inside helium droplets is not completely understood and relies on the assumption that only a single helium atom is ionized inside the droplet.[29] The most probable mechanism occurs by the following process. Upon electron impact of a helium droplet (with an electron of energy greater than 24.6 eV) it is expected that the initial ionization event results in the

formation of a helium ion (He^+) inside the droplet. The charge is then delocalised by a resonant charge transfer process, which is terminated when the charged ion combines with another He atom to form He_2^+ releasing 2.35 eV into the cluster.[29] The energy released from the formation of the helium dimer cation serves to induce further fragmentation of the droplet (2.35 eV corresponds to the loss of 3760 helium atoms) and if more helium atoms stick to the ionic core additional energy becomes available to further fragment the droplet.[29]

The initial positively charged He^+ ion, is thought to be produced by a sudden transition, which occurs randomly inside the droplet. In a previous study on the charge transfer process occurring inside helium droplets, it was suggested that the newly formed He^+ is, on average, a distance of 3.6 Å from the surrounding helium atoms and interacts with nearby atoms via very weak electrostatic interactions.[29] After the formation of a He^+ two competing processes begin to occur. The charge tunnels to other atoms via resonant charge transfer and the nearest neighbouring neutral atoms begin to move towards the charged He^+ ion. The mean time between steps occurs on the femtosecond timescale and since the actual motion of the atomic nuclei is small on this timescale it is assumed that the charge will hop several times before the formation and subsequent ejection of He_2^+ from the droplet.[30]

1.6.   CHARGE TRANSFER WITHIN DOPED HELIUM DROPLETS

The charge transfer mechanism for a dopant species inside a helium droplet has also been studied by Janda *et al.*[30,33] for a variety of atoms and molecules. The mechanism for a doped helium droplet is essentially the same for un-doped helium droplets in that the initial ionization event will result in the ionization of a He atom to create a He^+. The charge will then migrate towards the centre of the droplet via resonant

charge transfer to neighbouring helium atoms. Due to the stronger electrostatic forces between the helium ion and the dopant species the helium ion will more likely be drawn towards the dopant species by a potential energy gradient. The migration process will cease when the charge becomes localised as a He_2^+ or is transferred to the dopant species. The crucial factors that affect the charge transfer mechanism are the helium droplet size (the greater the droplet size the less probable it is for the charge to be transferred from a He^+ to the dopant species)[33] and the properties of the dopant species.

As an example, the ionization, charge transfer and subsequent fragmentation of argon doped helium droplets can be thought to occur by a four step process as outlined by Janda *et al.*[30] and summarised below.

Ionization,

$$He_nAr_k + e^- \rightarrow He^+He_{n-1}Ar_k + 2e^-$$

Formation of He_n^+,

$$He^+He_{n-1}Ar_k \rightarrow He_2^+He_{n-2}Ar_k \rightarrow He_m^+ + He_{(n-m)} + kAr + \Delta E$$
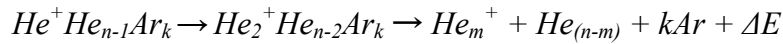
Charge transfer to a single Ar atom initially present,

$$He^+He_{n-1}Ar \rightarrow He_{n-1}He^+Ar \rightarrow He_{(n-m)} + He_mAr^+ + \Delta E$$
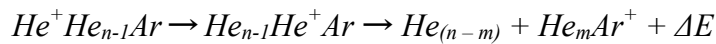
Charge transfer to more than one Ar atom initially present,

$$He^+He_{n-1}Ar_k \rightarrow He_{n-1}He^+Ar_k \rightarrow He_n + Ar_l + Ar_{(k-1)}^+ + \Delta E$$
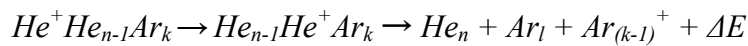
The energy released from the charge finding a dopant species is far greater than for a helium atom, which results in more fragmentation of the droplet.

If the helium droplets are exposed to electron energies lower than the ionization energy of helium (24.6 eV), then the helium atoms will become electronically excited and ionization of a dopant species will most likely occur by Penning ionization via meta-stable He^+ (2^3S), with an excitation energy of 19.8 eV.[32]

1.7. SPECTROSCOPY OF MOLECULES AND MOLECULAR CLUSTERS IN HELIUM DROPLETS

Optical spectroscopy of species embedded in helium droplets is commonly achieved by using a depletion technique, which was initially reported by Scholes *et al.* in 1992.[34] In this novel experiment the infrared spectrum of SF_6 was recorded by measuring the decrease in droplet beam intensity, with a sensitive bolometer, as a line-tuneable CO_2 laser was used to excite the v_3 vibrational mode. The observation of very narrow absorption line widths of < 0.25 cm^{-1} provided the first evidence for unusual behaviour of foreign species inside helium droplets. A schematic diagram of a typical depletion experiment is shown in Figure 1.4. Whilst a quadrupole mass spectrometer is depicted in the figure a sensitive bolometer can also be used.

Spectroscopic analysis of captured species has become increasingly popular with experimentalists in the field[9,10] as it provides a greater insight into the interactions between the captured species and the role of the surrounding liquid helium. Following the earliest experiment by Scholes *et al.* subsequent experiments carried out on SF_6 by Hartmann *et al.*[7] obtained a complete rotationally resolved vibrational spectrum, which revealed that the rotational temperature of the perturbed SF_6 molecule was 0.37 K ± 0.05, indicating that the captured molecule is cooled to the temperature of the droplet.
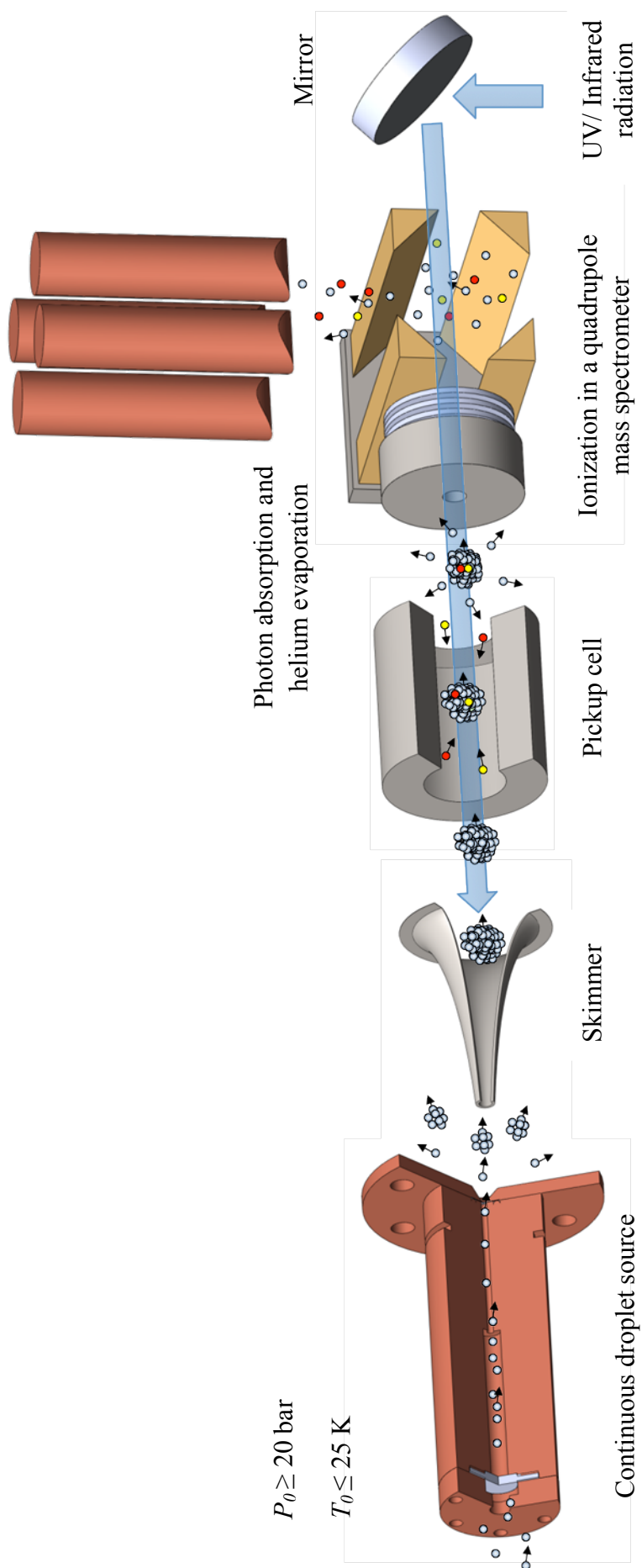
Figure 1.4. Schematic diagram of the aparatus for depletion spectroscopy of molecules and molecular clusters inside helium droplets. Following the absorption of infrared or UV radiation the droplet size will decrease through evaporative loss of helium atoms, a result of heat dissapation into the droplet following relaxation of the photon energy absorbed by the captured molecule.

In more recent work carried out by Miller *et al.* infrared depletion spectroscopy was used to identify a cyclic structure of $(H_2O)_6$[24] and a polymer chain of HCl[25] molecules, formed by the unique pick up processes that occur within the interior of an ultra cold helium droplet. Many other examples of the depletion spectra of molecules in helium droplets have been reported.[10]

Whilst depletion spectroscopy is commonly applied to experiments involving vibrational spectroscopy, other techniques such as laser induced fluorescence (LIF)[35] and resonance enhance multi-photon ionization (REMPI)[36] are sometimes more effective for studying electronic transitions. This is because beam depletion spectroscopy relies on the efficiency of the non-radiative energy transfer from the optically excited dopant into the surrounding liquid helium. In some cases the amount of energy that is transferred into the droplet can be significantly less than the photon energy absorbed; especially if the species under investigation has a large fluorescence quantum yield. In such cases, the reduction in droplet size will depend on the vibrational energy content of the molecule following fluorescence, which is often much lower than the photon energy absorbed. Therefore, if molecules fluoresce from their electronic excited states, then laser-induced fluorescence (LIF) will be more efficient for recording optical spectra.[35]

1.8.   OUTLINE OF THESIS

The remaining chapters of this thesis will discuss the following. Chapter 2 will present details about the pulsed helium droplet source that was used for electron impact ionization studies of dopant species within helium droplets. This chapter also includes information about the design and implementation of a continuous nozzle for the production of helium droplets for use in depletion-type spectroscopy experiments.

Chapter 3 presents details about the formation of helium cluster cations following electron impact ionization of helium droplets, with particular interest in the role of droplet size and dopant species on the charge transfer mechanism. Chapter 4 will discuss the formation of core-shell structures consisting of a water core and a co-dopant outer shell. The emphasis of this work was to explore whether an outer shell of a co-dopant would reduce the degree of fragmentation of water clusters following electron impact ionization. Chapter 5 presents the details of a new technique for recording optical spectra in helium droplets. The technique is applicable when optical excitation of a dopant species leads to the formation of a long-lived metastable state inside a helium droplet. If the dissipation of energy from this metastable state into the helium droplet is inefficient, then the optical spectrum can be recorded as a difference in the abundance of the ion fragments of the dopant species, as opposed to a difference in the ionization cross-section of the droplet. Finally, chapter 6 will present preliminary findings for infra-red depletion spectroscopy of water-methane binary clusters: $CH_4(H_2O)_n$ (n = 1-3). The specific aim of this work was to identify possible structures for the complexes (n = 1-3) by comparing the experimental spectra with the vibrational frequencies of $CH_4(H_2O)_n$ predicted from *ab initio* calculations.

REFERENCES FOR CHAPTER 1

1. E. Whittle, D. A. Dows, G. C. Pimentel, *J. Chem. Phys.* 1954, **22,** 1943.

2. I. R. Dunkin, *Matrix-Isolation Techniques - A Practical Approach*, Oxford, Oxford University Press, 1998.

3. M. J. Almond, A. J. Downs, *Spectroscopy of Matrix Isolated Species*, John Wiley & Sons Ltd, 1989.

4. G. Scoles, *Atomic and Molecular Beam Methods, Vol.1*, Oxford University press, New York, 1988.

5. R. Sliter, M. Gish, A. F. Vilesov, *J. Phys. Chem. A*, 2011, **115**, 9682.

6. B. Michielsen, J. J. J. Dom , B. J. van der Veken , S. Hesse , M. A. Suhm W. A. Herrebout, *Phys. Chem. Chem. Phys.*, 2012, **14**, 6469.

7. M. Hartmann, R. E. Miller, J. P. Toennies, A. Vilesov, *Phys. Rev. Lett.*, 1995, **75**, 1566.

8. S. Grebenev, J. P. Toennies, A. F. Vilesov, *Science*, 1998, **279**, 2083.

9. J. P. Toennies, A. F. Vilesov, *Annu. Rev. Phys. Chem.,* 1998, **49**, 1.

10. J. P. Toennies, A. F. Vilesov, *Angew. Chem. Inst. Ed*. 2004, **43**, 2622.

11. V.Mozhayskiy, M. N. Slipchenko, V. K. Adamchuk, A. F. Vilesov, *J. Chem. Phys*, 2007, **127**, 094701.

12. F. London, *Superfluids Volume II – Macroscopic Theory of Superfluid Helium*, Dover Publications, New York, 1964.

13. P. L. Kapitza, *Nature*, 1938, **141**, 74; J. F. Allen, A. D. Misener, *ibid.*, 75.

14. B. V. Rollin, F. Simon. *Physica VI,* 1939, **2**, 219.

15. E. L. Andronikashvili, *J. Phys USSR*, 1946, **10**, 201.

16. J. F. Annett, *Superconductivity, Superfluids and Condensates*, Oxford University Press, New York, 2004.

17. D. D. Osheroff, R. C. Richardson, D. M. Lee, *Phys. Rev. Lett.*, 1972, **28**, 885.

18. H. Kamerlingh Onnes, *Commun. Phys. Lab.Univ. Leiden.,* 1908, **105**, 744.

19. E. W. Becker, R. Klingelhoöfer, P. Lohse. *Z. Naturforsch. Teil. A*. 1961, **16,** 1259.

20. M. N. Slipchenko, S. Kuma, T. Momose, and A. F. Vilesov, *Rev. Sci. Instrum,* 2002, **73**, 3600.

21. S. Yang, S. M. Brereton, A. M. Ellis, *Rev. Sci. Instrum.*, 2005, **76**, 104102.

22. S. Grebenev, J. P. Toennies, A.F. Vilesov, *Science*, 1998, **279**, 2083.

23. M. Lewerenz, B. Schilling, J.P. Toennies, *J. Chem. Phys.*, 1995, **102**, 8191.

24. K. Nauta, R. E. Miller, *Science*, 2000, **287**, 293.

25. K. Nauta, R. E. Miller, *Science*, 1999, **283**, 1895.

26. O. Bünermann, G. Droppelmann, A. Hernando, R. Mayol, F. Stienkemeier, *J. Phys. Chem. A*, 2007, **111**, 12684.

27. F. Ancilotto, P. B. Lerner, M. W. Cole, *J. Low Temp. Phys.*, 1995, **101**, 1123

28. W. K. Lewis, B. E. Applegate, J. Sztáray, B. Sztáray, T. Baer, R. J. Bemish, R. E. Miller, *J. Am. Chem. Soc*, 2004, **126**, 11283.

29. B. E. Callicoatt, K . Förde, L.F. Jung, T. Ruchti, K. C. Janda, *J. Chem. Phys*, 1998, **109**, 10195.

30. B. E. Callicoatt, K. Förde, T. Ruchti, L. Jung, N. Halberstadt, K. C. Janda, *J. Chem. Phys.*, 1998, **108**, 9371.

31. A. Scheidemann, B. Schilling, and J. P. Toennies, *J. Phys. Chem.*, 1993, **97,** 2128.

32. H. Schöbel, P. Bartl, C. Leidlmair, M. Daxner, S. Zöttl, S. Denifl, T. D. Märk, P. Scheier, D. Spångberg, A. Mauracher, D. K. Bohme, *Phys. Rev. Lett.*, 2010, **105,** 243402.

33. B. E. Callicoatt, D. D. Mar, V. A. Apkarian, K. C. Janda, *J. Chem. Phys.*, 1996, **105**, 7872.

34. S. Goyal, D.L. Schutt, G. Scholes, *Phys. Rev. Lett.*, 1992, **69**, 933.

35. S. Kuma, H. Goto, M. N. Slipchenko, A. F. Vilesov, A. Khramov, T. Momose, *J. Chem. Phys.*, 2007, **127**, 214301.

36. E. Loginov, D. Rossi, M. Drabbels, *Phys. Rev. Lett.*, 2005, **95**, 163401.

CHAPTER 2

EXPERIMENTAL

This chapter presents details of the experimental setup. In the first section, a detailed description of a pulsed helium droplet system, used for electron impact ionization studies of molecules and clusters in helium nanodroplets, will be given. The following sections will then discuss the modifications made to produce a continuous helium droplet beam and the laser setup used for optical spectroscopy of doped helium droplets in this continuous beam.

2.1.   PULSED HELIUM DROPLET SOURCE: THE NOZZLE

For experiments involving the study of fragmentation patterns following electron impact ionization of doped helium droplets, a pulsed valve was employed. The use of a pulsed rather than a continuously flowing source of helium nanodroplets was originally chosen as the means for making helium nanodroplets in the University of Leicester Spectroscopy laboratory. The original motivation in choosing a pulsed source was to achieve a high flux while requiring a modest pumping capacity.

Formation of helium droplets with the use of a pulsed valve requires the expansion of pre-cooled helium gas, with a sufficiently high backing pressure (> 10 bar), into an evacuated chamber. As the gas expands it is collisionally cooled producing a droplet beam, whose average size depends on the stagnation pressure and temperature of the valve.

The pulsed droplet source consists of a commercial solenoid pulsed valve (General Valve, series 99) compression sealed to a modified faceplate (Figure 2.1). The valve is capable of reaching temperatures as low as 4 K when in good contact with the

closed-cycle cryostat (see later). The modifications to the faceplate include a conical shaped nozzle, consisting of converging and diverging cones on either side of the faceplate, and a short (0.6 mm wide and 0.1 mm long) constricting zone in-between the converging and diverging cones (Figure 2.2).[1]
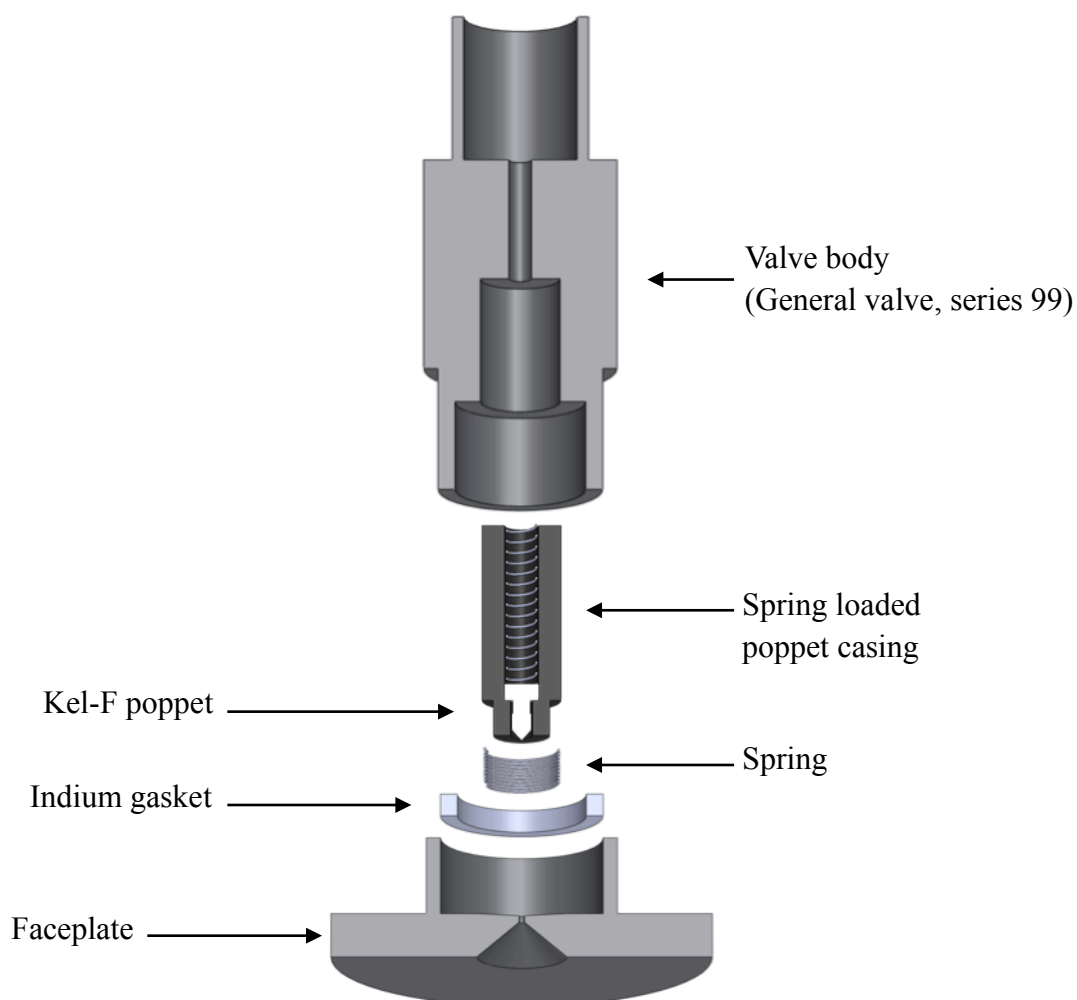
Figure 2.1. Pulsed valve assembly consisting of a commercial solenoid pulsed valve (General Valve, series 99) with a custom-made faceplate.

Whilst helium droplets were also observed with the use of a faceplate with a straight channel cut through its centre, the conical design gave an improved size control

and flux of the droplet beam.[1] This is likely a result of increased collisions between helium atoms in the constricting zone, which leads to a premature condensation to liquid droplets prior to the rapid cooling that occurs at the exit of the nozzle.
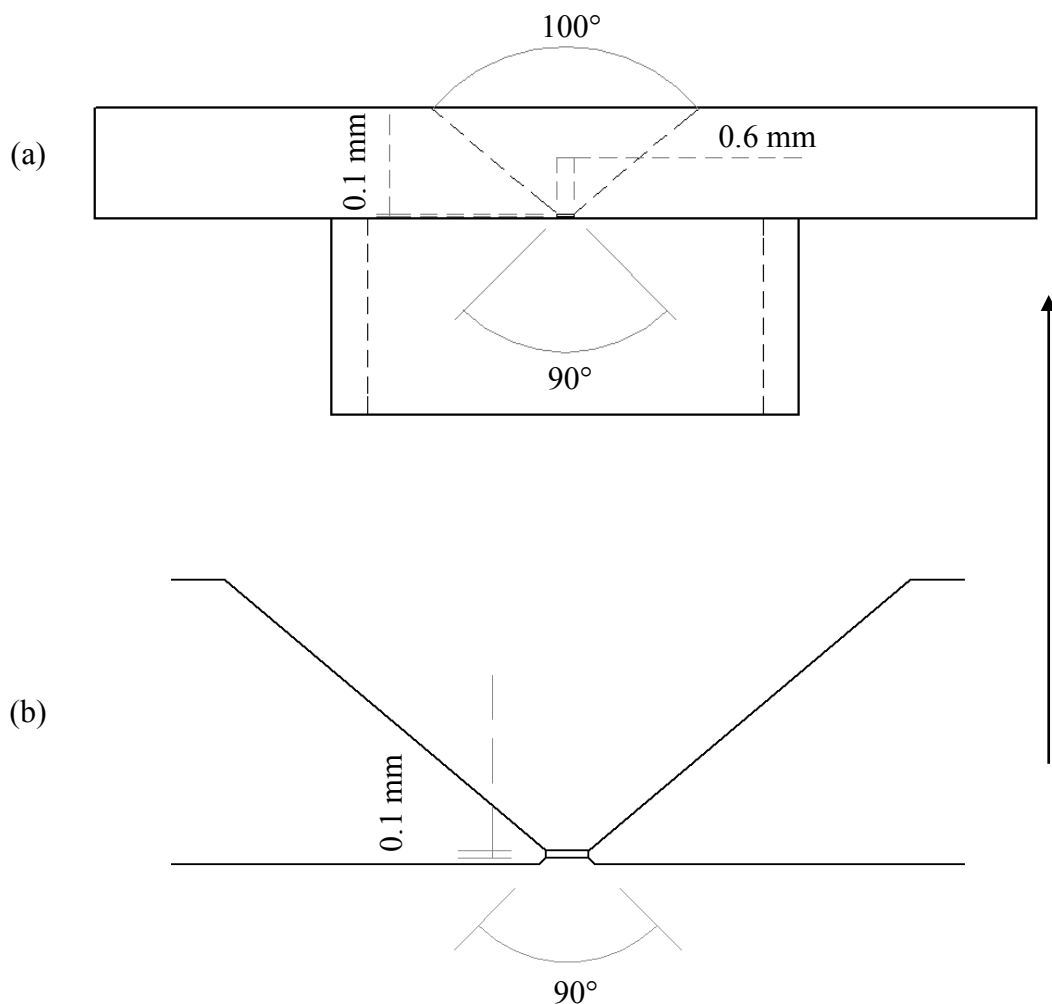
Figure 2.2. Schematic diagram of the faceplate for the pulsed helium droplet source showing (a) the profile of the faceplate and (b) an expanded view of the nozzle geometry. The arrow indicates the direction of flow.

The valve body is compression sealed to the faceplate with the use of indium wire, shaped into the form of a ring, which provides a leak tight seal at temperatures as low as 10 K with a constant backing pressure of 20 bar. An added advantage of using

indium wire is that the assembly can be resealed by simply squashing the compressed indium back up close to the edges of the interior of the faceplate. The opening and closing of the valve is achieved through movement of a poppet, which is spring-loaded and is driven into and out of a sealing position by the solenoid. As the valve body is tightened to the faceplate the poppet, which is made from Kel-F (a homopolymer of chlorotrifluroethylene), is compressed into the exit aperture on the faceplate, which prevents helium gas from leaking from the front of the nozzle. The use of Kel-F poppets is ideal as they are robust at the very low temperatures required for droplet formation, whereas other materials such as Teflon have a tendency to crack under extreme conditions.

The firing of the pulsed valve was controlled by an IOTA ONE control unit, which can be internally or externally triggered and can be used to set the valve opening time, Δt. The valve was typically operated at nominal opening times longer than Δt >120 µs at temperatures < 30 K with a repetition rate of 10 Hz. When the valve is opened using this Δt a rise in pressure of the source chamber, from ~3.0×10^{-8} mbar to ~2.0×10^{-6} mbar, is observed and if helium droplets are being successfully produced He_n^+ ions, begin to appear in the mass spectrum (see later). A maximum intensity of He_n^+ ions in the mass spectrum was observed when the valve was operated at an opening time of $\Delta t = 125$ µs.

In order to ensure that the valve operated consistently after changing the poppet and subsequent reassembly of the valve, the opening time of the valve has to be calibrated carefully at room temperature. It was found that by optimizing the opening time of the valve to be closed at an opening time of $\Delta t = 130$ µs, partially open at $\Delta t = 140$ µs and fully open at $\Delta t = 150$ µs at room temperature, gave an optimal helium

signal at an opening time of Δt = 125 μs when the valve was subsequently run at low temperatures (< 30 K).

The difference in the opening time of the valve at room temperature and at low temperatures is representative of a delay between the trigger signal and pulse firing with decreasing temperature, a result of a slower mechanical response of the valve at low temperatures. Whilst other opening times were explored, it was found that at shorter and longer opening times the total helium cluster cation signal decreased.[1] As such, for most experiments, the valve opening time that produced the strongest droplet signal in the mass spectrum was used. The decrease in signal at longer opening times could be a result of increased collisions between gaseous helium scattering off the walls of the source chamber and the helium nanodroplets, thus helping to destroy the latter.

The average size distribution of a helium droplet, containing $<N>$ helium atoms, can be controlled by altering the stagnation pressure and temperature, with the average droplet size increasing with higher pressures and lower temperatures. Droplets formed under stagnation temperatures of 24 K, 16 K and 14 K, with a backing pressure of 80 bars, have been determined experimentally, in a crossed beam scattering experiment, to be $<N>$ = 3170, $<N>$ = 7220 and $<N>$ = 14400 respectively.[2] As condensation occurs by a statistical process,[2] that follows a log normal distribution, scaling laws of the form $<N> \propto P^2 d T^{-5}$, where p, T and d are the pressure in bars, temperature in Kelvin and diameter of the nozzle in μm respectively, can be used to estimate droplet sizes.

The absolute droplet sizes, formed from a pulsed helium droplet source, have been investigated previously by Yang *et.al.* and can be calculated with the following scaling law (Equation 2.1),

$$<N> = 4.774 \times 10^9 \left(\frac{p^{0.956}}{T^{6.046}} \right) \qquad (2.1)$$

where p and T are the helium stagnation pressure in bars and temperature in Kelvin respectively.[1] This scaling law was obtained from mass spectrometric measurements of the abundances of $H_3O^+(H_2O)_m$ cluster ions in mass spectra recorded using various stagnation pressures and temperatures.[1] Residual water vapour was used in this study as it was present at a constant level and provided a simple and rapid means to explore the effect of various pressures and temperatures on the droplet size.[1] However, the partial pressure of the water vapour used in these experiments was too low to be recorded. Consequently, a second experiment where toluene was delivered with various known partial pressures was carried out in order to calibrate the water vapour data.

Although the partial pressure of the water vapour was unknown Yang *et.al.* were able to fit the abundances of $H_3O^+(H_2O)_m$ cluster ions in each mass spectrum, obtained with various source conditions, with the following Poisson distribution $p_k(z) = z^k \exp(-z)/k!$ and extract z. Since $z = \sigma n l$, where σ is the cross section of the helium droplet, n is the number density of species of interest and l is the distance the droplet beam travels in contact with the dopant species, its value can be related to the number of helium atoms in the droplet by the relationship $N \propto \sigma^{3/2}$. From the mass spectrometric measurements of the water vapour data there was sufficient data to ascertain how z varies with P and T. They found that as they lowered the nozzle temperature and kept the stagnation pressure fixed the value of z would increase, a similar trend was observed for a fixed nozzle temperature and increasing stagnation pressures, which indicates that the droplets increase in size with decreasing temperature and increasing pressure.[1]

To provide an estimate of the absolute droplet sizes, toluene was added into the pickup cell with known partial pressures and the toluene monomer ion signal was monitored as a function of pressure. The toluene data was fitted to a Poisson distribution and yielded droplet sizes of 10 880 ± 40 (P=14 bars, T=13.0 K) and 29100

± 200 (*P*=10 bars, *T*=10.5 K) helium atoms.[1] Having obtained this data Yang *et.al.* were able to calibrate the data from the water vapour experiment and determine the helium droplet sizes over the full range of source conditions used and extract the scaling law shown above (see equation 2.1). This scaling law implies that droplets with a mean size of *<N>* ~2000 helium atoms will be obtained for source conditions of 16 K and 8 bars while droplets with *<N>* ~80000 helium atoms will be obtained at 10 K and 20 bars.[1]

Helium droplets produced in pulsed mode have been shown to undergo velocity dispersion according to their size, which makes it possible to probe different droplet sizes simply by varying the time at which the probing particles (electrons or photons) cross the droplet beam.[3] Using mass spectrometry to obtain approximate droplet sizes, the droplet sizes obtained for an opening time of 125 μs, with source conditions of 10 K and 16 bars, vary from *<N>* ~4000 helium atoms near the beginning of the droplet pulse to approximately *<N>* ~90000 helium atoms towards the end. The time between the beginning and the end of the droplet pulse was found to be ~80 μs for a nominal valve opening time of 125 μs, which allows for convenient size selection with a delay generator with a microsecond time resolution. The ability to vary the time between the firing events of the pulsed valve and an electron gun also allows for a convenient method to subtract contributions of residual background gasses, such as O_2, N_2 and H_2O, from the helium droplet mass spectrum, by recording a mass spectrum prior to the optimal droplet signal and then subtracting it from the helium droplet mass spectrum.

2.2. PULSED HELIUM DROPLET SYSTEMS: APPARATUS

A schematic illustration of the overall helium droplet apparatus is shown in Figures 2.3 and 2.4. The vacuum system consists of three differentially evacuated regions.

Reflectron time of flight

Liquid nitrogen cooled cryo-trap chamber

$\{< 10^{-9} \text{ mbar}\}$

4 mm Skimmer

$\{10^{-8} \text{ mbar}\}$

1 mm Skimmer

Pickup cells

Pulsed valve

Source chamber

Closed-cycle cryostat

$\{10^{-8} \text{ mbar}\}$
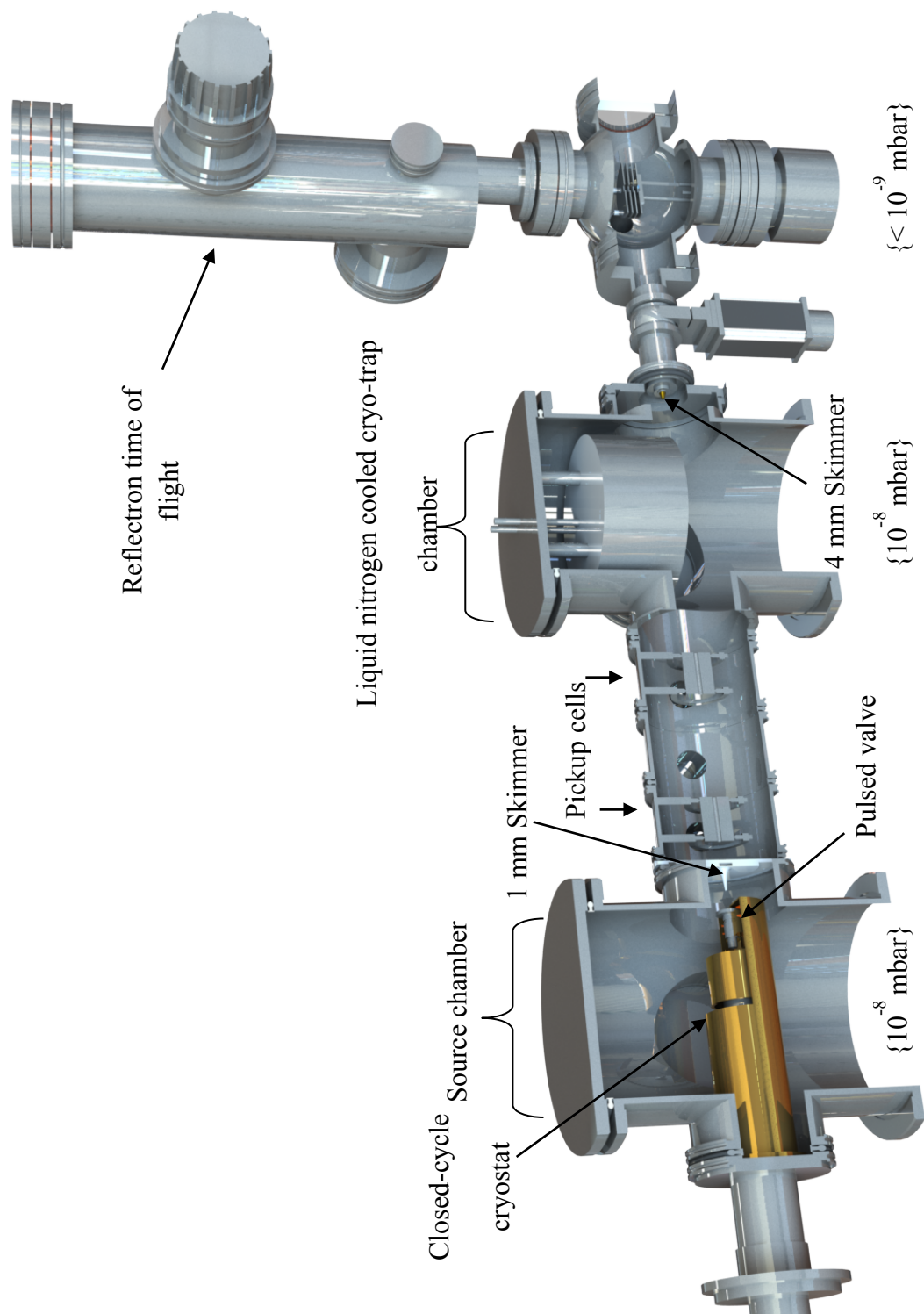
Figure 2.3. Schematic diagram of the vacuum system used for a pulsed helium droplet source.

31
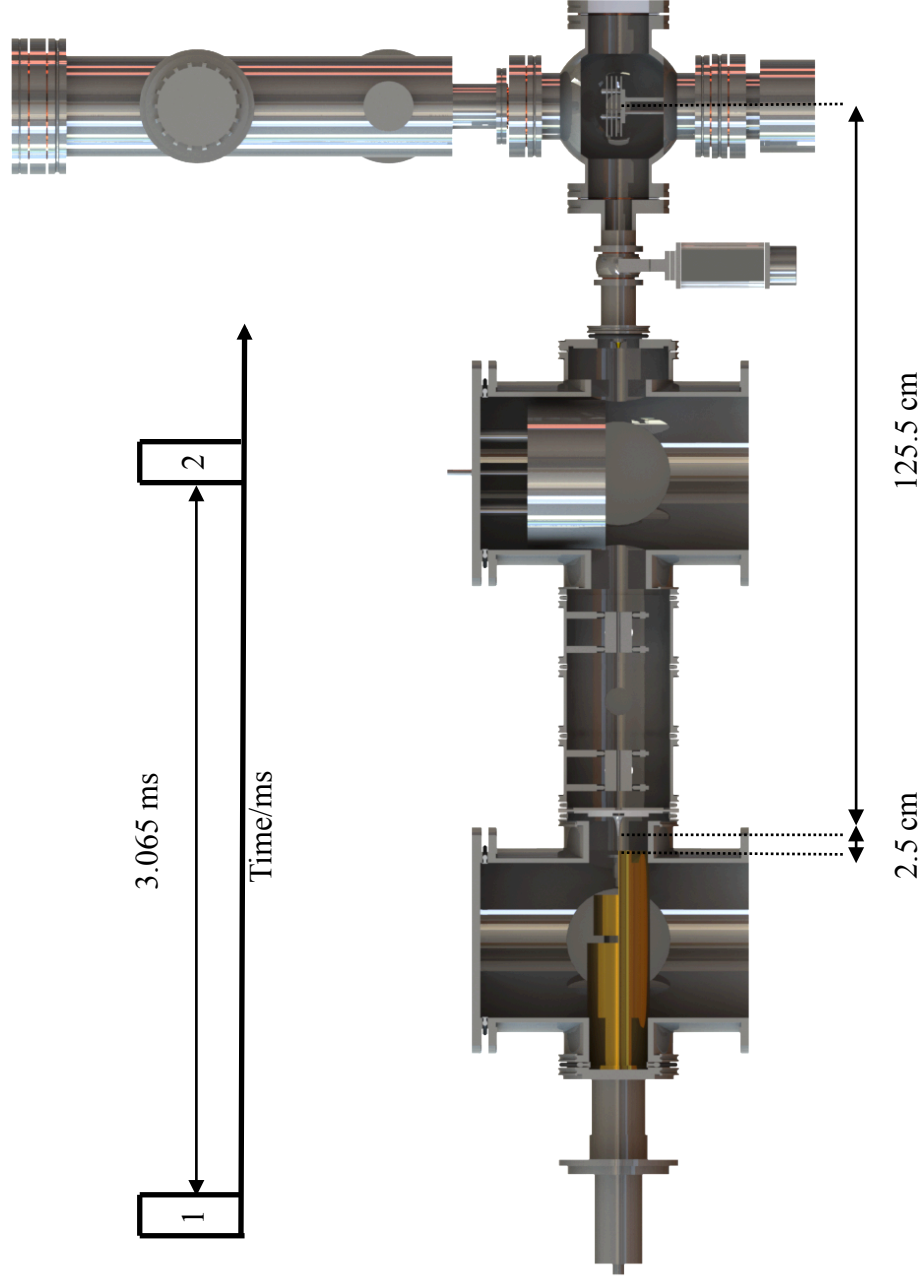
Figure 2.4. Schematic diagram showing the distance between the pulsed valve and the entrance of the skimmer and the entrance of the skimmer to the ionization region of the RE-TOF. The timing diagram (a) shows the delay time between the firing of the pulsed valve and the time at which the probing particles (electrons or photons) cross the droplet beam, for stagnation conditions of T= 20 K and P= 20 bar. The timing diagram is not to scale and 1 represents the opening of the pulsed valve and 2 represents the detection of the droplet pulse.

As mentioned previously, helium droplets were formed by expanding pressurised high purity (99.9999 %) helium gas at low temperatures ($T_0 \leq 25$ K) and high pressures ($P_0 \geq$ 8 bar) through a pulsed valve, attached to the tip of a closed cycle cryostat (Sumitomo, SRDK-408 cold head, CSW-71 helium compressor unit). The source chamber was evacuated by an oil diffusion pump (Varian, VHS-250, 4600 Ls^{-1} pumping speed for helium), which is capable of maintaining a typical pressure of 10^{-6} and 10^{-8} mbar with the pulsed valve open and closed respectively. A combination of a mechanical booster pump (EH-250-HYD) and a roughing pump (E2M-40) is used to initially evacuate the system and these form the backing pumps for the diffusion pump.

2.5 cm downstream from the exit of the nozzle the droplet beam passes through a 1 mm skimmer (Beam Dynamics) and enters the second differentially evacuated region. A distance of 2.5 cm was found to give a maximum intensity of the He$_2^+$ ion signal in the mass spectrum. This was presumably due to a reduction in the collisions between gaseous helium and the helium droplets in the region between the nozzle and the skimmer, which would otherwise act to destroy the latter. Shortly after passing through the skimmer the droplet beam passes through two separate pickup cells, placed in tandem, where the gas or vapour of a species of interest can be seeded into the droplet. The pickup cell used consisted of a 60 mm long stainless steel tube with a 40 mm diameter and a 6 mm diameter straight channel cut through its centre (Figure 2.5). Another smaller (1/8 inch) hole was drilled slightly offset from the centre at an angle to intersect the central channel. This allowed the dopant species to be administered by simply connecting an 1/8 inch copper pipe to a needle valve (EV-016-DOS-AB) by a 1/4 inch stainless steel feed through. Two pick up cells were easily mounted in our system (see Figure 2.3) and as they did not need isolated chambers only a single vacuum pump was required for the whole region. The use of these pickup cells allowed

for two dopant species to be picked up in tandem without any significant drift from either species. This allowed for experiments involving two different species to be explored in different orders, which may result in different cluster structures forming dependant on the order the two species were introduced to the droplet. Experimental examples of changing dopant order will be shown in chapter 4. The only disadvantage of this technique is that the pressures in the pick-up cells are unknown, but can be monitored by the signal of the monomer ion of the species under study observed in the mass spectrum. For gaseous species a backing pressure of 1 bar was used to ensure fine control of the dopant partial pressure.
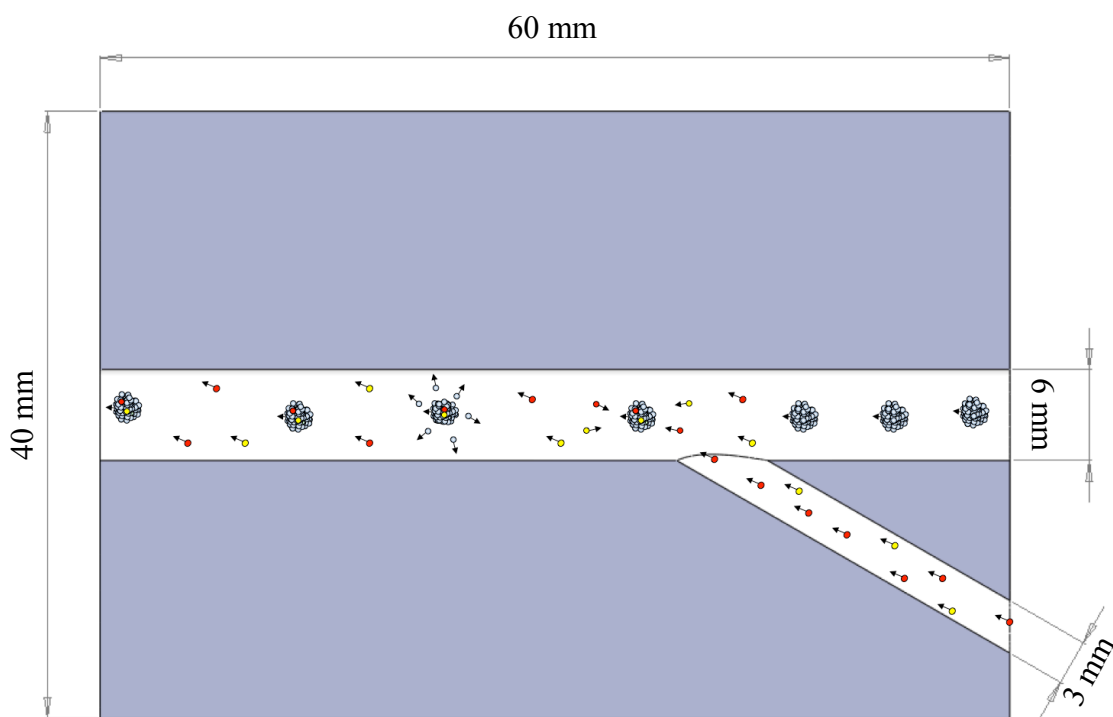
Figure 2.5. Schematic diagram of the pickup cell, arrows indicate the direction of flow.

After passing through the pickup region the droplets then travel through another vacuum chamber, this one equipped with a liquid nitrogen cooled trap, which helps to

reduce contamination of background species such as H_2O. The pickup and secondary region are evacuated by a 1000 Ls^{-1} turbomolecular pump (Varian, TV 1001 Navigator, TV 1000 HT controller), which maintains a base pressure of 10^{-8} mbar. The droplets then pass through a 4 mm skimmer and continue to the ionization region of a reflectron time-of- flight mass spectrometer (TOF-MS). This TOF-MS was purchased from Kore Technology and employs a microchannel plate detector. When venting the pulsed valve or pickup chambers for repairs/replacements the TOF-MS can be maintained under vacuum conditions by closing a pneumatic gate valve located on the entrance flange to the TOF-MS. Ionization of the helium droplets is achieved by a 70 eV pulsed electron beam, which is synchronized to fire upon the arrival of each helium droplet pulse. A timing diagram for the arrival of the droplet pulse at the ionization region of the RE-TOF is shown in Figure 2.4. From a knowledge of the distance between the pulsed valve and the ionization region (1.28 m) and the delay time between the firing of the pulsed valve and the time at which the probing particles (electrons or photons) cross the droplet beam (3.065 ms) the velocity of the droplet beam can be estimated to be 418 ms^{-1} for stagnation conditions of T= 20 K and P= 20 bar.

2.3. CONTINUOUS HELIUM DROPLET SOURCE

The pulsed source used in the early stages of the authors work was 'inherited' from work by others. However, due to fluctuations in the ion signals of peaks arising from electron impact ionization of the helium droplet (He_n^+) and the dopant species, in mass spectra recorded with a low number of averages (~400 averages), it was decided that a continuous source of helium droplets would lead to a more stable and more suitable source of droplets for depletion-type spectroscopy experiments as opposed to

the pulsed valve. Consequently, a continuous source of helium droplets was developed by the author.

Whilst many nozzle designs were tested only a brief description of the preliminary nozzles developed by the author will be given here, with more detail given on the final design of the nozzle. The formation of a continuous source of helium droplets requires the expansion of high purity (99.9999 %) helium gas, at low temperatures ($T_0 \leq 25$ K) and high pressures ($P_0 \geq 20$ bar), through a pinhole aperture into an evacuated chamber.

In the initial design of the nozzle helium gas was expanded through a copper assembly, attached to the tip of the closed cycle cryostat. An electron microscope aperture (Pt/Ir 95/5, with a thickness of 0.1 mm and a diameter of 5 mm, Gunther Frey GmbH & CO KG), with a single 5 μm hole at its centre, was placed at the tip of the copper assembly. A 5 μm aperture was chosen for compatibility with the pumping speed of the pumps. The electron microscope aperture was sealed using a cap seal, which involved placing a cap, with a 100° diverging cone, on top of a 2 mm long pillar with the aperture and an indium washer compressed in-between (Figure 2.6).

As the nozzle was cooled the gas flux of helium increased as $1/\sqrt{T_0}$, as expected for an ideal gas, which was observed as a steady increase in the source chamber pressure between 300-15 K (see Figure 2.7; Copper nozzle (cap seal)). However, with this design, the signal of the He_2^+ ion, the predominant ion from electron impact ionization of a helium droplet, was very weak compared to the He^+ ion signal at 15 K (~ 1 %), indicating that condensation to droplets, with this nozzle, was not very efficient. One of the main reasons for a weak He_2^+ ion signal comes from over compression of the cap when sealing the nozzle. This can lead to bending of the electron microscope aperture and cause a restricted gas flow due to alterations in the size of the exit aperture.
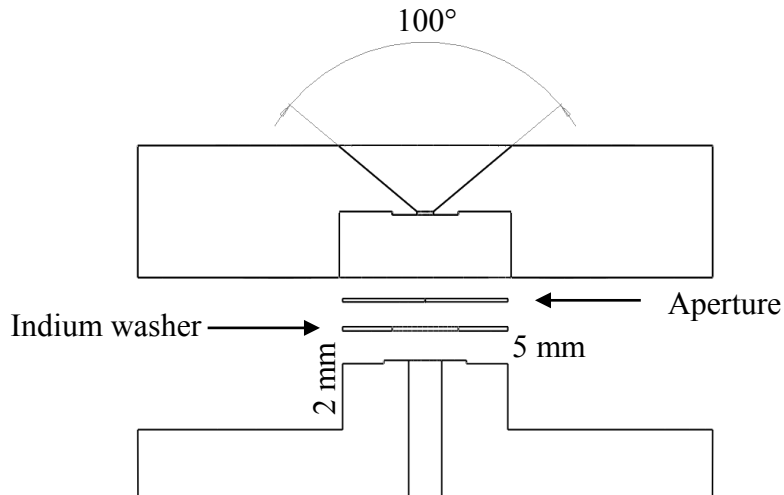
Figure 2.6. Schematic diagram of the cap seal.
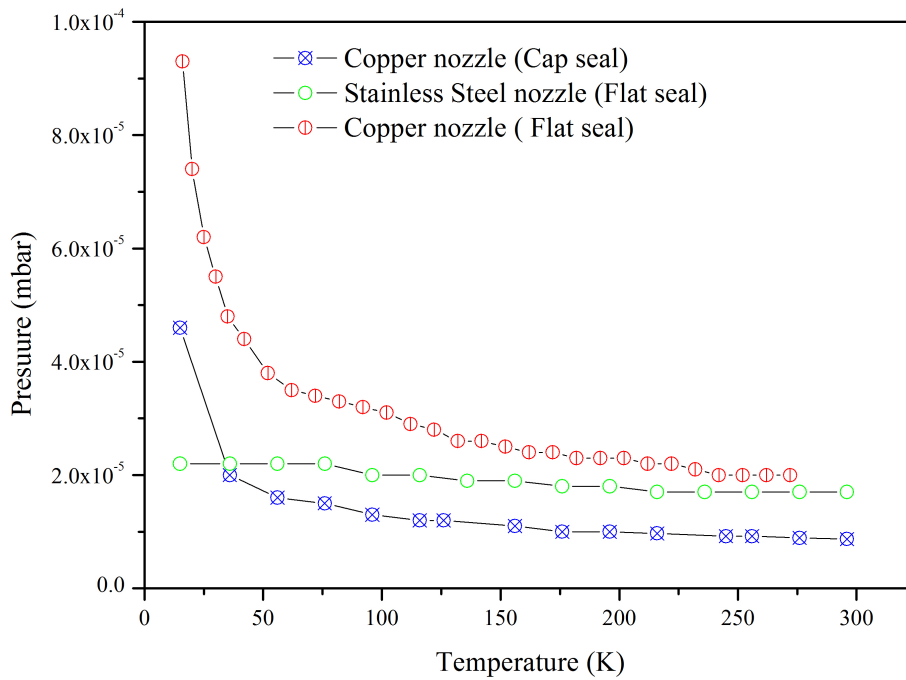
Figure 2.7. Variation in source chamber pressure with decreasing temperature.

To prevent distortions to the aperture from occurring a flat seal was designed, in which the indium could sink into a specially made groove to maintain a leak tight seal (Figure 2.8). An added advantage of the flat seal is that the aperture can be aligned to the faceplate with greater ease. In order to determine whether the flat seal would be leak

tight at low temperatures, a nozzle made from stainless steel was tested. Stainless steel was chosen as the material for the preliminary test, as it is easier to machine than copper. Although condensation to helium droplets did not occur, presumably because of the lower thermal conductivity of stainless steel when compared to copper, the flat seal was able to provide a leak tight seal at low temperatures. The flux of helium through the nozzle was also higher than that achieved using a cap seal, as indicated by the higher pressure in the source chamber (Figure 2.7), presumably a result of less strain on the aperture as it was sealed.
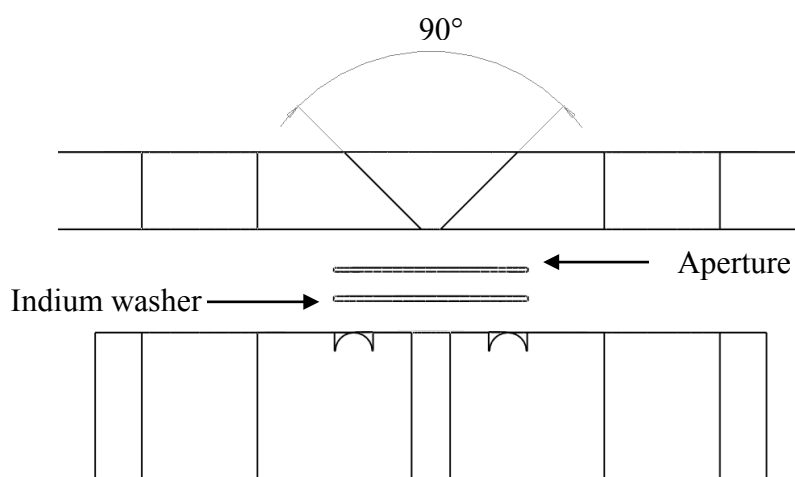
Figure 2.8. Schematic diagram of the flat seal.

In order to test the performance of the nozzle for producing helium droplets, a final version of the nozzle was made out of copper. The final version of the nozzle is shown in Figure 2.9. It consists of an electron microscope aperture with a single 5 μm hole at its centre, compression sealed between a copper cylinder (oxygen free, high conductivity), with a straight channel cut through its centre, and a copper faceplate, with a 90° diverging cone. A faceplate with a 100° diverging cone was tested before the faceplate with a 90° diverging cone. However, no significant difference between the two faceplates was observed so the 90° faceplate was left in place in order to prevent

unnecessary damage to the aperture. A leak tight seal is achieved by compressing the aperture onto an indium washer (thickness 0.125 mm, internal diameter 3 mm, outer diameter 5 mm) into the specially designed flat seal. In order to prevent impurities such as dust and H_2O from blocking the nozzle an inline sintered filter is placed just before the point where gas enters the cold head. Not only was a higher flux of gaseous helium observed (see Figure 2.7), with this nozzle, the signal of the He_2^+ ion at 15 K was also more predominant when compared to the He^+ signal (~ 15 %).

Figure 2.10 shows mass spectra of helium droplets produced with a copper continuous nozzle with a cap and a flat seal. From a comparison of the intensity of the helium cluster signals (He_n^+) it is evident that larger droplets are being formed with the flat seal.
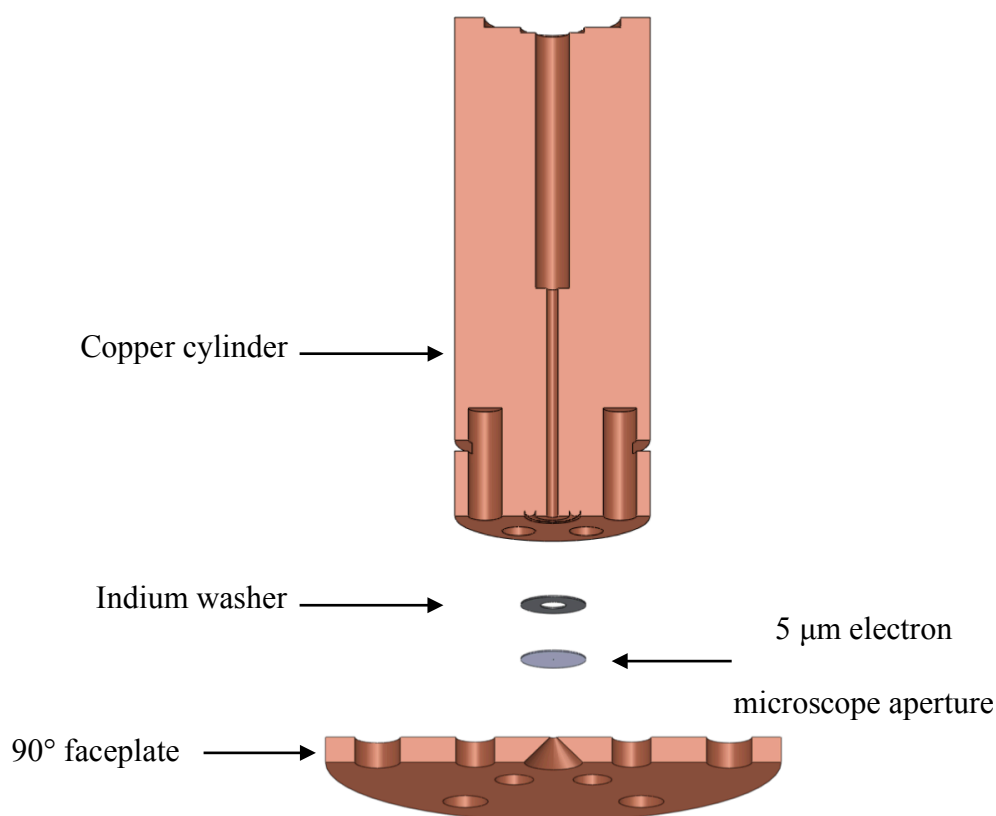
Figure 2.9. Schematic diagram of the continuous nozzle.
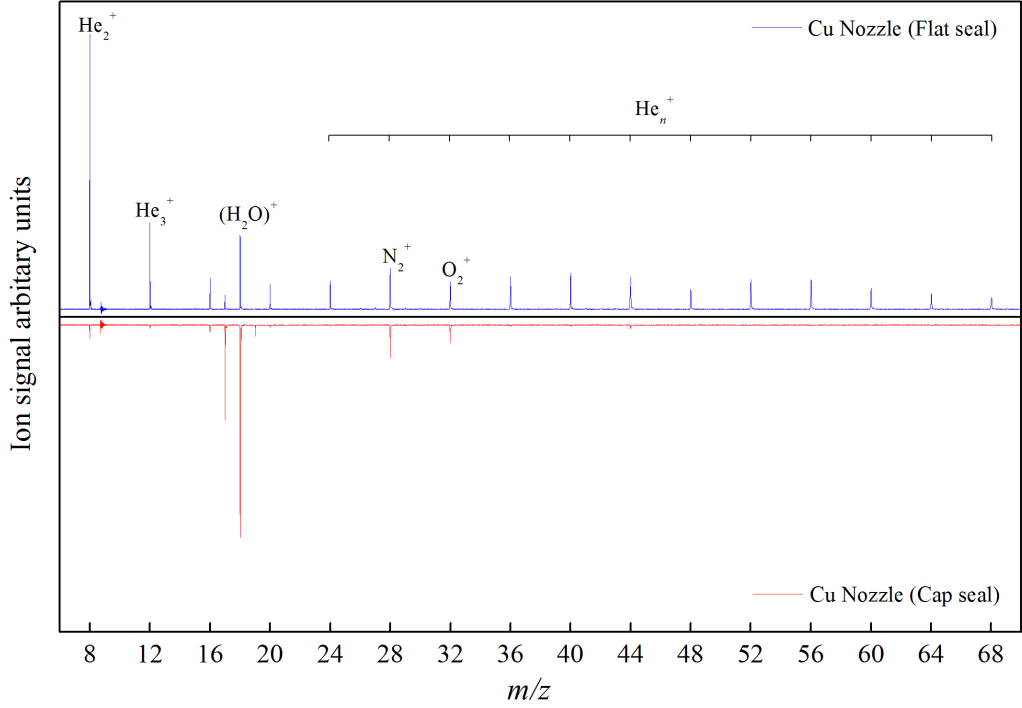
Figure 2.10. Comparison of the He_n^+ signals recorded using a copper continuous nozzle with a flat (upper panel) and cap (lower panel) seal. The helium stagnation conditions were 15 K and 20 bars.

The temperature at which condensation to droplets occurs can be approximated with knowledge of the He^+ ion signal with decreasing temperature. A comparison of the He^+ ion signal with decreasing temperature, using the cap and the flat seal, with a constant backing pressure of 20 bars of helium, is shown in Figure 2.11. The nozzle made from stainless steel, with a flat seal, is also shown for a comparison. As the temperature of the nozzle is decreased the flux increases as $1/\sqrt{T_0}$, which is observed as a steady increase in the He^+ ion signal between 270 – 70 K. Between 70 – 40 K the He^+ ion signal plateaus out and reaches a maximum around ~40 K, for both the copper cap and flat seal. Even though helium droplets are not observed in the mass spectrum at this temperature it is likely that they are beginning to be formed but are being destroyed by the high gas flux of helium, between the nozzle and skimmer, at this temperature. As the temperature of the nozzle is cooled below 40 K the He^+ signal begins to decrease

rapidly. This decrease in He^+ signal corresponds to an increase in He_n^+ ions, in the mass spectra between 15-30 K, indicating condensation to droplets.
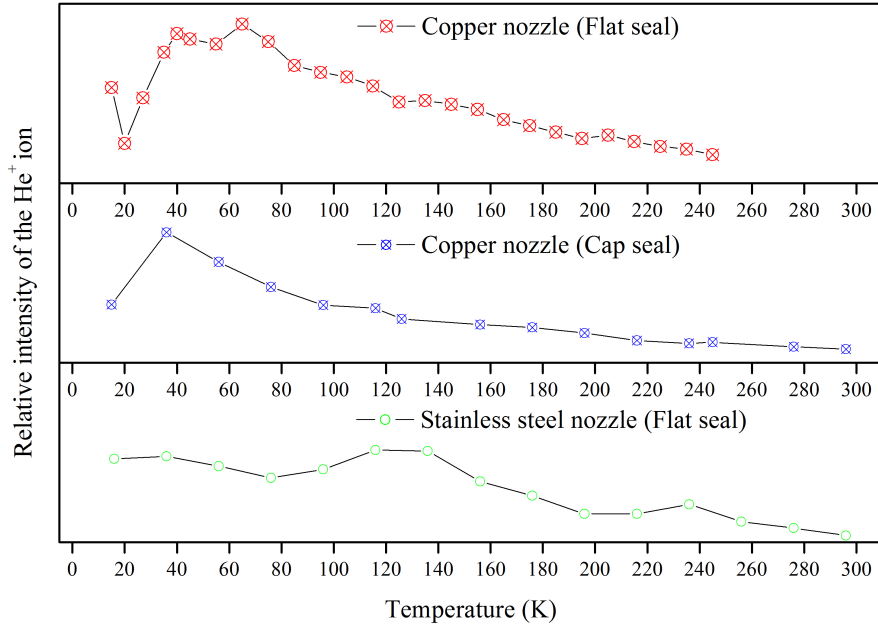
Figure 2.11. Relative intensity of He^+ in mass spectra recorded at temperatures between 300-15 K.

A scaling law that describes the average size of helium droplets formed under subcritical conditions (T > 5 K) has been reported by Moller *et al*.[4] (Equation 2.2).

$$<N> = 2.834 \times 10^5 \left(\frac{p^2 d^{1.7}}{T^{5.07}} \right) \qquad (2.2)$$

Whilst the scaling law shown above can accurately predict droplet sizes for those formed under subcritical conditions, clusters formed under supercritical conditions ($T <$ 5 K) are often larger than those predicted. This is a result of cluster formation from direct fragmentation of the liquid beam as opposed to the statistical condensation mechanism that occurs in a subcritical expansion of helium.

A schematic illustration of the overall apparatus for the continuous helium droplet system is shown in Figure 2.12. The vacuum system is similar to that described for the pulsed system, in that the cold head, chambers and pumps used to evacuate each region are the same as those described previously. Consequently only a description of the modifications made will be given.

The formation of helium droplets with the continuous system is essentially the same as that described for the pulsed system, with the substitution of the pulsed valve for the continuous nozzle described above. Unlike the pulsed system where the mechanical booster pump was used only when initially evacuating the chamber, in order to cope with the continuous flow of helium gas into the source chamber the booster pump was left on permanently to back the diffusion pump when the nozzle was cooled to low temperatures ($T < 20$ K).

An X-Y translation stage, manufactured in the University of Leicester workshop, was added to the system to allow for fine alignment of the nozzle with respect to the skimmer. To reduce the amount of gaseous helium entering the pickup and detection regions a 0.5 mm skimmer (Beam dynamics) was used in place of the 1 mm skimmer. In order to achieve a stable helium droplet beam at low temperatures, $13 - 11$ K, where the high flux of gaseous helium acts to destroy the helium droplets, through increased collisions between gaseous helium and liquid droplets in the region between the nozzle and skimmer, the skimmer was placed 2.5 cm downstream from the exit of the nozzle, which was long enough to allow gaseous helium to escape and reduce the build up of turbulence.
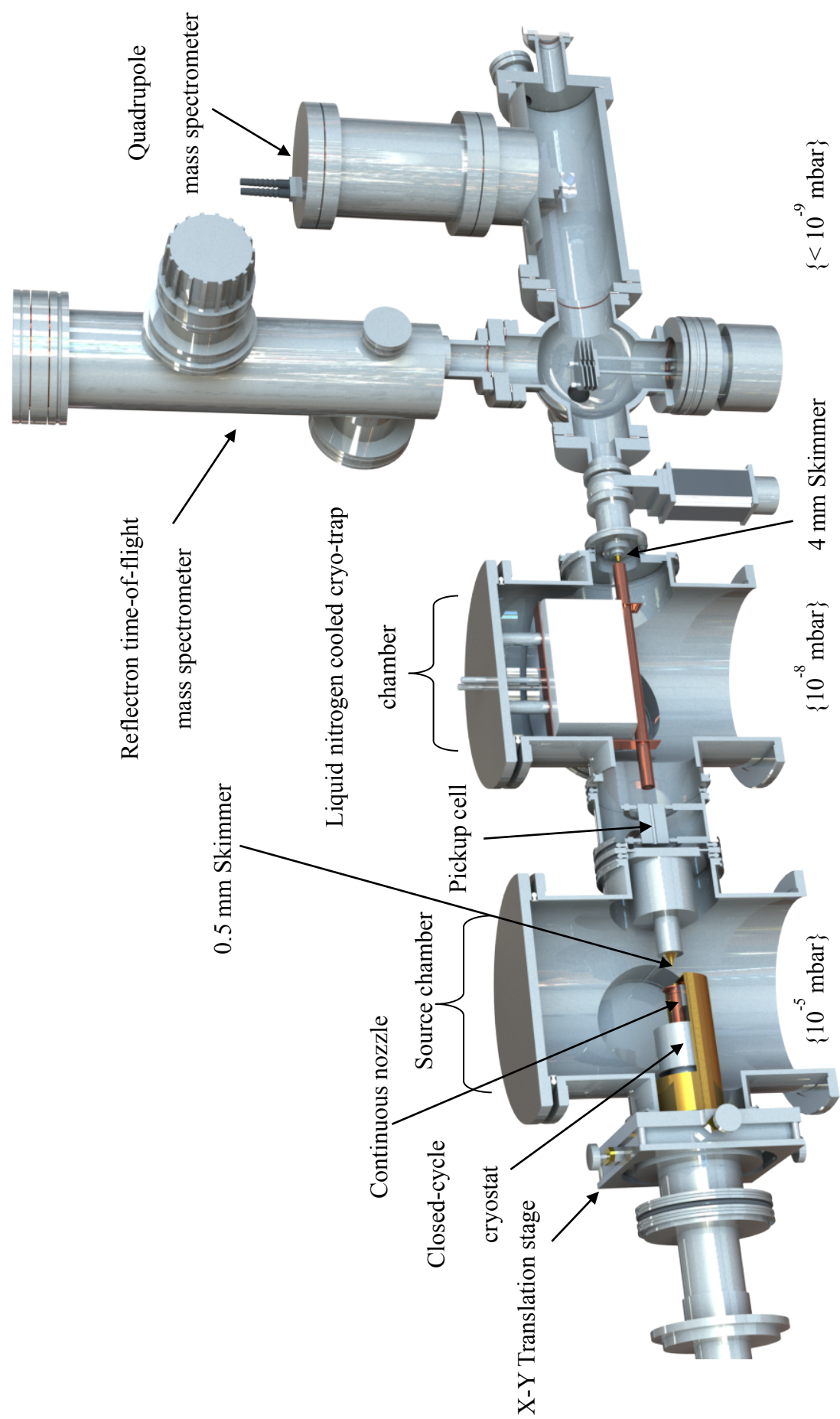
Figure 2.12. Schematic diagram of the vacuum system used for a continuous helium droplet source.

Quadrupole mass spectrometer

Reflectron time-of-flight mass spectrometer

Liquid nitrogen cooled cryo-trap chamber

0.5 mm Skimmer

4 mm Skimmer

Pickup cell

Continuous nozzle

Source chamber

Closed-cycle cryostat

X-Y Translation stage

$\{< 10^{-9} \text{ mbar}\}$

$\{10^{-8} \text{ mbar}\}$

$\{10^{-5} \text{ mbar}\}$

The pickup cell is similar to that described previously, with the only difference being the addition of a second hole, to allow for the addition of two species into a single pickup cell. A needle valve with 1/4 inch diameter Swagelok connections (FTI, Hamlet H-1300, metering valve) was used to administer the dopant species, as the use of species such as ammonia and toluene either degraded or expanded the O-rings sealing the needle valve listed previously. To reduce contamination from background H_2O, in the region between the pick up cell and the entrance of the 4 mm skimmer, a copper pipe was attached to the liquid nitrogen cooled trap. To prevent a build up of gaseous helium inside the pipe various holes were made to allow for gaseous helium to escape.

The detection region consists of both a reflectron time-of-flight mass spectrometer (the Kore Technology system mentioned earlier) and a quadrupole mass spectrometer (Extrell ELQ-400 series) placed in tandem. The quadrupole mass spectrometer was included to provide a constant signal of a particular ion channel over period of time, which is essential for optical spectroscopy of embedded species. In most cases the time-of-flight was used for general diagnostics of the droplet beam composition and for recording mass spectra as it has a higher mass resolution when compared to the QMS (see Figure 2.13). Whilst efforts to achieve optical spectroscopy (see next section) with the reflectron time-of-flight mass spectrometer were pursued, no depletion in the total helium cation signal could be recorded. This was due to large fluctuations (> 20 %) in the He_n^+ ion signal, even over 300 shot averages, which gave rise to a relatively small (< 20 %) depletion effect and so the greater signal stability of the QMS was essential for recording optical depletion spectra.
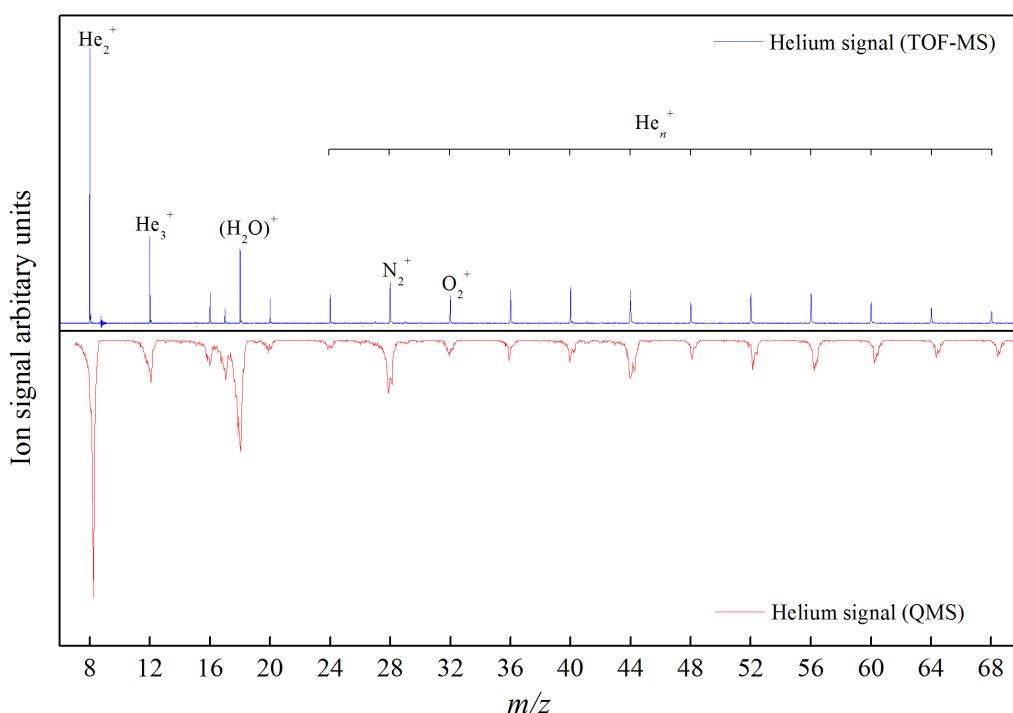
Figure 2.13. Comparison of mass spectra recorded on the TOF-MS (upper panel) and the QMS (lower panel). The helium stagnation conditions were 15 K and 20 bars.

2.4. OPTICAL SPECTROSCOPY OF DOPED HELIUM DROPLETS

The following sections will discuss the procedure and the equipment used for recording optical spectra of captured molecules and molecular clusters inside helium droplets. As the procedure for recording a depletion spectrum was very similar for both infrared and electronic spectroscopy, with the only difference being the different light sources, only a general procedure for recording optical spectra will be given.

2.4.1. Laser setup for electronic spectroscopy

A combination of a Nd:YAG laser (Continuum Surelite II -10) and a Sirah dye laser was used for generating tuneable visible and ultraviolet light for electronic depletion spectroscopy. The tuneability of a dye laser derives from the use of liquid organic dyes as the gain medium. A separate laser (Nd:YAG) is required to pump the

fluorescent dyes to induce a population inversion. A diffraction grating within the dye laser system allows for output at a specific wavelength with a reasonably narrow linewidth. Dye lasers are capable of producing an almost continuous range of colours, most of which are in the visible part of the spectrum. A frequency conversion unit (FCU) has been added to the dye laser to allow access to the near UV (220 – 440 nm) by frequency doubling of visible output from the dye laser.

A schematic of the laser setup for electronic depletion spectroscopy is shown in Figure 2.14. The helium droplet beam was intersected by an unfocused pulsed UV beam, operating at 10 Hz repetition rate, which was aligned anti-parallel to the helium droplet beam for maximum spatial overlap. The UV beam was aligned along a path directed into the centre of the pickup cell, using calcium fluoride prisms. The height of the beam was adjusted to match the height of the pickup cell with the use of a periscope, constructed using two additional CaF_2 prisms. To mark the path of the beam and to ensure that a good alignment could be achieved when the system was under vacuum, three irises were placed in tandem prior to the entrance of ionization region of the quadrupole mass spectrometer.
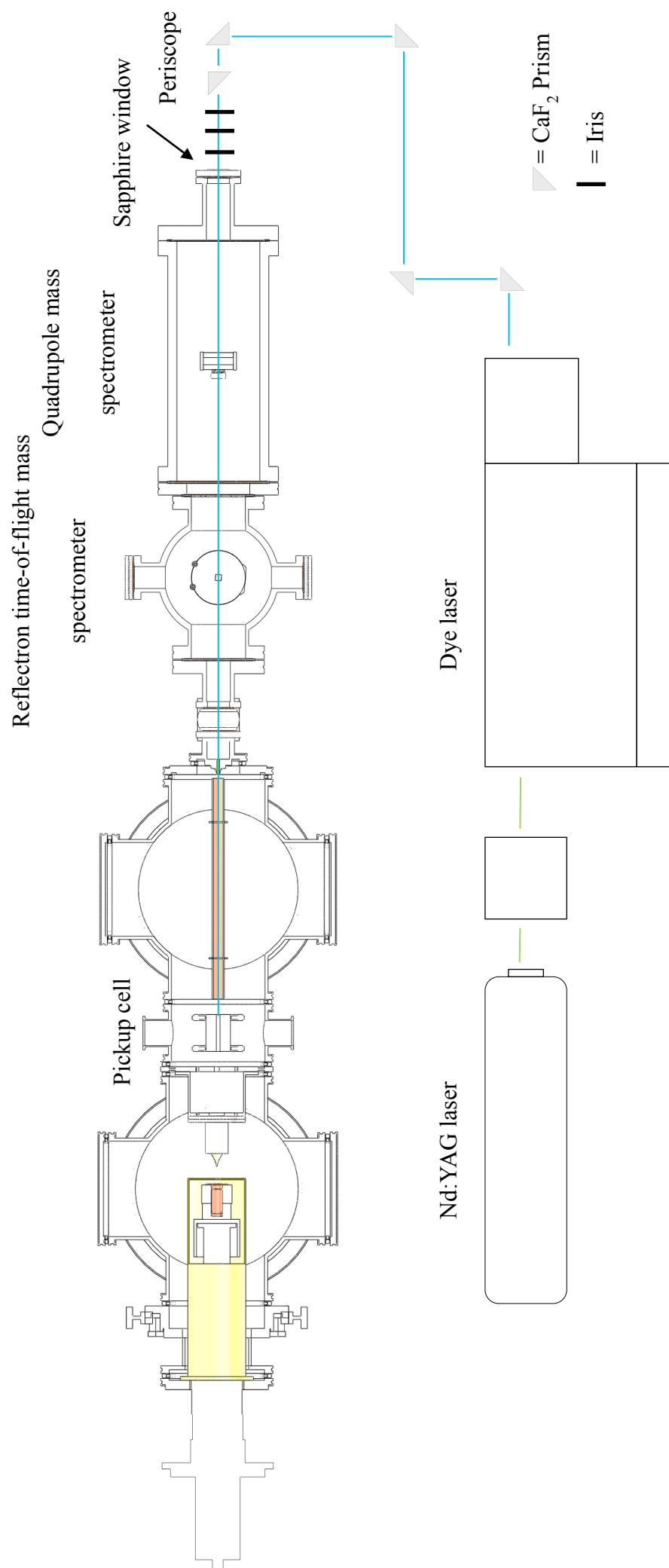
Figure 2.14. Schematic diagram of the laser setup used for electronic depletion spectroscopy.

Reflectron time-of-flight mass spectrometer

Quadrupole mass spectrometer

Sapphire window

Periscope

Pickup cell

Dye laser

Nd:YAG laser

= CaF$_2$ Prism

= Iris

2.4.2. Laser setup for infrared spectroscopy

An optical parametric oscillator/ amplifier (LaserVision, bandwidth 2.0 – 3.0 cm⁻¹) was used to generate infrared radiation for depletion type experiments accessing vibrational transitions. The use of the OPO/A allows for the, 1064 nm, fundamental output wavelength of a Nd:YAG laser (Surelite 1, 10 Hz), to be converted into tunable radiation in the mid-infrared. The OPO/A employed uses a combination of a 532 nm pumped OPO and a 1064 nm pumped OPA, which is capable of producing a tunable output from 710 to 885 nm in the near infrared, and from 1.35 to 5 μm, in the mid infrared, with the use of a single set of nonlinear crystals.

A schematic diagram of the laser setup for infrared depletion spectroscopy is shown in Figure 2.15. The 1064 nm output of the Nd:YAG laser is directed into the OPO/A with the use of two broadband metallic mirrors. The beam then passes through a beam splitter (BS1), which separates the horizontally polarized pump beam into two separate beams. One beam is directed towards a KTP crystal (C1), and is then frequency doubled and provides the 532 nm pump beam for the OPO stage, whilst the second 1064 nm beam is directed through a delay stage and goes on to the OPA. The 532 nm pump beam for the OPO is directed into the OPO cavity, which consists of a rear mirror (X1), an intra-cavity mirror set at 45 degrees for steering the 532 nm pump into the cavity (M2), an output coupler (X2) and a second KTP crystal (C2). In addition to the cavity optics a silver coated mirror (M5) is used to reflect any idler leaking through the rear mirror back towards the OPA. The KTP crystal (C2) used in the OPO cavity generates radiation at two different frequencies by a difference-frequency process. The higher of the two frequencies is termed the *signal* beam and is horizontally polarized, while the lower frequency portion is referred to as the *idler* and is vertically polarized.
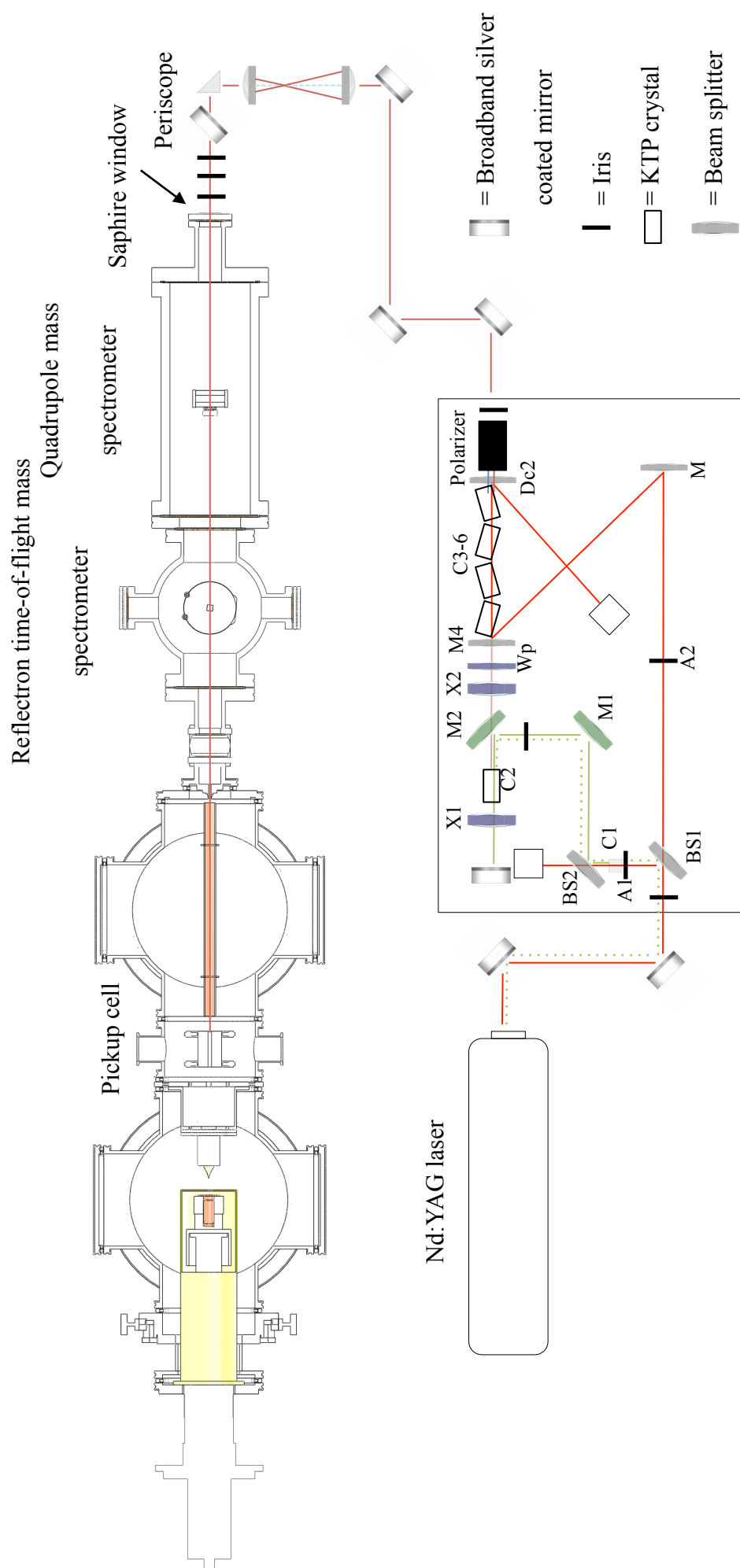
Figure 2.15. Schematic diagram of the laser setup used for infrared depletion spectroscopy.

49

Before entering the OPA stage the signal beam from the OPO is dumped and the polarization of the idler wave is flipped with the use of a variable half-wave plate (Wp). In the OPA stage the delayed 1064 nm pump beam is combined with the idler output from the OPO stage, which creates two additional signal and idler waves by a difference-frequency process. Upon exit of the OPA the residual 1064 nm pump, signal wave and idler wave pass through a dichroic, which removes the residual 1064 nm pump from the co-propagating signal and idler waves. The horizontally polarized signal and vertically polarized idler waves then pass through a Brewster 'stack of plates' polarizer, which depending on its orientation will isolate either the signal or idler wave from the combined output. For accessing the mid-infrared region, 2– 5 μm, the polarizer was orientated to allow the idler wave to exit.

The mid-infrared light generated by the OPO/A was then directed into the pickup region using silver coated broadband metallic mirrors (Newport, 25.4 mm diameter) and a periscope. The periscope is essentially the same as that described in the previous section, with the only substitution being the replacement of the top CaF_2 prism with a silver coated broadband metallic mirror. In order to achieve maximum spatial overlap of the helium droplet beam and the pulsed infrared beam the two beams were aligned antiparallel to one another, as in the electronic depletion spectroscopy experiments. As the path length of the IR beam from the OPO/A to the pickup region was rather long, ~3 m, and the IR beam was quite divergent, a telescope was placed just before the beam entered the periscope, to produce a narrow and more collimated beam. The telescope consisted of two CaF_2 plano-convex focusing lenses, with focal lengths of 10 and 20 cm. The two lenses were separated by 30 cm and orientated so that the IR beam would pass through the 20 cm focusing lens first, which reduced the beam size by approximately half.

2.4.3. Optical depletion spectroscopy

At present, the most commonly used technique for recording optical spectra of molecules and molecular clusters in helium droplets is the depletion technique. When a dopant within a helium droplet absorbs a photon a rapid transfer of energy from the dopant species into the helium droplet is possible, a result of redistribution of the absorbed photon energy as the excited molecules relaxes in the presence of the surrounding helium. This transfer of energy into the droplet generally leads to the evaporation of helium atoms from the droplet surface, which in turn reduces its ionization cross section.

To observe the reduction in the helium droplet ionization cross-section, the quadrupole mass spectrometer is set to record in single-ion-monitoring mode (SIM), which monitors the intensity of a specific ion channel over a period of time, and the laser is tuned into a particular vibrational or electronic transition. An example of the depletion in the ion signal of the mass channel 8, recorded by a SR430 multi-channel scaler and induced by laser excitation of a dopant, is shown in Figure 2.16.
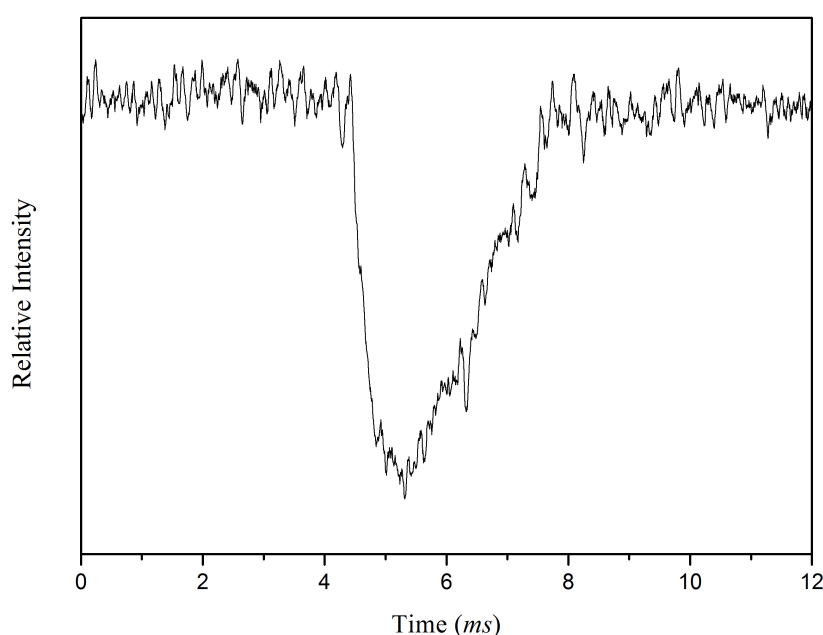
Figure 2.16. Depletion in the ion signal of the mass channel 8 recorded by a multi-channel scaler.

51

The dopant species shown in this example is water and the depletion arises as a result of tuning the OPO/A into the free OH stretching region of $(H_2O)_n$ clusters, specifically to 3730 cm^{-1}. The mass channel 8 was chosen for the SIM data acquisition as it corresponds to the He_2^+ ion, the predominant ion from electron impact ionization of a helium droplet, and is representative of a change in ionization cross section of the overall helium droplet. In most cases a depletion in the ion signal of all mass channels is observed, if transfer of the photon energy absorbed by the dopant into the droplet is efficient. The depletion in ion signal typically lasts for ~ 3 ms, which is roughly the time it takes for a doped droplet to travel from the pickup cell to the ionization region of the quadrupole mass spectrometer.

When recording an optical spectrum the signal intensity of a specific ion channel is monitored as a function of wavelength. To process the data an SR400 two-channel gated photon counter was employed. The SR430 was used only as a convenient means to check the strength of the depletion signal, which is dependent on the transfer of the photon energy absorbed by the dopant into the droplet, the laser alignment, the laser energy and the partial pressure of the dopant species. To prevent noise pulses from being counted the discriminator threshold, on both the SR430 and SR400, was set to -300 mV. A depletion spectrum was recorded by defining two gates of equal width, one to coincide with the depletion signal and another at a time prior to the depletion event to provide a background ion signal (typically obtained some 4 ms prior to firing of the laser). As the depletion in the ion signal typically lasts for ~3 ms a gate width of 2.5 ms was commonly used. For most experiments each point was averaged for 400 laser shots. A vibrational/ electronic depletion spectrum was obtained by subtracting the depleted ion signal from the background ion signal. The residual was then normalised by the

background in order to compensate for any fluctuations in the ion signal and to give the

best signal-to-noise ratio.

REFERENCES FOR CHAPTER 2

1. S. Yang, S. M. Brereton, A. M. Ellis, *Rev. Sci. Instrum.*, 2005, **76**, 104102.

2. M. Lewerenz, B. Schilling, and J.P. Toennies, *Chem. Phys. Lett.*, 1993, **206**, 381.

3. S. Yang, A. M. Ellis, *Rev. Sci. Instrum.*, 2008, **79**, 016106.

4. A. V. Kanaev, L. Museur, T. Laarman, M. C. Castex, S. Monticone, K. von Haeften and T. Möller, *J. Chem. Phys.*, 2001, **115**, 10248.

CHAPTER 3

THE FORMATION OF HELIUM CLUSTER CATIONS FOLLOWING THE IONIZATION OF HELIUM NANODROPLETS: INFLUENCE OF DROPLET SIZE AND DOPANT

This chapter presents details about the influence of helium droplet size and dopant species on the formation of helium cluster cations, following electron impact ionization of helium droplets. The effect of droplet size on the formation of pure helium cluster cations has been investigated by measuring the He_n^+/ He_2^+ ($n \geq 3$) signal ratio for droplet sizes between $\langle N \rangle = 4000$ to $\langle N \rangle = 80\ 000$ helium atoms. As the droplets become larger the He_n^+/ He_2^+ ($n \geq 3$) signal ratio increases until an asymptotic limit of $\langle N \rangle = 50\ 000$ helium atoms is reached. To explain this, a charge hopping mechanism where the positive charge is able to penetrate deeper into larger droplet sizes has been suggested. If the positive charge localizes to form He_2^+ further from the droplets surface, then the probability for collisions with surrounding helium as the ion leaves the droplet increases, resulting in the ejection of helium in the form of He_n^+ clusters as opposed to He_2^+. The effect of a dopant species was shown to alter the He_n^+/ He_2^+ ($n \geq 3$) signal ratio for smaller droplet sizes and was attributed to the potential energy gradient created by the cation-dopant interaction, and its potential to draw the positive charge towards the centre of the droplet.

3.1. INTRODUCTION

Over the past few decades, electron impact ionization has been used as a versatile tool in the study of helium nanodroplets.[1,2] One of the more common applications of the technique is to study the fragmentation patterns arising from both doped[3,4] and un-doped helium droplets.[5,6] Ions observed in the electron impact mass spectra can be formed by either charge transfer ionization[6] or by Penning ionization.[7] The mechanism for charge transfer ionization has been the focus of many experimental studies and is thought to occur by the following processes. Following electron impact ionization, with ionization energies > 24.6 ev, the initial event will most likely result in the ionization of a He atom to form He^+. The charge is then delocalised by a resonant charge hopping mechanism, which will terminate when the charge either localizes on the dopant (if one is present) or self-trapping of the positive charge occurs to form He_2^+.[6,8,9] If the helium droplets are exposed to electron energies lower than the ionization energy of helium (24.6 eV), then the helium atoms will become electronically excited and ionization of a dopant species will most likely occur by Penning ionization via meta-stable He^+ (2^3S), with an excitation energy of 19.8 eV.[10]

In the work presented here the aim was to investigate the formation of helium cluster cations, He_n^+, following electron impact ionization. As such, the discussion will focus on the charge transfer mechanism since helium cluster cations are unlikely to be formed by Penning ionization. Scifoni et $al.$[11] have modelled the formation of helium cluster cations, based on the He_2^+ + He system, and it was suggested that following self-trapping of the positive charge a vibrationally excited He_2^+ would form. Following its formation, the He_2^+ is then cooled by collisions with surrounding helium atoms and will act as a nucleation centre for the attachment of additional helium atoms, which will remain attached as the ion is ejected into the gas phase.

Callicoatt *et al*. have previously investigated the relative abundances of helium cluster cations with the use of electron impact ionization. In this investigation helium droplets containing a mean average of $<N>$ 100 to 15 000 helium atoms were used. The relative abundances of He_3^+ and He_2^+ can be obtained from Table I of Ref.6. From a plot of the He_3^+/He_2^+ ratio versus droplet size, a decline in the signal ratio was observed for droplet sizes containing more than $<N>$ 600 helium atoms and an approach towards an asymptotic limit was observed for the largest droplet sizes used, $<N> \sim$ 15 000. However, Callicoatt *et al*. mentioned that the largest helium droplets employed did not reach the "the large cluster limit" and that greater care should be taken to avoid contamination from background species, such as water.[6]

In this chapter, the relative abundances of helium cluster cations have been re-investigated for larger helium droplet sizes than those used by Callicoatt *et al*.[6] and the influence of dopant molecules on the relative abundances of helium cluster cations have been deliberately explored. In the case of pure helium droplets it was found that the He_3^+/He_2^+ ratio showed an opposite trend to that obtained from the abundances of He_3^+ and He_2^+ listed in Table 1 of Ref. 6. The addition of a dopant species was found to significantly alter the relative abundances of the helium cluster cations. For example, when water was used as the dopant species, the trend of the He_3^+/He_2^+ ratio compared very well to that observed by Callicoatt *et al*. for undoped helium droplets.

3.2. EXPERIMENTAL

The experimental apparatus has been described in detail in Chapter 2, and so only a brief description of the experimental procedure is given here. Helium droplets were produced using a pulsed valve and were detected with a reflectron time-of-flight mass

spectrometer, equipped with a 100 eV electron impact source.[12] The pulsed valve was operated with stagnation conditions of 10.5 K and 16 bars.

Since the aim of this work was to investigate the abundance of helium cluster cations for a range of helium droplet sizes, the use of a pulsed valve was more convenient than a continuous nozzle. This was because the droplet size could be selected by simply varying the delay between the firing of the pulsed valve and the pulsed extraction of the droplet beam.[13] This was preferable to changing the expansion conditions to vary the droplet size, as more time would have been required for the valve to equilibrate to each new set of expansion conditions. In all experiments mass spectra were recorded at 5 μs intervals to cover the full width of the gas pulse, which lasted for approximately 80 μs for a pulse opening time of 125 μs. This corresponded to droplet sizes consisting of $<N> = 4000$ to $<N> = 80\,000$ helium atoms, from the beginning to the end of the gas pulse respectively.[13]

The abundance of helium cluster cations (He_n^+) in a variety of helium droplet sizes was investigated by comparing the ratio between the ion signals of larger He_n^+ clusters and the He_2^+ in the mass spectra recorded at 5 μs intervals. In order to determine the influence of a dopant species on the abundance of helium cluster cations two further experiments were carried out, one with argon and a second with water as the dopant.

The amount of dopant species added into the droplet was gauged using the parent ion signal of the dopant species, e.g. H_2O^+ and Ar^+, in the background mass spectrum, which was recorded when the temperature of the pulsed valve was raised high enough to prevent droplet formation (> 25 K). The parent ion signals were then corrected for differences in their ionization cross sections to ensure the delivery of an equal partial pressure. The partial pressure was kept high enough to ensure that the smallest helium

droplets ($<N>$ = 4000) investigated in this work contained at least one atom or molecule.

In a previous study by Callicoatt *et al.* the abundance of helium cluster cations in helium droplets, containing a mean average of $<N>$ 100 to 15 000 helium atoms, was investigated with the use of electron impact ionization. In this experiment it was mentioned that larger helium cluster sizes should be explored and that care should be taken to avoid contamination by pickup of water vapour and other background gases.[6] Since the work reported in this chapter employed much larger helium droplets than those reported by Callicoatt *et al.*, considerable effort was made to reduce contamination from background gasses.

In order to prevent the pickup of residual water vapour, and to ensure a clean pickup of the dopant species, the system was baked for a week prior to each experiment. Also, when running the experiment, the liquid nitrogen trap was kept full to prevent any water vapour from being picked up downstream from the pickup cell. Figure 3.1 shows the mass spectrum of an un-doped helium droplet. The mass spectrum shows peaks arising from helium cluster cations, H_2O^+, O_2^+ and N_2^+. The H_2O^+, O_2^+ and N_2^+ peaks are presumably due to a small air leak in the mass spectrometer region as the H_3O^+, the major ion formed from the fragmentation of the water dimer, is negligible, which would be predominant if a significant amount of water was being picked up.
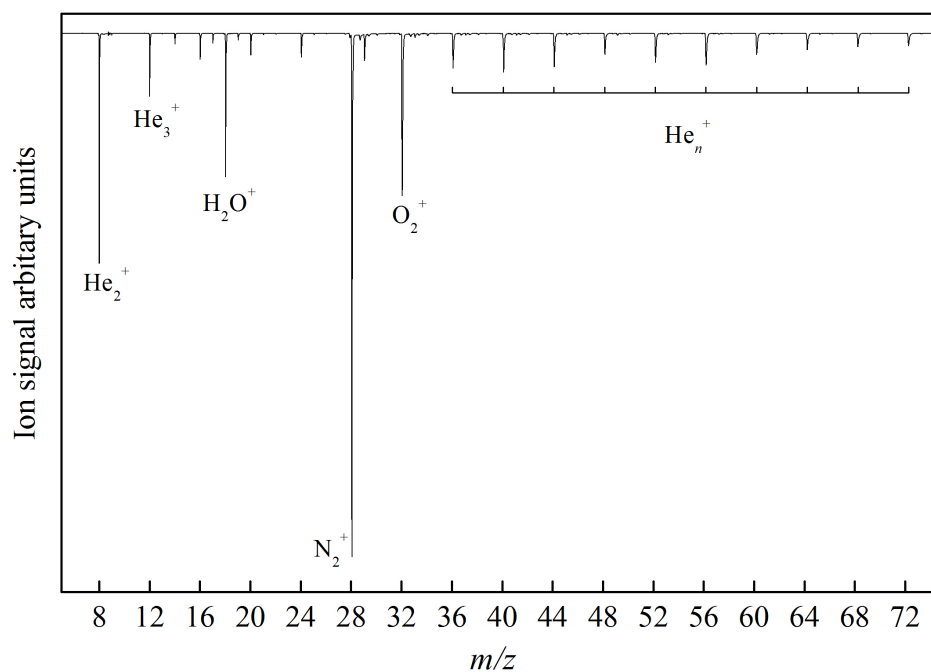
Figure 3.1. Background mass spectrum obtained before the addition of a dopant species. The peaks separated by 4 amu correspond to He_n^+ cluster ions.

To illustrate the cleanliness of the pickup process a mass spectrum showing the pickup of argon is shown in Figure 3.2.
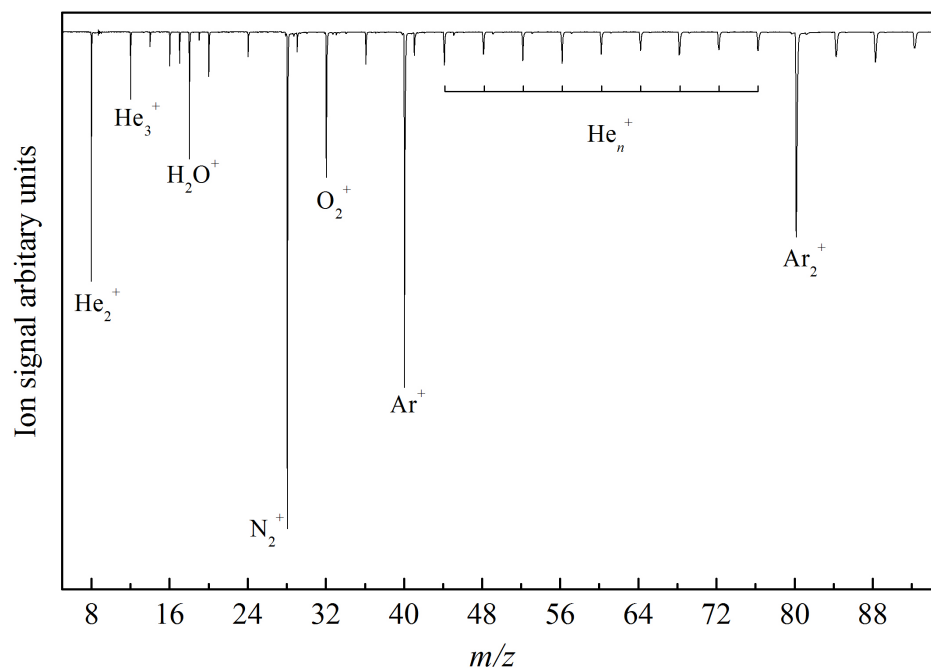
Figure 3.2. Mass spectrum recorded after the addition of argon. The pickup of argon is demonstrated by the appearance of Ar^+ and Ar_2^+ signals. The peaks separated by 4 amu correspond to He_n^+ cluster ions.

What is evident is that the intensity of the O_2^+, N_2^+ and the H_3O^+ peaks do not increase, which indicates that the argon gas line was sufficiently purged of water vapour and that all seals were leak tight.

It should also be noted that the ionization of large helium clusters containing small argon clusters ($m \leq 4$) rarely fragment to form Ar^+ and instead Ar_2^+ will be the primary fragment.[14] As such, the Ar^+ peak in the mass spectrum is mostly from background gas phase argon and the fragmentation of larger argon clusters. Figure 3.3 shows the change in the mass spectra following the addition of Ar atoms into the droplet.
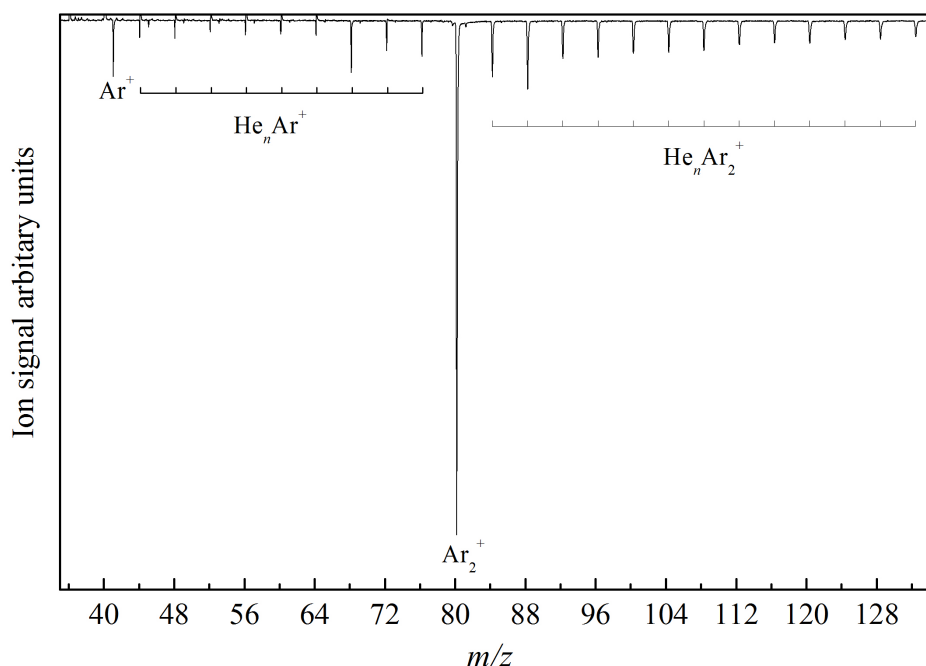
Figure 3.3. Mass spectrum of argon clusters in helium droplets obtained using the subtraction method described in the text.

The mass spectrum was obtained by subtracting (1) the background ion signal of argon and (2) the contribution from He_n^+ signals, in which the charge remained on the helium, from the argon doped mass spectrum shown in Figure 3.2. The figure shows that the Ar^+ peak is much weaker than the Ar_2^+ peak and reveals a broad distribution of

fragments of the type He_nAr^+ and $He_nAr_2^+$, which is consistent with a previous study by Janda *et al.*[14] The appearance of $He_nAr_m^+$ cluster ions become more predominant in larger helium droplets where the excess energy released into the droplets following the ionization of Ar_m^+ is insufficient to evaporate all of the helium atoms.[14]

3.3.   EXPERIMENTAL RESULTS

3.3.1. *The effect of droplet size on the He_n^+/He_2^+ signal ratio*

Figure 3.4 shows the effect of droplet size on the relative abundances of the He_n^+/He_2^+ ($n \geq 3$) signal ratios, observed in the electron impact mass spectra of un-doped helium droplets. The plot shows the ratio of the relative intensities of the helium trimer (He_3^+) and hexamer (He_6^+) ions to the dimer (He_2^+).
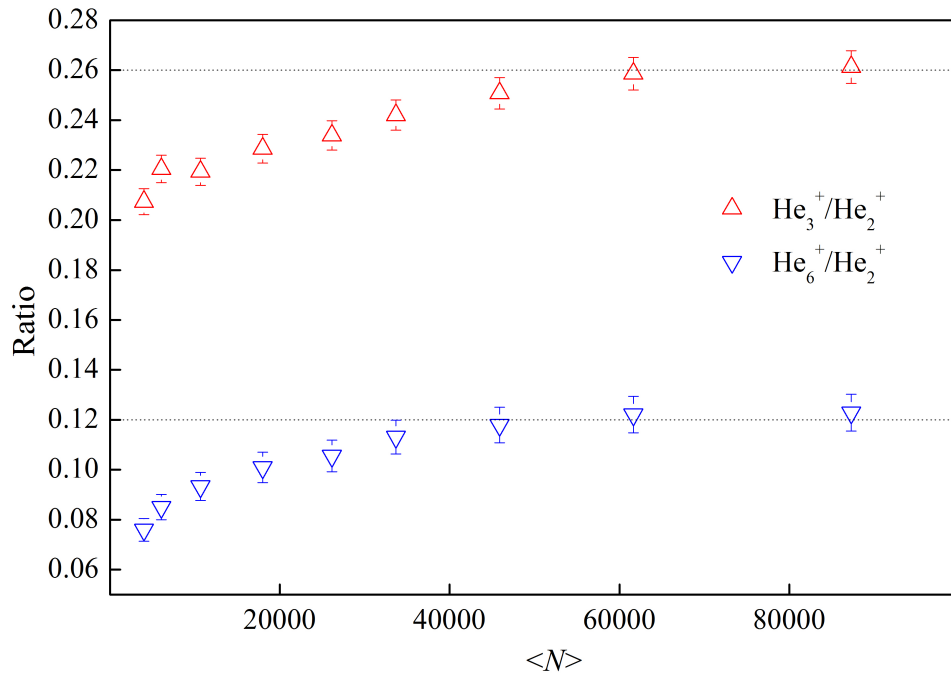
Figure 3.4. Relative abundance of He_3^+/He_2^+ and He_6^+/He_2^+ signal ratios with increasing droplet size, expressed as mean number of helium atoms $<N>$. The dashed lines represent asymptotic limits for large helium droplets. The error bars represent the standard deviation (1σ) of repeat measurements with the same conditions.

The hexamer was included to show that the variation of He_n^+/He_2^+ ratio continues for larger cluster ions. The helium tetramer (He_4^+) and pentamer (He_5^+) could not be used as a suitable comparison as the He_4^+ peak overlaps with traces of O^+, from fragmentation of background O_2, and the He_5^+ peak is affected by broadening of the wing of the H_3O^+ signal when H_2O is added to the system. The results from un-doped helium droplets show that, as the mean droplet size is increased, the He_3^+/He_2^+ and He_6^+/He_2^+ signal ratios both increase initially and then reach an asymptotic limit for helium droplets consisting of $<N> = 50\ 000$ helium atoms. The signal ratios increase from 0.20 to 0.26 for He_3^+/He_2^+ and from 0.05 to 0.12 for He_6^+/He_2^+.

3.3.2. The effect of a dopant species on the He_n^+/He_2^+ signal ratio

Figure 3.5 shows the influence of a dopant species on the He_3^+/He_2^+ signal ratio.
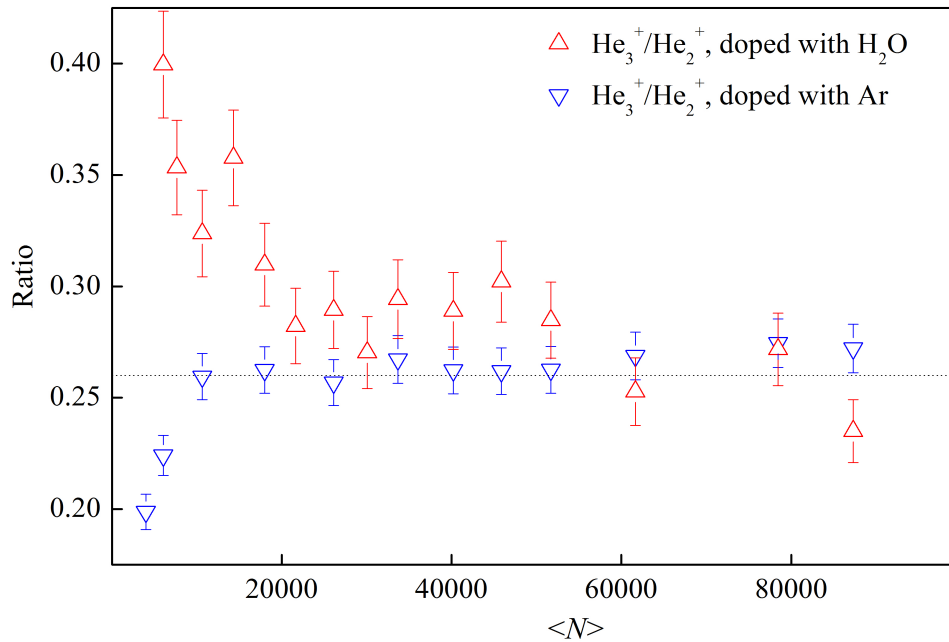
Figure 3.5. The dependence of the He_3^+/He_2^+ ratio on the helium droplet size when doped with H_2O (upper panel) or argon (lower panel). The dashed line represents the asymptotic limit for large helium droplets. The error bars represent the standard deviation (1σ) of repeat measurements with the same conditions.

The figure shows that the same asymptotic limit is reached for pure helium droplets regardless of whether argon or water is added, but it is evident that the addition of a dopant has a significant effect on the He_n^+/ He_2^+ signal ratio for smaller helium droplets. The first observation is that the asymptotic limit is reached for smaller droplet sizes when the droplets are doped compared to the pure helium droplets: In the case of argon the asymptotic limit is reached for droplet sizes containing as few as $<N> = 10$ 000 helium atoms. The second observation from Figure 3.5 is that the plots for water and argon doping approach the asymptotic limit from opposite directions. It should be mentioned that if the evaporation of helium atoms from the droplet surface, following the pickup of a dopant, were to have a significant effect on the He_n^+/ He_2^+ signal ratio, then it would be expected that the asymptotic limit would be reached for slightly larger droplet sizes. However, exactly the opposite is observed in practice, which suggests some alternative phenomenon is occurring here.

3.4.   DISCUSSION

In order to aid the interpretation of the experimental results a brief description of the charge transfer process, which occurs following electron impact ionization of a helium droplet, and the process for forming larger helium cluster cations, will be given first before the results presented above are discussed.

3.4.1. Charge transfer mechanism

Following electron impact ionization of a helium droplet the initial ionization event will produce a charged He^+, which is likely to reside close to the surface of the droplet. The charge is then delocalised by a resonant charge transfer process, in which the positive charge hops between adjacent helium atoms. The charge transfer process

will terminate when positive charge either localizes on the dopant (if one is present) or self-trapping of the positive charge occurs to form He_2^+. The energy released from the localization of the charge on the dopant or the formation of the helium dimer cation will serve to induce further fragmentation of the droplet. It should also be mentioned that, following the addition of a dopant species, a potential gradient will form between the positive charge and the dopant, which is expected to steer the positive charge towards the dopant species.[8] In the case of un-doped helium droplets the potential energy gradient that forms between the positive charge and the position of lowest potential energy, which is located at the droplets centre, is relatively weak and may not encourage the positive charge to travel towards the droplet centre; instead there is evidence that the charge hopping resembles a random walk.[8] The number of hops the positive charge makes before self-trapping to form He_2^+ occurs is of a finite length and is thought to be close to ~10 hops.[6,8,9] As such, if the dopant species is too far away from the droplet surface, ionization of the dopant will become unlikely.[8]

3.4.2. Formation of larger helium cluster cations

Although self-trapping of the positive charge will predominantly form a He_2^+, larger He_n^+ cluster ions are also observed in the mass spectrum (see Figure 3.1). Scifoni *et al*. have modelled the collisional relaxation dynamics following the formation of He_2^+ using the He_2^+ + He system as a basis for the model. In this work it was reported that the initial event, following self-trapping of the positive charge, would be the formation of a vibrationally excited He_2^+. Following its formation, the He_2^+ will be cooled by collisions with surrounding helium atoms and the He_2^+ will act as a nucleation centre for the attachment of additional helium atoms, which will remain attached as the ion is ejected into the gas phase.[11]

3.4.3. The effect of droplet size on the He_n^+ / He_2^+ signal ratio

From the above discussion, it is expected that the abundance of larger helium cluster cations will increase with the number of collisions with surrounding helium atoms. Consequently, the increase in the He_n^+/He_2^+ signal ratio (see Figure 3.4), before the asymptotic limit is reached, might be explained by the variation in the penetration depth of the incoming electron with droplet size. As the helium droplet size increases the possibility for the incoming electron to penetrate further inside the droplet, before ionization leads to He^+, increases. This will increase the probability that self-trapping of the He^+ ion to form He_2^+ will also occur deeper within the droplet. The greater the depth that self-trapping to form He_2^+ occurs, the more likely that larger cluster ions (He_n^+) will be produced by collisions with helium as the He_2^+ makes its exit from the droplet. The observation of an asymptotic limit for droplet sizes containing more than $<N> = 50\ 000$ helium atoms suggests that the incoming electron is not capable of penetrating any further than a certain distance into the droplet, and that further attachment of helium atoms would lead to the formation of an untouched core of liquid helium. Results from a previous study on the charge transfer mechanism have shown that the site for the initial ionization event to form He^+, following electron impact ionization, was found to become further from the droplet centre with increasing droplet size, which indicates that the incoming electron will penetrate the droplet to a finite depth.[8]

In a previous study by Callicoatt *et al*. the variation in the He_3^+/He_2^+ signal ratio, for helium droplets containing a mean average of $<N> = 100$ to $15\ 000$ helium atoms, can be obtained with the use of the relative ion yields of He_3^+ and He_2^+ listed in Table I of Ref.6. In contrast to the results shown in Figure 3.4 the He_3^+/He_2^+ signal ratio was found to decline as the droplet size increased and tended towards an asymptotic limit for the largest droplets used, $<N> \sim 15\ 000$. The difference between the He_3^+/He_2^+

signal ratios presented in this chapter and those obtained by Callicoatt *et al.*[6] might be explained by the pickup of impurities. For example, the results obtained for the water doping experiment, shown in Figure 3.5, show a similar trend to that reported by Callicoatt *et al.* (see Figure 3.6).
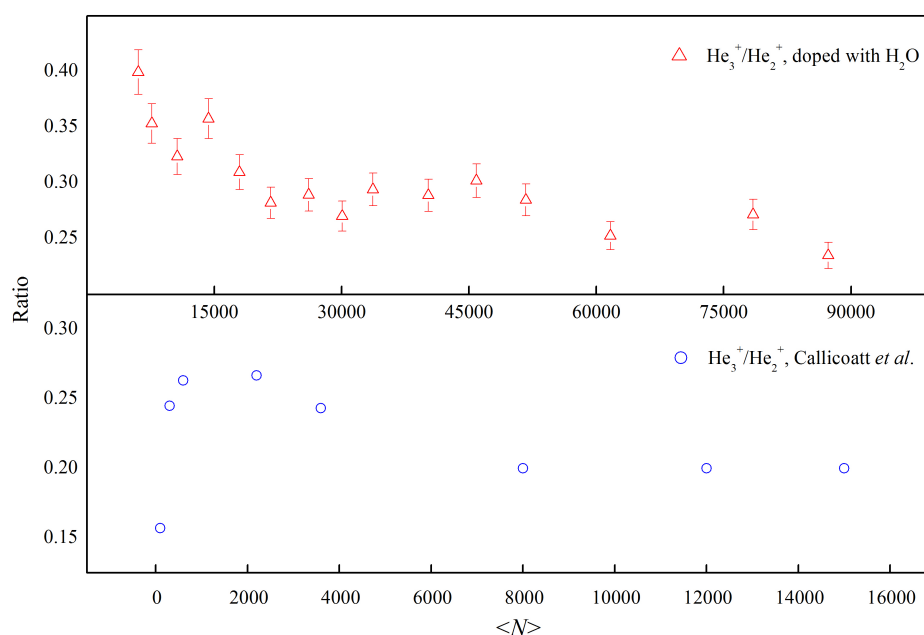
Figure 3.6. Comparison of the dependence of the He_3^+/He_2^+ ratio on the helium droplet size when doped with H_2O (upper panel) to the dependence of the He_3^+/He_2^+ signal ratios with increasing droplet size reported by Callicoatt *et al.* (lower panel).[6]

3.4.4. The effect of a dopant species on the He_n^+/He_2^+ signal ratio

Following the addition of a dopant two major differences were observed in the variation of the He_3^+/He_2^+ signal ratio with droplet size when compared to un-doped helium droplets (see Figures 3.5 and 3.4, respectively). The first was that the asymptotic limit was reached for smaller helium droplet sizes and the second was that argon and water approached the asymptotic limit from opposite directions.

In order to account for the increase in the abundance of larger helium cluster cations for smaller helium droplet sizes it implies that the presence of the dopant must

cause self-trapping of the positive charge to occur deeper inside the droplet. This can be explained by the potential energy gradient that will form between the dopant and the positive hole. Following the pickup of a dopant it is expected that it will reside close to the droplet centre, as this is the position of lowest potential energy. Following electron impact ionization and the formation of He^+ a potential energy gradient will form between the He^+ and the dopant, which will draw the He^+ deeper inside the droplet via a directed charge hopping process. This will increase the likelihood that self-trapping of the positive charge to form He_2^+ will occur deeper inside the droplet. As the initial location for self-trapping of the positive charge will be closer to the droplets centre it is expected that the He_2^+ will encounter more collisions with surrounding helium atoms, which will lead to an increase in the formation of larger helium cluster cations in smaller droplet sizes.[15]

The second observation, namely the approach to the asymptotic limit from opposite directions for Ar versus H_2O, can be explained by the stronger potential gradient formed between the dopant and the He^+. In this case it is not the interaction between the dopant and He^+ that is the important factor, but the interaction between the dopant and the He_2^+ formed after self-trapping of the positive charge. In order for helium cluster cations to be observed in the electron impact mass spectrum they must have gained enough kinetic energy to overcome the potential energy well that exists between He_2^+ and the dopant, otherwise they will be drawn back towards the dopant. If the latter occurs then it is expected that the He_2^+ would transfer its charge onto the dopant, due to the lower ionization energy of water and argon when compared to helium. For the helium cluster cations that are able to break free from the potential energy well, it is expected that they will travel at a reduced velocity as they make their

exit from the droplet, as a result of the energy expended when escaping the potential energy well between the dopant and the He_2^+.[15]

Whilst there have been no experimental studies on the impact the velocity of He_2^+ can have on association reactions to form He_n^+ clusters, there have been numerous studies on ion + molecule association reactions that show that the rate of reaction increases as the collision energy decreases.[16,17] If the same is true for association reactions in helium droplets then it is expected that the ability to form He_3^+ and larger He_n^+ clusters should increase if the He_2^+ travels through the droplet with a lower velocity. The potential gradient between the dopant and He_2^+ has a more significant effect on the He_n^+/He_2^+ signal ratio for smaller droplets, observed by the enhanced production of He_n^+ clusters, presumably due to the closer proximity of the He_2^+ to the dopant. As the droplet size becomes larger the ability of the dopant to affect the He_2^+ will decrease, a result of self-trapping to form He_2^+ occurring further away from the dopant, which explains the decline in the He_3^+/He_2^+ signal ratio with droplet size.[15]

3.5. CONCLUSION

To summarise, the variation of He_n^+/He_2^+ ($n \geq 3$) signal ratios in pure helium droplets have been found to increase with droplet size until an asymptotic limit is reached for droplets consisting of $<N> \geq 50\ 000$ helium atoms. The increase in the He_n^+/He_2^+ signal ratio is attributed to the ability of an incoming electron to penetrate further inside larger helium droplets before ionization occurs, which subsequently leads to self-trapping of He^+ to form He_2^+ deeper within the droplet. The greater the depth that self-trapping occurs, the higher the probability of increased collisions between helium atoms as the He_2^+ makes its exit from the droplet. The net effect is the preferential formation of larger cluster ions.

The addition of a dopant causes a strong potential energy gradient to be formed between the He^+ and the dopant, which acts to draw the He^+ closer to the centre of the droplet prior to self-trapping. This alters the He_n^+/He_2^+ signal ratio when compared to un-doped helium droplets and in some cases leads to a more rapid approach to the asymptotic limit. This effect was found to be more significant for water as opposed to argon.

REFERENCES FOR CHAPTER 3

1. J. P. Toennies, A. F. Vilesov, *Annu. Rev. Phys. Chem.,* 1998, **49**, 1.

2. J. P. Toennies, A. F. Vilesov, *Angew. Chem. Inst. Ed*. 2004, **43**, 2622.

3. J. Liu, B. Shepperson, A. M. Ellis, S. Yang, *Phys. Chem. Chem. Phys.*, 2011, **13**, 13920.

4. W. K. Lewis, B. E. Applegate, J. Szta ́ray, B. Szta ́ray, T. Baer, R. J. Bemish, R. E. Miller, *J. Am. Chem. Soc.*, 2004, **126**, 11283.

5. H. Buchenau, E. L. Knuth, J. Northby, J.P. Toennies, C. Winkler, *J. Chem. Phys.*, 1990, **92**, 6875.

6. B.E. Callicoatt, K. Förde, L. Jung, T. Ruchti, and K. C. Janda, *J. Chem. Phys.*, 1998, **109,** 10195.

7. A. Scheidemann, B. Schilling, and J. P. Toennies, *J. Phys. Chem.*, 1993, **97,** 2128.

8. A. M. Ellis, S. Yang, *Phys. Rev. A*., 2007, **76**, 032714.

9. B.E. Callicoatt, D. D. Mar, V. A. Apkarian, and K. C. Janda, *J. Chem. Phys.*, 1996, **105,** 7872.

10. H. Schöbel, P. Bartl, C. Leidlmair, M. Daxner, S. Zöttl, S. Denifl, T. D. Märk, P. Scheier, D. Spångberg, A. Mauracher, and D. K. Bohme, *Phys. Rev. Lett*., 2010, **105,** 243402.

11. E. Scifoni, E. Bodo, G. Dellepiane, and F. A. Gianturco, *Eur. Phys. J. D*., 2004, **30,** 363.

12. S. Yang, S. M. Brereton, A. M. Ellis, *Rev. Sci. Instrum.*, 2005, **76**, 104102.

13. S. Yang, A. M. Ellis, *Rev. Sci. Instrum.*, 2008, **79**, 016106.

14. B.E. Callicoatt, K. Förde, T. Ruchti, L. Jung, and K. C. Janda, *J. Chem. Phys.*, 1998, **108,** 9371.

15. B. Shepperson, J.Liu, A. M. Ellis, S. Yang, *J. Chem. Phys.*, 2011, **135**, 041101.

16. P. A. M. van Koppen, M. F. Jarrold, M. T. Bowers, L. M. Bass, K. R. Jennings, *J. Chem. Phys.*, 1984, **81**, 288.

17. R. Johnsen, A. Chen, M. A. Biondi, *J. Chem. Phys.*, 1980, **73**, 1717.

CHAPTER 4

CORE-SHELL EFFECTS IN THE IONIZATION OF DOPED HELIUM

NANODROPLETS

This chapter presents details about the formation of core-shell particles within helium droplets. Core-shell particles, consisting of a water core and an outer shell of a co-dopant, were formed using a sequential pickup technique, in which water and a co-dopant were added in specific doping orders. The co-dopants used for this investigation were Ar, O_2, N_2, CO, CO_2, NO and C_6D_6. The aim of the experiment was to assess how a variety of co-dopants, with different properties, would affect the ionization of water cluster ions by charge transfer. If the presence of a particular co-dopant reduced the fragmentation of the parent ion $((H_2O)_n^+)$ to form $(H_2O)_{n-1}H^+$ then it was taken to represent a softening of the ionization process. Of the co-dopants used N_2, O_2, CO_2 and C_6D_6 were found to stabilize the formation of $(H_2O)_n^+$, which was attributed to the co-dopant forming a protective outer shell around the water cluster core. Whilst for CO and NO the discussion was complicated due to secondary reactions to form HONO and HOCO, which favor the fragmentation of some water cluster sizes to form $(H_2O)_nH^+$. The results from *ab initio* calculations of $[X(H_2O)_2]^+$ cluster ions support the experimental observations and suggest that when X = of Ar, N_2 and CO_2 the lowest energy dissociation process would be the loss of X, a process which would cool the remaining $(H_2O)_2^+$ and increase the likelihood that the unprotonated water dimer cation will survive the ionization process. Whilst for CO, on purely energetic grounds, the loss of HOCO rather than CO would be the preferred fragmentation process.

4.1. INTRODUCTION

The use of helium droplets for the study of molecules and molecular clusters at very low temperatures has become increasingly popular over the past few years. This is largely due to the unique properties possessed by the droplets, which include an extremely low equilibrium temperature (0.37 K), high thermal conductivity and their ability to rapidly dissipate excess energy through the evaporative loss of weakly bound helium atoms.[1,2] The unique environment provided by the droplet not only allows for a convenient means to probe individual molecules and molecular clusters with spectroscopic techniques, such as mass spectrometry and infrared spectroscopy, but can also be used as a medium to tailor molecular aggregates. Recently the use of infrared spectroscopy has revealed that unique structures can form within the droplet as a result of the interactions between the dopant molecules.[3-6]

Whilst the mechanism for charge transfer ionization has been extensively studied for a single dopant,[7,8] there have been fewer investigations into the mechanism following electron impact ionization of mixed dopants. One of the earliest experiments to study mixed dopants was carried out by Fárnik et al. and investigated ion-molecule reactions between $N_2^+ + D_2$, $CH_4^+ + D_2$ and $CH_3^+ + D_2$.[9] The experiments were carried out with the use of electron impact ionization mass spectrometry and revealed that both reaction intermediates and end products were observed in the mass spectra. In a more recent study carried out by Ren et al.[10] water was co-added to helium droplets containing fragile organic molecules. It was found that the presence of water significantly reduced the degree of fragmentation of the organic molecules, which was attributed to the ability of the water clusters to *soften* the ionization process. The softening effect of the water was found to be more effective when organic molecules with low or zero dipole moments were used. This was attributed to the potential

gradient that forms between the water and the positive charge, which will steer the positive charge towards the water. If the water clusters are ionized prior to the organic molecules then it is expected that some of the excess energy will be dissipated prior to charge transfer onto the organic molecules.

In a similar experiment, Lewis *et al*. reported that the co-addition of two different species could lead to the formation of core-shell structures in helium droplets.[11] In this study triphenylmethanol (TPM) was co-added with various amounts of neon atoms. As the amount of neon was increased a reduction in the fragmentation of the parent ion of TPM was observed. This was attributed to a softening effect caused by the neon atoms forming a protective shell around the TMP molecule. By monitoring the intensity of the TPM parent ion it was found that an asymptotic limit was reached following the addition of 20 neon atoms, which was interpreted as the formation of a complete outer shell of neon atoms around the TPM molecule.

In this chapter, electron impact ionization has been used to investigate mixed molecule systems. The aim of the work was to investigate whether core-shell particles consisting of two different components can be formed in helium droplets, and then explore the effect on the ion-molecule chemistry. Core-shell particles were formed using a sequential pickup technique, which relies on the unique ability of the helium environment to rapidly cool the dopant molecules. In contrast to previous studies the work presented here also investigates the effect of forming core-shell structures that are capable of *chemically interacting*.

In this study, water clusters were chosen as one of the reactive species as their corresponding cations have been extensively studied. Water cluster cations $(H_2O)_n^+$ ($n = 2, 3, 4 \ldots$) are readily formed by electron impact ionization of neutral water clusters, however they are very unstable as they are formed in highly vibrationally excited

states.[12] As a result, unprotonated clusters are not observed in gas-phase ionization experiments as the $(H_2O)_n^+$ readily fragment to form protonated water cluster ions $((H_2O)_{n-1}H^+)$. In order for unprotonated water clusters ions to survive the ionization process the excess energy deposited into the vibrational degrees of freedom of the parent ions must be rapidly quenched. Previous studies have shown that this can be achieved by seeding water with argon[13] or by using helium nanodroplets.[14] However, in either case, water cluster ion fragmentation is still the dominant reaction pathway. The ability to monitor the abundance of the water cluster ions is advantageous for this work as it provides a convenient measure to determine the effect of a co-dopant shell around the water clusters. This is because if the abundance of the unprotonated channel increases with respect to the corresponding protonated channel it implies that the co-dopant must provide additional quenching.

In this work, water clusters were combined with a variety of co-dopant species including Ar, O_2, N_2, CO, NO, CO_2 and C_6D_6. These species were chosen as they cover both monatomic and polyatomic species, and gave access to a distribution of ionization energies, with some lying above and some below that of water. Of the co-dopants used N_2, O_2, CO_2 and C_6D_6 were found to stabilize the formation of $(H_2O)_n^+$, which was attributed to the co-dopant forming a protective outer shell around the water cluster core. Whilst for CO and NO the discussion was complicated due to secondary reactions to form HONO and HOCO, which favor the fragmentation of some water cluster sizes to form $(H_2O)_nH^+$. The formation of a core-shell structure was established by reversing the pickup order of the addition of water and O_2. In a subsequent experiment the amount of O_2 molecules required to complete an outer shell around the water clusters was determined by keeping the partial pressure of water fixed whilst the O_2 partial pressure was varied. In order to aid the interpretation of the experimental results *ab*

initio calculations were performed on $[X(H_2O)_2]^+$ cluster ions. The specific aim of these calculations was to provide an insight into the mechanism behind the increase/decrease of the branching ratios, of water cluster ions in the electron impact mass spectra, when water is co-added with another species. To reduce the computational load, calculations were performed on the water dimer and its complexes formed with various co-dopant molecules. The results from these calculations were taken to be representative of larger water cluster sizes. The co-dopants used were Ar, N_2, CO and CO_2. O_2 and benzene were omitted from the calculations, as their ionization energies are lower than that of H_2O and charge transfer from He^+ to O_2 or benzene is expected on ionization. NO was also not included for the same reason as O_2 and benzene and because of secondary reactions to form HONO for some water cluster sizes. The calculations focus on the binding energies of $X{\cdots}(H_2O)_2{}^+$, where X is one of Ar, N_2, CO and CO_2, and the effect of a co-dopant on the binding energy of the $OH{\cdots}HOH_2{}^+$.

4.2. EXPERIMENTAL

The details of the experimental apparatus are provided in Chapter 2 and only a brief account of relevant experimental procedures are presented here. Helium droplets were produced using a pulsed helium droplet source and were detected with a reflectron time-of-flight mass spectrometer, equipped with a 100 eV electron impact source.[15,16] The pulsed valve was operated with stagnation conditions of 15 K and 20 bars, which gave droplet sizes containing an average size of $<N> = 7500$ helium atoms. In order to ensure that two different dopant species would be picked up sequentially, the dopants were introduced into two separate pickup cells placed in tandem.

In most experiments water was added to the first pickup cell and its partial pressure was carefully monitored to ensure the pickup of at least three water molecules.

A co-dopant, selected from one of Ar, O_2, N_2, CO, CO_2, NO and C_6D_6, was added into a second pickup cell, which was located downstream from the first. Water was added into the first pickup cell to ensure that water clusters would aggregate first, enabling the addition of a co-dopant to form a core-shell structure with a water core and a co-dopant shell. Similarly, reversal of the pickup order should lead to a core-shell structure with a co-dopant core and a water shell. Small water cluster sizes were used to ensure that the co-dopant would surround the water clusters.

Whilst the formation of core-shell structures inside helium droplets have been observed previously,[11] another possible outcome is that a core-shell structure will not form at all and instead the water and the co-dopant will aggregate separately and attach to each other as an aggregate. If this occurs then identical mass spectra should be obtained regardless of the pickup order. However, if a core-shell structure is formed then it is expected that the presence of the co-dopant will alter the fragmentation pattern for water clusters, which would produce distinct mass spectra when the order in which the dopants are added is reversed.

In order to verify that a core-shell structure was being formed, two separate experiments were carried out. In the first experiment H_2O was added prior to O_2 and in the second experiment the pickup order was reversed. In both experiments the vapour pressure of water was optimised to ensure the pickup of at least 3 water molecules and the partial pressure of O_2 was applied at an O_2/H_2O ratio of 20, to ensure that O_2 would form at least a partial outer shell around the water clusters. Subsequently, a further experiment was also performed to determine how many O_2 molecules would be required to form a complete outer shell around a water cluster core. In this experiment the partial pressure of water was kept fixed whilst the partial pressure of O_2 was varied for a range of O_2/H_2O ratios up to 35.

The amount of dopant species added into the droplet was gauged using the parent ion signal of the dopant species, e.g. H_2O^+ and O_2^+, in the background mass spectrum, which was measured 1 ms prior to the arrival of helium droplets in the ionization region of the reflectron time-of-flight mass spectrometer. Figures 4.1 and 4.2 show mass spectra recorded at different time delays to show that the background mass spectrum was free from any contribution from helium droplets.
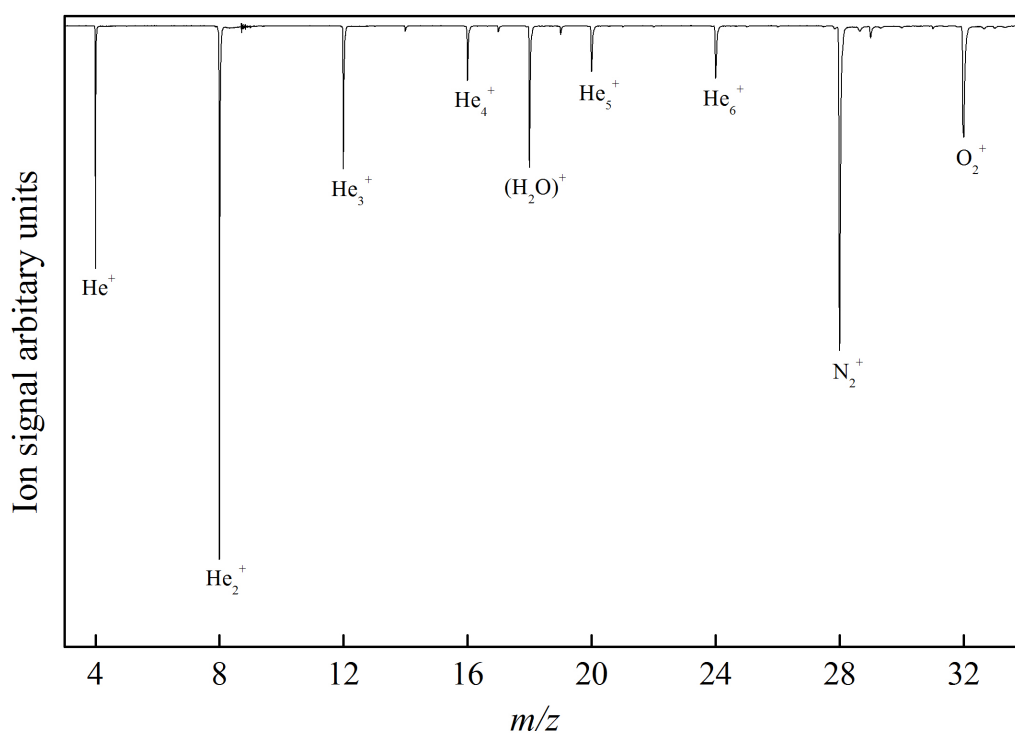
Figure 4.1. Electron impact mass spectrum of pure helium droplets, recorded when the electron beam was set to fire when helium droplets were present. The presence of H_2O^+, N_2^+ and O_2^+ peaks are presumably due to a small air leak in the mass spectrometer region.
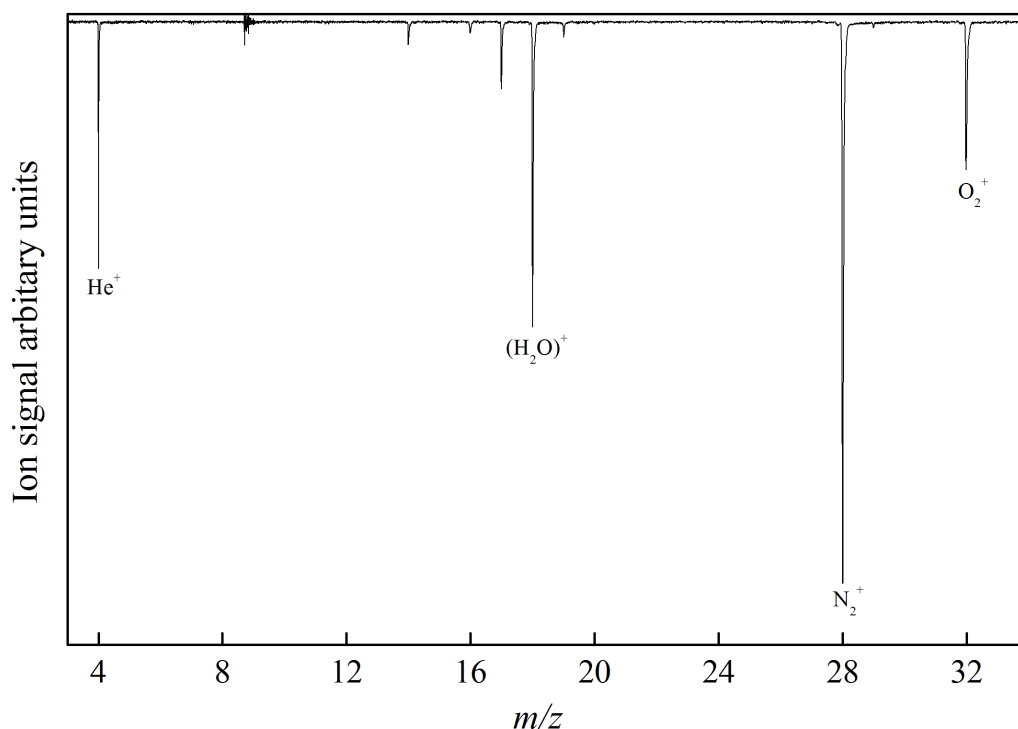
Figure 4.2. Electron impact mass spectrum of pure helium droplets recorded when the electron beam was set to fire when no helium droplets were present. The spectrum shows that peaks from He_n^+ clusters are no longer present, as expected in the absence of helium droplets (He^+ peak is still present because of trace gas phase helium entering the ion source).

A disadvantage of using the parent ion signal of the co-dopant to gauge how much co-dopant was added is that different co-dopants cannot be quantitatively compared by their parent ion signal intensity alone. This is because different species will have different ionization cross-sections and fragmentation of the parent ion will also vary for different species. In order to directly compare the same amount of co-dopant, the parent ion signal (I) of the co-dopant was multiplied by its ionization cross-section (σ) and the percentage of the parent ion (P) in the gas phase electron impact mass spectrum. The values for the ionization cross-section and the percentage of the parent ion signal in the electron impact mass spectrum were calculated for an electron impact energy of 100 eV and were obtained from the NIST Chemistry WebBook.[17]

In most experiments the amount of co-dopant added into the droplet was made deliberately high to give a co-dopant/H_2O parent ion signal ratio of 40. This was done to ensure that there would be a sufficient amount of the co-dopant to form a complete outer shell around the water clusters. The only exception to this was when deuterated benzene was used. In this experiment the deuterated benzene was administered so that the $C_6D_6^+$ and the H_2O^+ parent ion signals were approximately the same. This was because the water cluster ions would disappear following the addition of high levels of deuterated benzene, and the deuterated benzene cluster ions would become the dominant feature in the mass spectrum (see Figure 4.3). This was presumably due to the lower ionization energy of deuterated benzene when compared to water, which increases the likelihood that the charge would reside on the deuterated benzene following charge transfer from He^+. Although the amount of deuterated benzene added was not sufficient to form a complete outer shell around the water clusters, it is likely that the amount added will at least partially surround the water clusters.
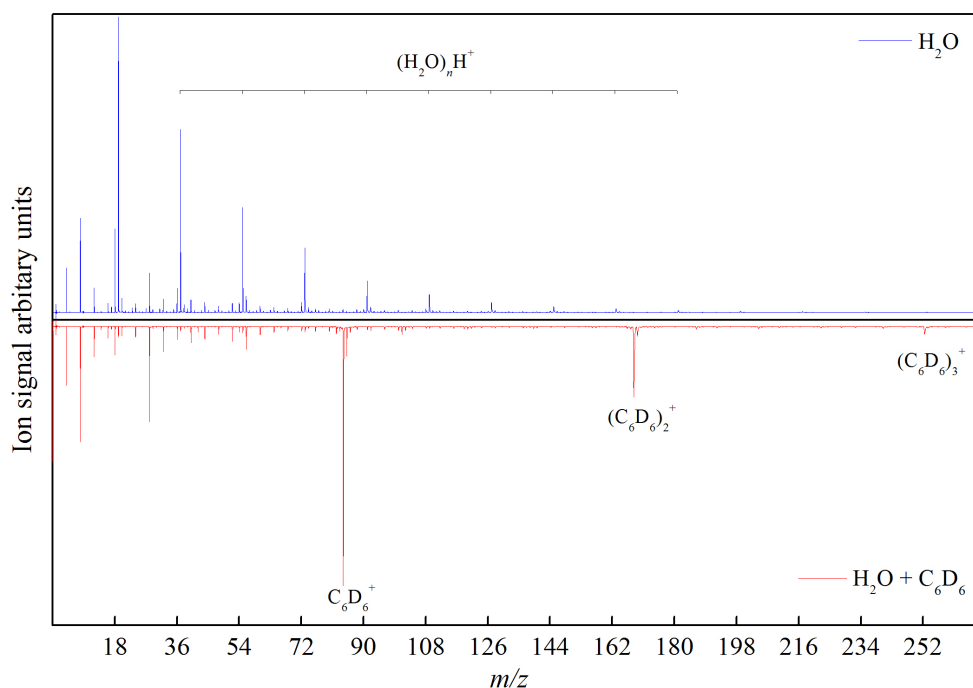
Figure 4.3. Comparison of mass spectra of recorded with and without C_6D_6.

4.3.   COMPUTATIONAL DETAILS

In order to aid the interpretation of the experimental results *ab initio* calculations were performed using MP2 methodology along with an aug-cc-pVTZ basis set. Calculations were initially performed on the water dimer ion $(H_2O)_2^+$, which was subsequently used to construct the initial geometries of the various $[X(H_2O)_2]^+$ cluster ions. Various theoretical investigations have suggested three possible structures for the $(H_2O)_2^+$.[18,19] The three structures include a hydrazine-like configuration, which is the global minimum structure, a gauche orientated dimer and a disproportionated ion, $HO\cdots HOH_2^+$. Since ionization of water will involve a rapid proton transfer, which leads to charge localization on an H_3O^+ moiety, the disproprtionated ions will be the only product following electron impact ionization of water clusters. This has been established in an Ar-tagging experiment by Gardenier *et al.*[20] Consequently, only the geometry of the disproportionated ion was used in this in this study. All of the possible binding sites for a co-dopant, X, attached to the $OH\cdots HOH_2^+$ were investigated. In order to verify if a true minima had been found vibrational frequencies calculations were carried out on the optimised structures. In order to calculate binding energies of $HO\cdots HOH_2^+$ and $(H_2O)_2^+\cdots X$, basis set superposition error (BSSE) corrections using the standard counterpoise correction procedure were employed. The binding energy was then obtained from the formula $\Delta E_{AB} = E_{AB} + \text{BSSE} - (E_A + E_B)$,[21] where E_{AB}, E_A and E_B are the total energies of molecule/cluster AB and A and B are the corresponding fragments.[22] All of the calculations presented here were performed using GAUSSIAN 03 and were run on ALICE, the high performance computing (HPC) cluster, at the University of Leicester.

4.4. EXPERIMENTAL RESULTS

4.4.1. Water clusters

Figure 4.4 shows the electron impact mass spectrum of pure water clusters inside helium droplets. The spectrum shows an even distribution of peaks separated by 18 m/z. The predominant peaks in the spectrum arise from protonated water cluster ions $((H_2O)_n H^+)$ and the weaker shoulder peaks correspond to unprotonated water cluster ions $((H_2O)_n^+)$, which is consistent with a previous study by Yang et $al.$[14] As the ionization of water clusters inside a helium droplet will occur by a charge transfer mechanism, in which the initial ionization event leads to the formation of He^+,[23,24] the dominant protonated water cluster ions will most likely form by the following reaction pathway

$$(H_2O)_n + He^+ \rightarrow H^+(H_2O)_{n-1} + OH + He \qquad (4.1)$$
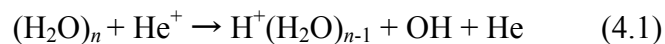
The appearance of unprotonated water clusters is a result of the ability of the helium droplet to rapidly quench the excess energy deposited into the water cluster following ionization by charge transfer. This rapid quenching of the $(H_2O)_n^+$ is possible because of the droplets extremely low equilibrium temperature (0.37 K), high thermal conductivity, and its ability to rapidly dissipate excess energy through the evaporative loss of weakly bound helium atoms.[14,24] As such, the formation of the $(H_2O)_n^+$ will most likely form by the following reaction pathway

$$(H_2O)_n + He^+ \rightarrow (H_2O)_n^+ + He \qquad (4.2)$$
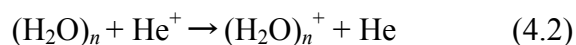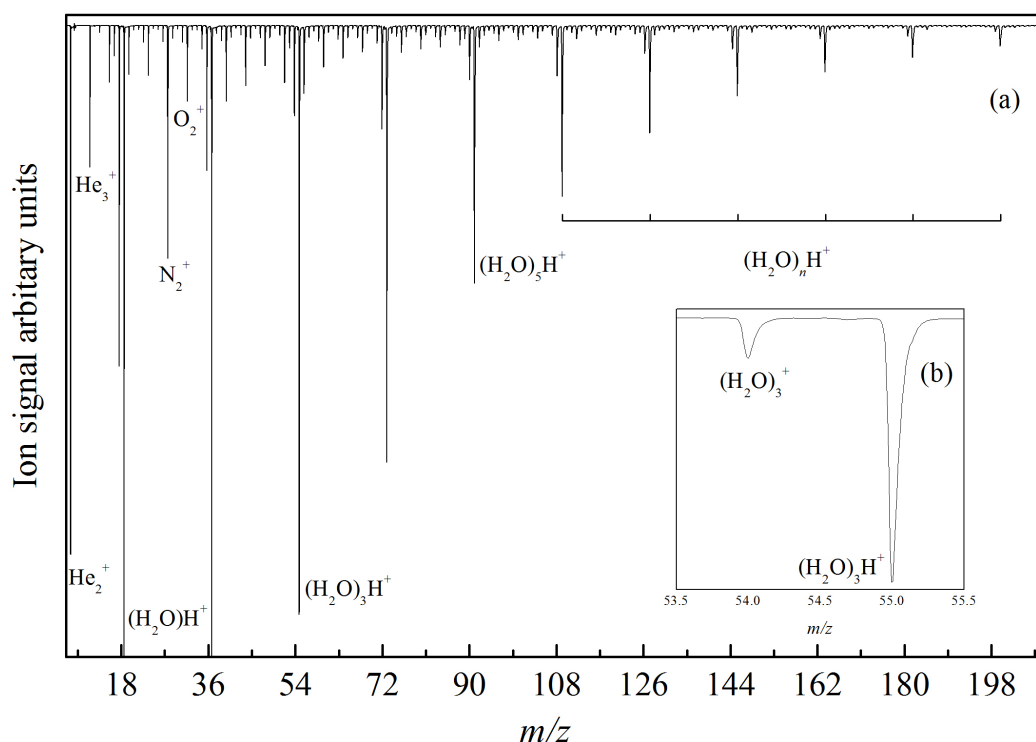
Figure 4.4. Electron impact mass spectrum of helium droplets doped with water. The predominant peaks in the spectrum are derived from protonated water cluster ions $(H_2O)_nH^+$. To the immediate left of every protonated water cluster ion is a weaker peak, which corresponds to un-protonated water cluster ions, $(H_2O)_n^+$.

4.4.2. Binary water clusters: water and a co-dopant

Figure 4.5 shows the electron impact mass spectrum when O_2 is co-added to water clusters inside helium droplets. The water vapour pressure was kept constant to ensure the pickup of at least three water molecules and the partial pressure of O_2 was administered to give an O_2/H_2O parent ion signal ratio of 20, which corresponds to the addition of approximately 60 oxygen molecules. The mass spectrum shows ion signals due to protonated water cluster ions ($(H_2O)_nH^+$), unprotonated water cluster ions ($(H_2O)_n^+$) and binary cluster ions (O_2-$(H_2O)_n^+$). In subsequent experiments, where Ar, N_2, CO, CO_2, NO and C_6D_6 were co-added to water clusters, a similar response was observed in the corresponding mass spectra (see Appendix A).
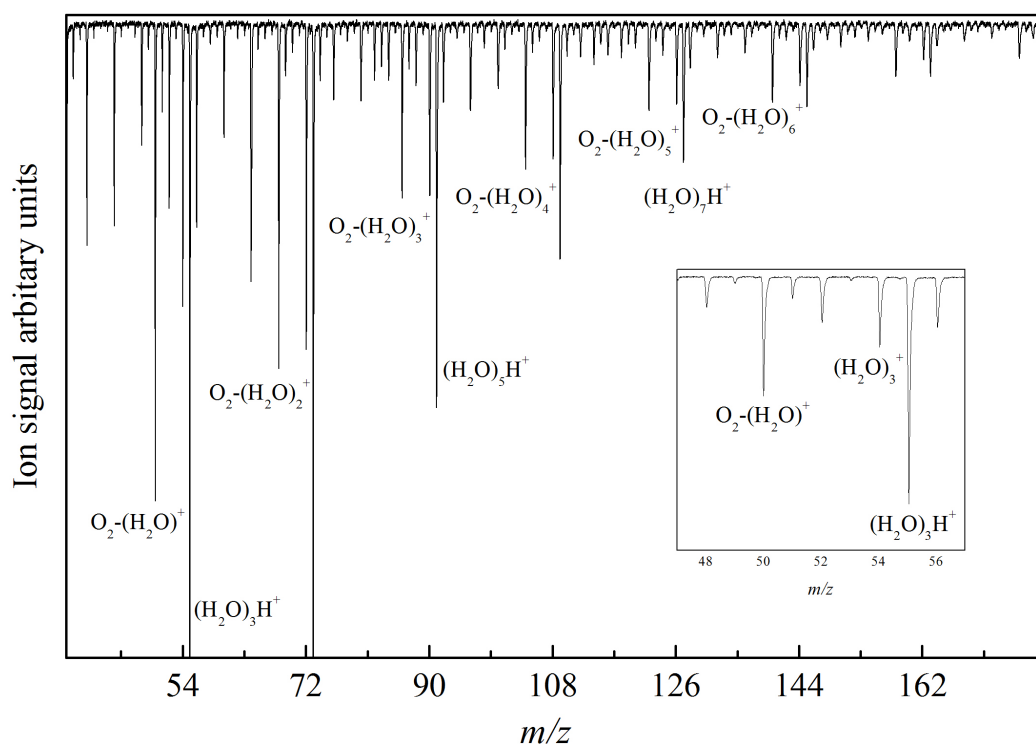
Figure 4.5. Electron impact mass spectrum of helium droplets doped with water and O_2. Pure water cluster ions ($(H_2O)_n^+$ and $(H_2O)_nH^+$) and peaks corresponding to binary cluster ions, consisting of O_2 and water (O_2-$(H_2O)_n^+$), are observed in the spectrum.

The presence of O_2 also seems to increase the $(H_2O)_n^+/(H_2O)_nH^+$ signal ratios when compared to the $(H_2O)_n^+/(H_2O)_nH^+$ signal ratios observed in the pure water mass spectrum. For example, the $(H_2O)_3^+/(H_2O)_3H^+$ signal ratio increases from 0.15 to 0.30 following the addition of O_2. A similar observation was made when C_6D_6, CO_2, and N_2 were used as the co-dopant, whereas for Ar no significant difference in the $(H_2O)_n^+/(H_2O)_nH^+$ signal ratio was observed. However, when CO and NO were used the opposite effect was observed, and the $(H_2O)_n^+/(H_2O)_nH^+$ signal ratio was found to decrease for some cluster sizes.

The variation in the $(H_2O)_n^+/(H_2O)_nH^+$ signal ratio could be an indication that the presence of a particular co-dopant can either decrease or increase the formation of $(H_2O)_n^+$ when compared to $(H_2O)_nH^+$ following the ionization of water clusters by

charge transfer in helium nanodroplets. Consequently, if the $(H_2O)_n^+/(H_2O)_nH^+$ signal ratio is dependent on the order in which dopants are picked up then it could also be used to determine whether core-shell structures are formed.

4.4.3. Core-shell structure – identification

Evidence for the formation of core-shell structures (II and III in Figure 4.6) as opposed to the formation of homogeneous clusters consisting of water and the co-dopant (I in Figure 4.6) is shown in Figure 4.7.
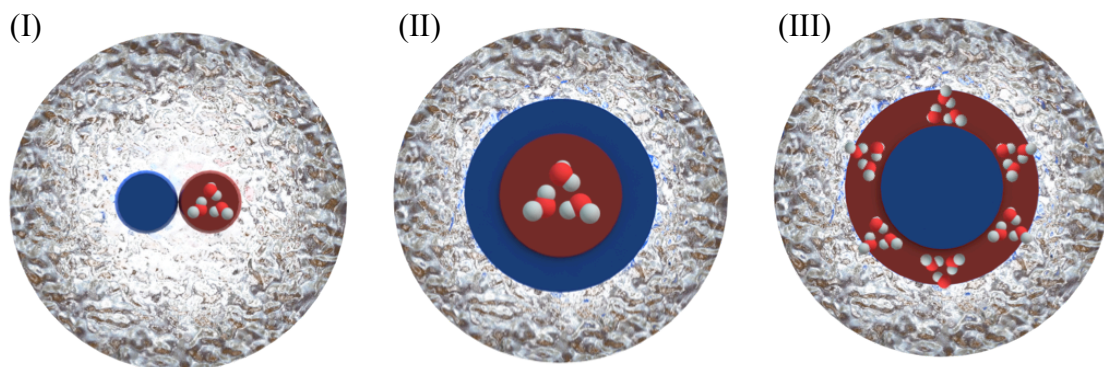
Figure 4.6. Simplified 'cartoon' showing the possible structures formed following the co-addition of water with a co-dopant. (I) shows water and co-dopant clusters attached as an aggregate, formed by the homogenous distribution of water and the co-dopant following sequential pickup, (II) a core-shell structure where water is picked up prior to the co-dopant and (III) a core-shell structure where the pickup order is reversed.

Figure 4.7 shows a comparison of mass spectra recorded in the region of the $(H_2O)_3^+$ ion signal when water was picked up prior to O_2 (upper plot, Figure 4.7) and when the pickup order was reversed (lower plot, Figure 4.7). The $(H_2O)_3^+$ ion was chosen for the comparison as it does not overlap with underlying signals from He_n^+ cluster ions, which would otherwise complicate the comparison. If a core-shell structure was formed, O_2

should either reduce or increase the fragmentation of water clusters to form $(H_2O)_nH^+$, depending on whether O_2 molecules surrounded the water clusters or vice-versa respectively. As such, the $(H_2O)_n^+/(H_2O)_nH^+$ signal ratio was chosen to compare the effect of switching the pickup order. To conveniently compare the $(H_2O)_n^+/(H_2O)_nH^+$ signal ratio the mass spectra were normalized so that the $(H_2O)_3H^+$ ions were of the same intensity.
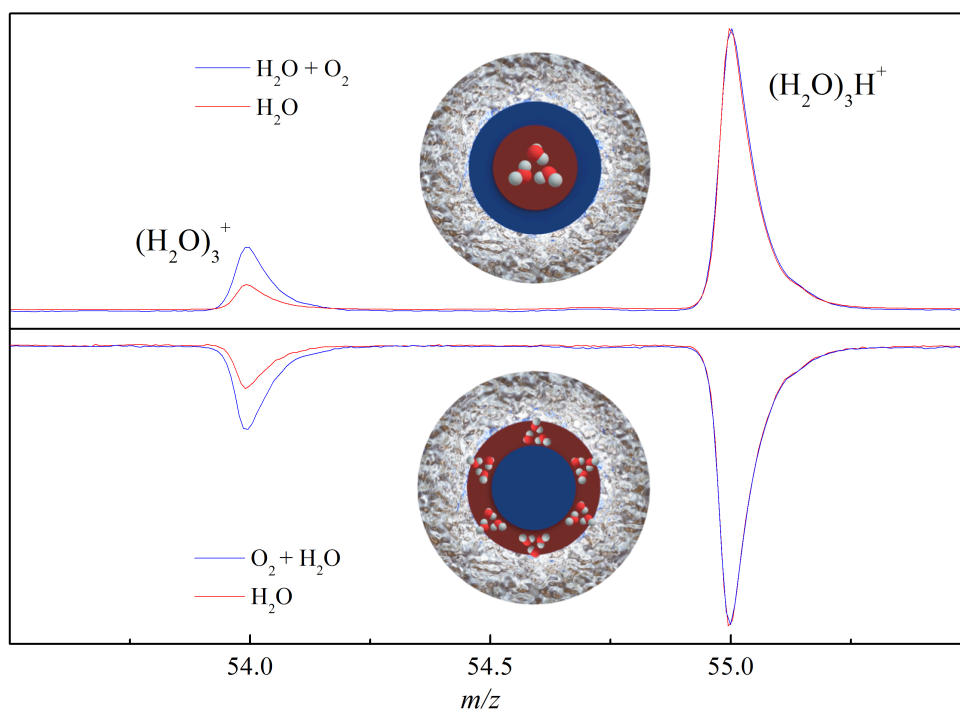
Figure 4.7. Electron impact mass spectra in the region of the $(H_2O)_3^+$ ion signal, showing a comparison of the yield of $(H_2O)_3^+$ relative to $(H_2O)_3H^+$. The blue line in the upper plot represents the addition of H_2O in the first pickup cell and O_2 in the second. The blue line in the lower figure represents the reverse pickup order of H_2O and O_2. The red line represents the pickup of pure water clusters.

The mass spectra show an increase in the $(H_2O)_3^+$ signal relative to that of $(H_2O)_3H^+$ following the addition of O_2 for both pickup orders. However, the pickup order does seem to affect the signal ratio. When water was added into the first pickup cell an enhancement factor of 2.49 was observed, whereas when water was added in the second

pickup cell a lower enhancement factor of 1.92 was observed. The clear difference in the enhancement factors indicates that distinct structures are formed which depend on the order in which the dopants are added. If the pickup of H_2O and O_2 did not lead to a core-shell structure, then no significant difference in the ion signals would be expected. However, as the pickup order alters the enhancement factor it implies that specific structures are being formed and provides evidence for the formation of core-shell particles, consisting of either a water or co-dopant core depending on the pickup order. A possible explanation for the larger enhancement factor, when water is the core species, is that it will become more likely that the co-dopant will be ionized prior to the water clusters, which will reduce the amount of energy available to fragment the water clusters. Consequently, ion signals corresponding to unprotonated water clusters will increase.

4.4.4. Core-shell structure – Investigation

In a previous study carried out by Lewis *et al.*[11] the fragmentation of triphenylmethanol (TPM) in helium droplets was investigated using electron impact ionization. In that particular study the effect of co-doping TPM with neon atoms on the fragmentation process was also explored, which has similarities to the work reported here. Lewis *et al*. reported that, as the average number of neon atoms picked up by the droplets increased, the fractional abundance of the TPM parent ion signal began to level out and reach an asymptotic limit after the addition of approximately 20 neon atoms. The observation of an asymptotic limit was reported to indicate the formation of a TPM molecule with a complete outer shell of neon atoms, and that the addition of further neon atoms had a reduced quenching effect on the ion fragmentation process. Lewis *et al*. suggested that this was presumably due to the formation of a second solvation shell

where the Ne atoms bind more weakly, with the result that evaporative loss of neon atoms from this second shell would remove less energy from the TPM core-shell cluster when compared to a single solvation shell structure.

The result of a similar experiment to calculate the number of O_2 molecules required to complete an outer shell around a water core is shown in Figure 4.8. This shows the variation of the $(H_2O)_3^+$ and $(H_2O)_9^+$ ion signals as the partial pressure of O_2 was increased. The $(H_2O)_3^+$ and $(H_2O)_9^+$ ion signals were chosen for this comparison as they do not overlap with He_n^+ cluster ions, and are taken to represent small and large water clusters, respectively. At low partial pressures the $(H_2O)_3^+$ ion intensity increases almost linearly with O_2 partial pressure, whilst for $(H_2O)_9^+$ there is only a slight variation in ion intensity. As the pressure of O_2 is raised an asymptotic limit is reached for both $(H_2O)_3^+$ and $(H_2O)_9^+$ at a O_2/H_2O ratio of 15 and 20, respectively.
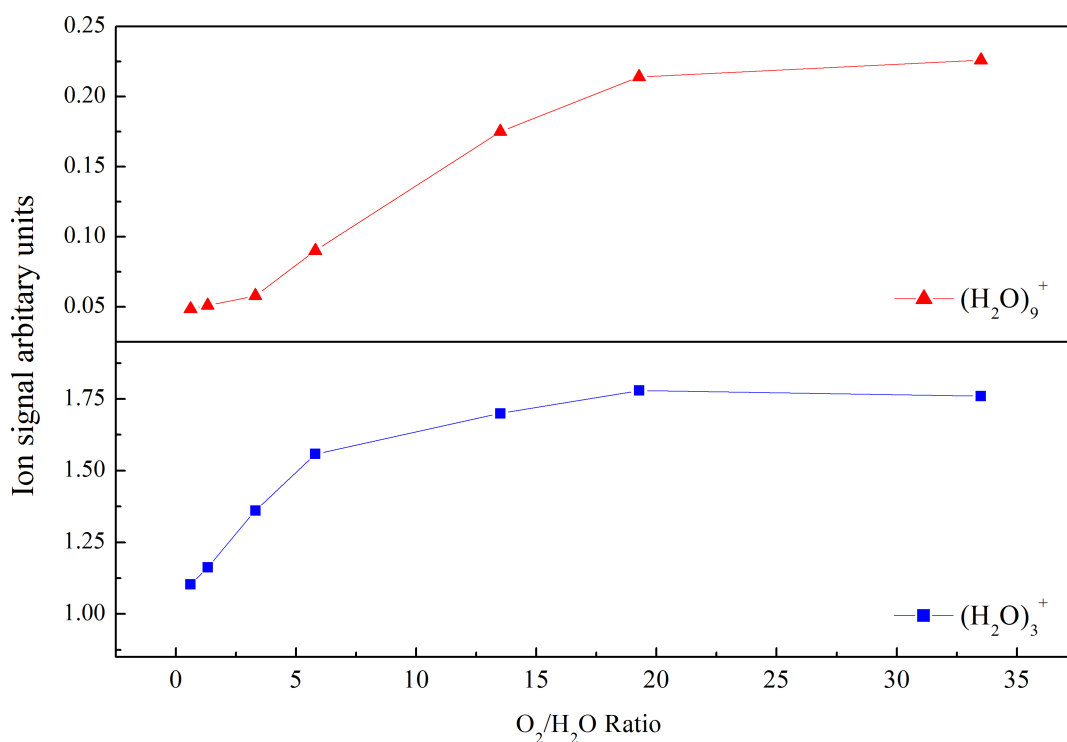
Figure 4.8. The dependence of unprotonated water cluster ion intensities on the partial pressure of O_2 relative to that of H_2O.

The difference in the response of the ion signals at low O_2 partial pressures is presumably due to the fact that smaller water clusters will require fewer O_2 molecules to provide a shielding effect against the ionization process. The observation of an asymptotic limit indicates the formation of a complete outer shell of oxygen atoms around the water clusters. Based on the value of the O_2/H_2O ratio when the asymptotic limit is reached, it is estimated that it will take around 45 O_2 molecules to complete an outer shell around $(H_2O)_3^+$ and approximately 60 O_2 molecules for $(H_2O)_9^+$. The difference in the number of O_2 molecules required to complete the outer shell for $(H_2O)_3^+$ and $(H_2O)_9^+$ implies that less O_2 is required to complete an outer shell around smaller clusters, whilst larger clusters will require more. Of course this assumes that $(H_2O)_3^+$ is representative of $(H_2O)_3$, whereas more likely it contains contributions form larger neutral complexes which fragment.

4.4.5. Core-shell clusters consisting of water and a co-dopant

Figure 4.9 shows a comparison of mass spectra recorded in the region of the $(H_2O)_3^+$ ion and shows the impact of an outer shell of O_2, CO and Ar on the $(H_2O)_3^+/(H_2O)_3H^+$ signal ratios. In all experiments the co-dopants were added to the second pickup cell to ensure that a core-shell structure consisting of a water core and co-dopant shell was formed. The co-dopant/H_2O ratio was made deliberately high (> 30) so that the co-dopant would form a complete outer shell around the water clusters. The mass spectra were normalized in a similar way to that used to present the core-shell effect in Figure 4.7, so that the effect of an outer shell of a co-dopant on the $(H_2O)_3^+/(H_2O)_3H^+$ signal ratio is easily observed.

The results show that an outer shell of O_2 causes an increase in the amount of $(H_2O)_3^+$ when compared to $(H_2O)_3H^+$. However, an outer shell of CO has the opposite

effect and a slight decrease in the amount of $(H_2O)_3$ when compared to $(H_2O)_3H^+$ is observed. In the case of argon no significant difference in the $(H_2O)_3{}^+/(H_2O)_3H^+$ signal ratio is observed.
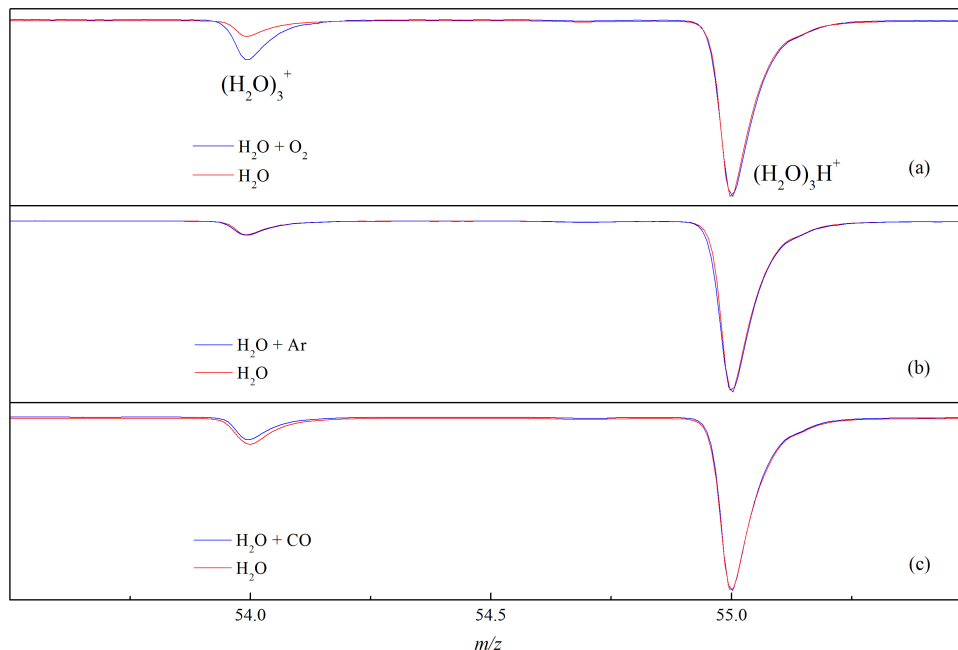
Figure 4.9. Comparison of mass spectra recorded in the region of the $(H_2O)_3{}^+$ ion showing the effect of the addition of (a) O_2, (b) Ar and (c) CO. In all cases the mass spectrum from pure water clusters is also shown and the water plus co-dopant spectrum is normalized such that the $(H_2O)_3H^+$ peak has the same intensity as the $(H_2O)_3H^+$ peak in the pure water spectrum.

4.4.6. Effect of core-shell structures with water cluster size

Figure 4.10 shows the variation of the ratio of the total water cluster ion signals (R_T) with water cluster size (n) for the CO/H_2O and O_2/H_2O systems. The term R_T was introduced to conveniently show the effect of a co-dopant on a range of water cluster sizes. R_T is defined in equation 4.3 and is essentially a comparison of the total ion signals containing n water molecules, in mass spectra recorded with and without a co-dopant. In the pure water spectrum the total water cluster ion signal, for a particular number of water molecules, n, was calculated by adding together the integrated area of

the $(H_2O)_n^+$ and $(H_2O)_{n-1}H^+$ ion signals. As the addition of a co-dopant leads to the formation of binary cluster ions, $X-(H_2O)_n^+$ and $X-(H_2O)_{n-1}H^+$, both the pure water cluster ions and the binary cluster ions in the co-doped spectrum were used to calculate the total water cluster ion signal.

$$R_T = \frac{[(H_2O)_n^+ + (H_2O)_{n-1}H^+ + X-(H_2O)_n^+ + X-(H_2O)_{n-1}H^+]_{X-(H_2O)}}{[(H_2O)_n^+ + (H_2O)_{n-1}H^+]_{H_2O}} \qquad (4.3)$$
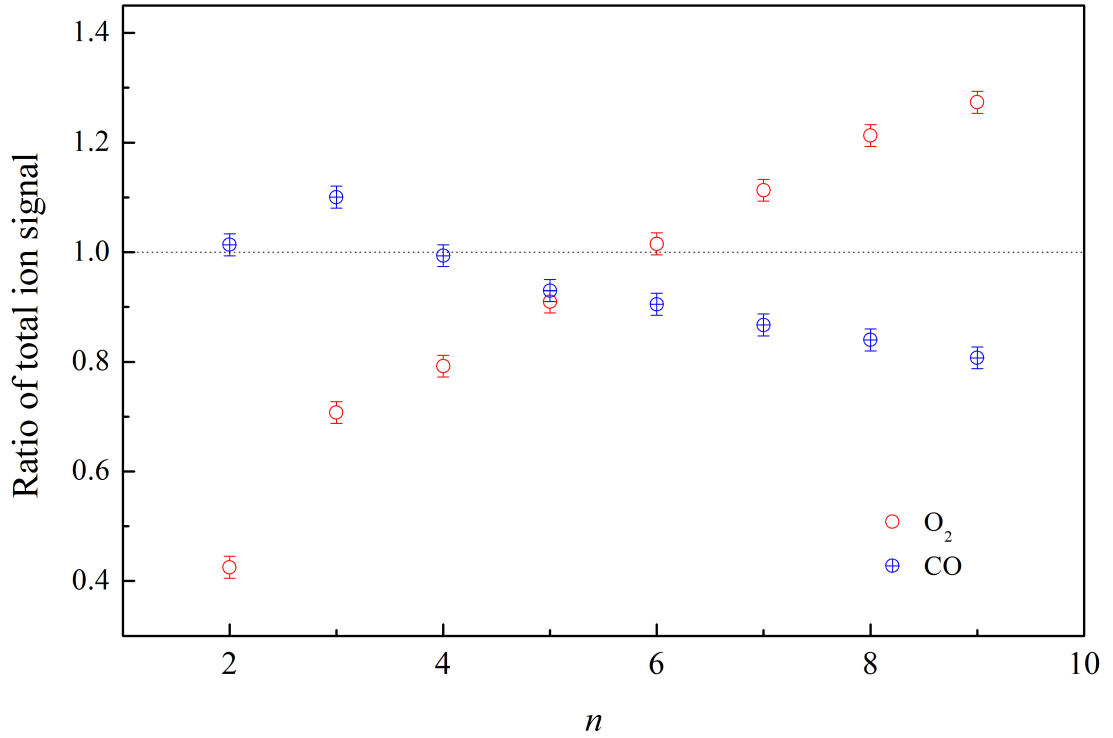
Figure 4.10. Ratio of the total water cluster ion signals between co-doped and un-doped water clusters. The co-dopants used were O_2 and CO. For co-doped water clusters the total water cluster ion signal includes $(H_2O)_n^+$, $(H_2O)_{n-1}H^+$, $X-(H_2O)_n^+$ and $X-(H_2O)_{n-1}H^+$. For un-doped water clusters the total water cluster ion signal includes $(H_2O)_n^+$ and $(H_2O)_{n-1}H^+$. The error margins are estimated based on the signal-to-noise ratios for various ion signals.

The addition of O_2 is shown to cause an increase in R_T with water cluster size, whilst for CO the opposite is observed. The increase in R_T for larger water cluster sizes,

when O_2 is added, might indicate that the presence of O_2 is preventing the fragmentation of larger water cluster sizes, which explains why the value of R_T decreases for smaller cluster sizes. For CO the opposite is observed and the value of R_T increases for smaller water clusters and decreases for larger clusters, which suggests that the presence of CO is increasing the fragmentation of water clusters. This is presumably due to the ionization energies of CO and O_2, which are above and below water respectively (see Table 4.3 below). Consequently, if CO is ionized prior to the water then additional energy will be available to fragment the water clusters (see section 4.6.2 below).

4.4.7. Softening effect of a co-dopant on the ionization of water clusters

Figure 4.11 shows the variation of R_n with water cluster size, using the O_2/H_2O, CO/H_2O and NO/H_2O systems as examples. R_n is defined in equation 4.4 and was introduced to conveniently compare how well a particular co-dopant softens the ionization of water clusters by charge transfer. The softening effect is measured by comparing the branching ratios between the $(H_2O)_n^+$ and the corresponding $(H_2O)_{n-1}H^+$ signals in the presence and absence of a co-dopant. When the ratio is equal to 1 it implies that the co-dopant has no effect on water cluster ion formation. On the other hand, if $R_n > 1$ it implies that the presence of the co-dopant impedes the fragmentation of the water cluster ions, whereas $R_n < 1$ implies that the co-dopant will increase the fragmentation of water cluster ions.

$$R_n = \frac{[(H_2O)_n^+ / (H_2O)_{n-1}H^+]_{X-(H_2O)}}{[(H_2O)_n^+ / (H_2O)_{n-1}H^+]_{H_2O}} \qquad (4.4)$$

It should be noted that even though the partial pressure of the co-dopants were made deliberately high, to ensure that the co-dopant would form either a partial or complete outer shell around the water clusters, the results obtained for the R_n values do not represent a quantitative comparison for the same amount of a particular co-dopant. This is because the presence of some co-dopants caused the water cluster ions to become too weak when large co-dopant/H_2O ratios were used, which made a comparison of the $(H_2O)_n^+/(H_2O)_nH^+$ ratio difficult.
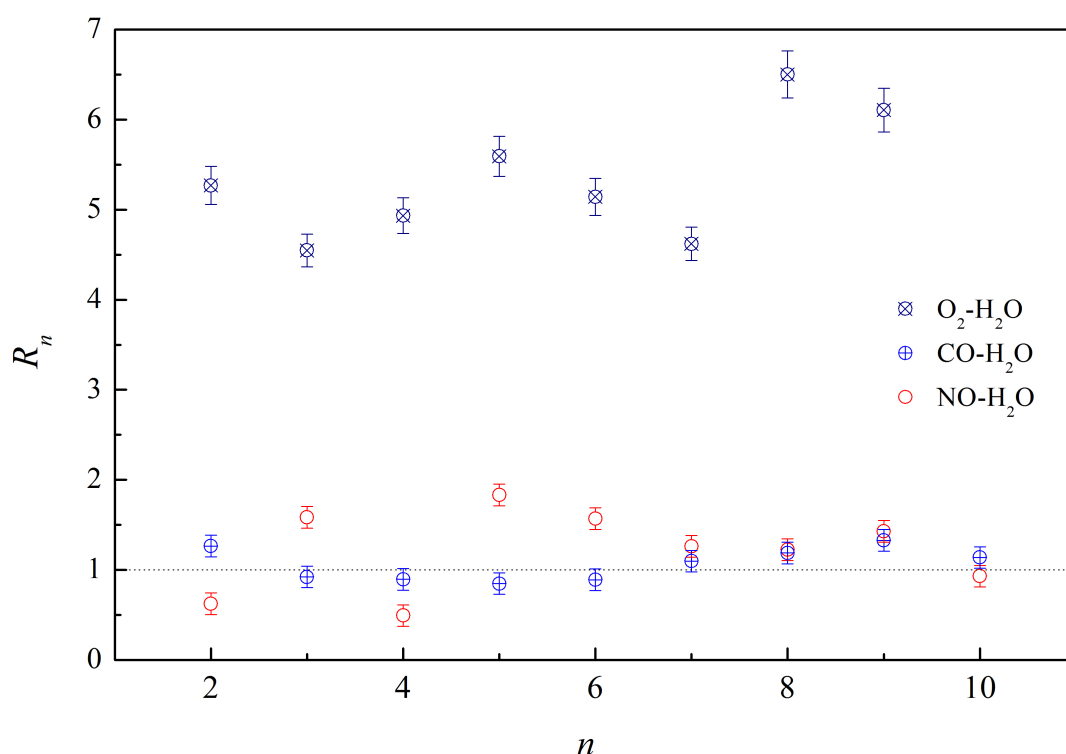
Figure 4.11. Variation of R_n with water cluster size (n) for the O_2/H_2O, CO/H_2O and NO/H_2O systems. For NO the variation of R_n when $n > 4$ is complicated due to the overlap of the binary cluster ions $((NO)_3(H_2O)_n^+)$ with water cluster ions $(H_2O)_{n+5}^+$ ($n = 0$, 1, 2 etc). The error margins were estimated based on the signal-to-noise ratios of the ion signals.

The addition of O_2 was found to significantly increase the production of $(H_2O)_n^+$ when compared to $(H_2O)_nH$, which is illustrated by an R_n value between 5 and 6 for all water cluster sizes. However for CO and NO the R_n value is generally between 0.5-2 and for

some cluster sizes the R_n value goes below 1, which indicates that the presence of CO and NO increases the fragmentation of the water cluster ions. When C_6D_6, N_2 and CO_2 were used a similar effect as for O_2 was observed and R_n values of 9.44, 1.6, and 3.5 were obtained, respectively. For argon an R_n value of 1 was determined, which implies no significant softening of the water clusters.

4.4.8. Normalized Softening effect of a co-dopant

In order to compare how the same amount of each co-dopant would affect the relative abundances of the water cluster ions, assuming a linear dependence of R_n with the number of co-dopant molecules, the R_n values were divided by the corrected parent ion signal of the co-dopant in the background mass spectrum.

$$S_n = \frac{R_n - 1}{I\sigma P} \qquad (4.5)$$

In the above equation I is the intensity of the parent ion signal of the co-dopant in the background mass spectrum, σ is the ionization cross section of the co-dopant at 100 eV, P is the percentage of the parent ion signal in the mass spectrum and R_n-1 describes the overall softening effect of the co-dopants.

Since pure water cluster ions were used for calculating R_n, an R_n value of 1 would imply no softening effect. As such, the value of R_n-1 was used in the calculation of the normalized softening effect to show the net softening effect of each co-dopant. If a positive value of S_n was obtained it implies that the co-dopant will act to prevent the fragmentation of water cluster ions. Similarly, if a negative value of S_n was obtained it implies the co-dopant will encourage fragmentation of the water cluster ions: an S_n value of 0 implies no softening effect. The values for the normalized softening effects

for some of the species explored in this study are shown in Table 4.1, where the softening effect was calculated for the water trimer. The softening effect is shown to follow the order $C_6D_6 > CO_2 > O_2 > N_2 > Ar$. CO and NO were excluded from the comparison as they are complicated by secondary reactions, which can favor the fragmentation process (see section 4.6.4 below).

Table 4.1 Comparison of the softening effect on the ionization of water clusters by charge transfer for the Ar/H_2O, N_2/H_2O, O_2/H_2O, CO_2/H_2O and C_6D_6/H_2O systems.

	Softening effect ($n = 3$)
Ar	0
N_2	19.4
O_2	121.8
CO_2	252.6
C_6D_6	2546.8

4.5.   COMPUTATIONAL RESULTS

4.5.1. Geometries of $[X(H_2O)_2]^+$: X = Ar, N_2 CO_2

Figure 4.12 shows the optimized geometries for $HO{\cdots}HOH_2^+$ and $[Ar(H_2O)_2]^+$. For the $[Ar(H_2O)_2]^+$ three distinct structures were identified, with the Ar attaching to one of the three free O-H bonds. The optimised global minimum geometries of $[Ar(H_2O)_2]^+$ are in good agreement with those reported by Gardenier et al.[20] and any slight differences are presumably due to the larger basis set employed in this study. For N_2 and CO_2 similar geometries were found (see Appendix A). In all cases the *trans-*structure, where one of Ar, N_2 or CO_2 is attached to the free OH bond of H_3O^+ on the other side from the hydroxyl moiety, is found to be the global-minimum (see Table

4.2). For the *cis*-structure, where one of Ar, N_2 and CO_2 is attached to the free OH bond of H_3O^+ on the same side of the hydroxyl moiety, slightly higher energies than the *trans*-structure were found. The highest total energy was found for the structure where one of Ar, N_2 and CO_2 is attached to the hydrogen atom of the OH moiety. The difference in the binding energies for the *trans* and *cis* structures is marginal and varies between 12 cm^{-1} to 45 cm^{-1}.[22]

(a)

(b)

(c)

(d)
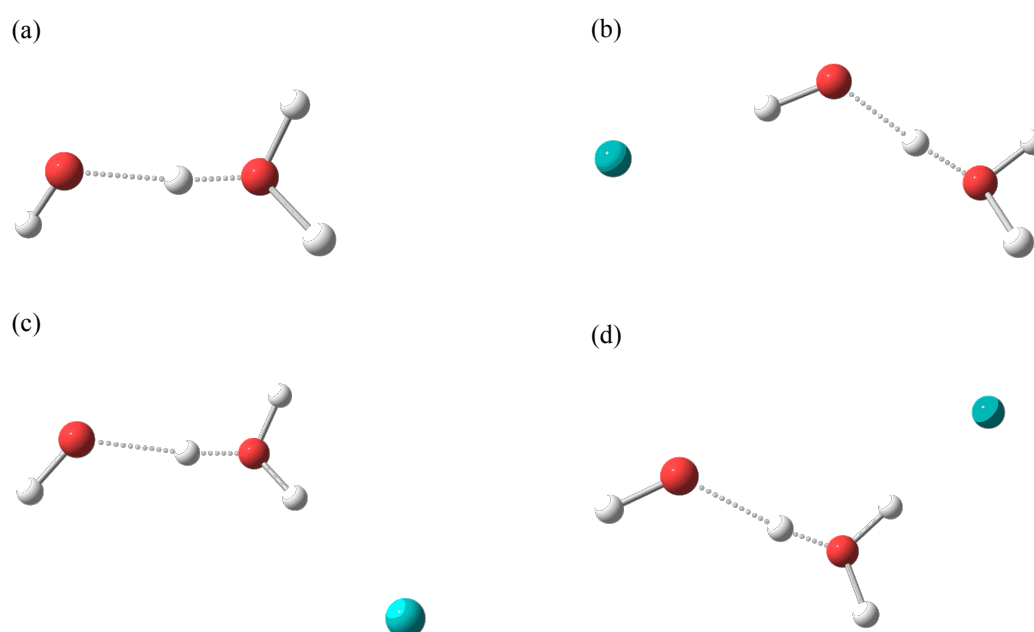
Figure 4.12. Optimised geometries for (a) HO$\cdots$HOH$_2^+$; (b) Ar$\cdots$(H$_2$O$_2$)$^+$; (c) cis-(H$_2$O$_2$)$^+$Ar; and (d) trans-(H$_2$O$_2$)$^+$Ar. The *trans*-geometry of [Ar(H$_2$O)$_2$]$^+$, shown in (d), is the global minimum. The optimised geometries of [N$_2$(H$_2$O)$_2$]$^+$ and [CO$_2$(H$_2$O)$_2$]$^+$ are similar to those shown here, in that an N$_2$ or CO$_2$ molecule is attached to one of the three H atoms in the dangling OH bonds (see Appendix A for structural properties of all the complexes).

Table 4.2 The structure, total energy and binding energies of $[X(H_2O)_2]^+$ ions (X= Ar, N_2 CO_2 and CO). The energies are expressed in cm^{-1}. The letters in square brackets correspond to the labels given for the structures shown in Figures 4.12 and 4.13.

X	Geometries	E_{total}	$\Delta E_{HO\cdots HOH_2^+}$	$\Delta E_{(H_2O)_2^+\cdots X}$
Ar	$HO\cdots HOH_2^+\cdots Ar$ (*trans*) [d]	0	7811.1	1254.8
	$HO\cdots HOH_2^+\cdots Ar$ (*cis*) [c]	11.7	7815.7	1239.4
	$Ar\cdots HO\cdots HOH_2^+$ [b]	501.6	10103.2	790.1
N_2	$HO\cdots H_3O^+\cdots N_2$ (*trans*)	0	7273.5	2935.4
	$HO\cdots H_3O^+\cdots N_2$ (*cis*)	40.7	7252.3	2890.3
	$N_2\cdots HO\cdots HOH_2^+$	872.1	11734.3	2062.9
CO_2	$HO\cdots HOH_2^+\cdots CO_2$ (*trans*)	0	6928.5	4190.6
	$HO\cdots HOH_2^+\cdots CO_2$ (*cis*)	25.2	6925.5	4166.4
	$CO_2\cdots HO\cdots HOH_2^+$	1063.6	13736.4	3216.2
CO	$HOCO\cdots H_3O^+$ (*trans*) [g]	0	7414.2	10498.1
	$HOCO\cdots H_3O^+$ (*cis*) [h]	841.9	7848.8	9036.9
	$HO\cdots HOH_2^+\cdots CO$ (*trans*) [a]	6465.6	6740.7	4734.8
	$HO\cdots HOH_2^+\cdots CO$ (*cis*) [c]	6529.5	6706.0	4658.7
	$HO\cdots HOH_2^+\cdots OC$ (*trans*) [b]	8842.8	7532.3	1966.3
	$HO\cdots HOH_2^+\cdots OC$ (*cis*) [d]	8872.4	7515.2	1940.3
	$OC\cdots HO\cdots HOH_2^+$ [e]	7670.4	14232.8	3533.0
	$CO\cdots HO\cdots HOH_2^+$ [f]	9533.9	10881.6	1306.9

4.5.2. Geometries of [CO(H$_2$O)$_2$]$^+$

Figure 4.13 shows the optimized geometries for [CO(H$_2$O)$_2$]$^+$, in total eight stable structures were identified.

(a)

(b)

(c)

(d)

(e)

(f)

(g)

(h)
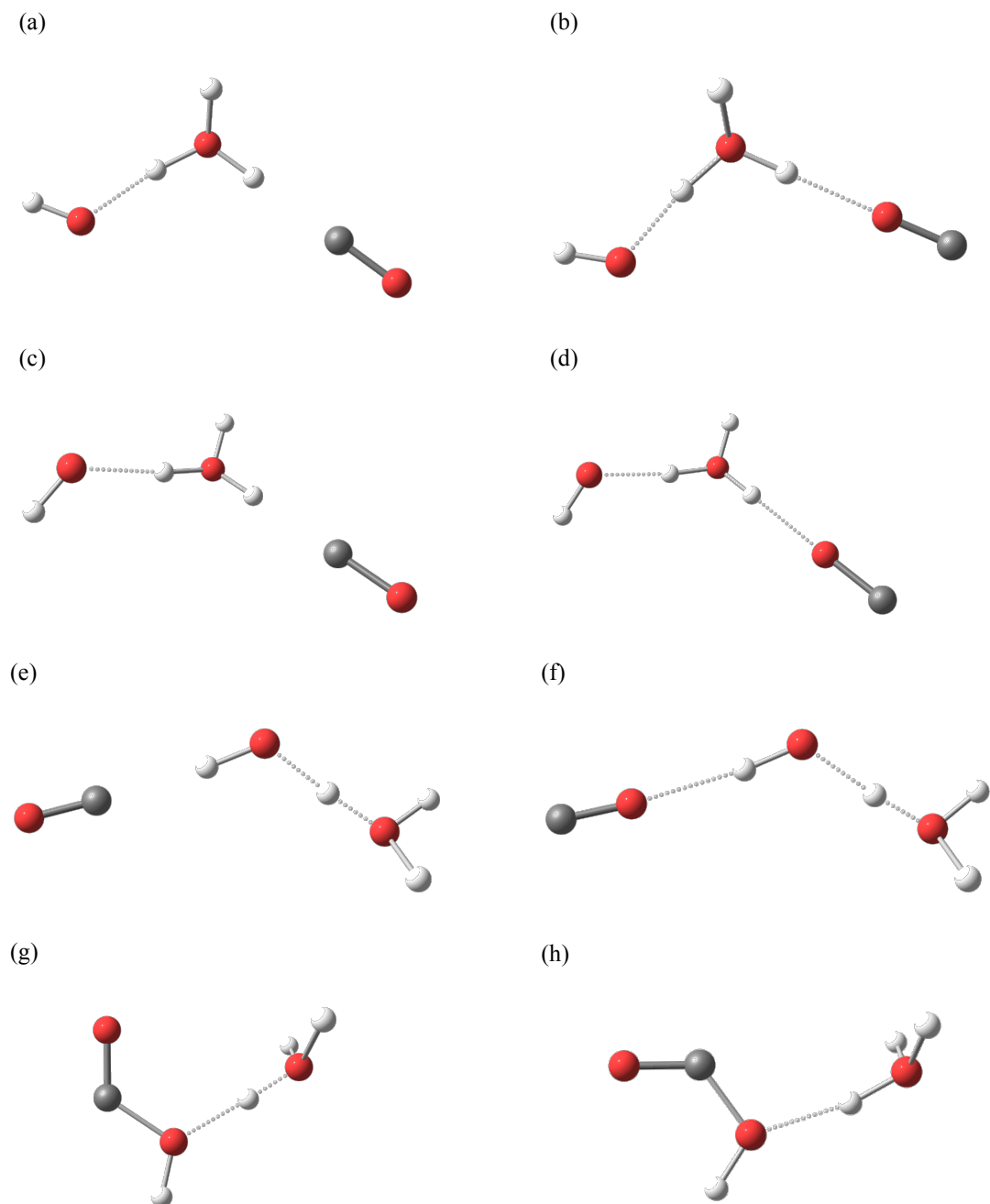
Figure 4.13. Calculated structures of [CO(H$_2$O)$_2$]$^+$. (a) *trans*-(H$_2$O)$_2$$^+$CO; (b) *trans*-(H$_2$O)$_2$$^+$OC; (c) *cis*-(H$_2$O)$_2$$^+$CO; (d) *cis*-(H$_2$O)$_2$$^+$OC; (e) OC⋯(H$_2O_2$)$^+$; (f) CO⋯(H$_2O_2$)$^+$; (g) *trans*-HOCO⋯H$_3O^+$; (h) *cis*-HOCO⋯H$_3O^+$.

99

The CO molecule can bind to any of the three free O-H bonds with either the carbon or oxygen atom. However, for CO the lowest energy configuration is when the carbon atom is attached to the oxygen in the hydroxyl moiety, rather than being attached to one of the three hydronium ions. Attachment of CO to the hydroxyl in the *trans*-HOCO$\cdots$H$_3$O$^+$ structure produces a strong HO-CO bond with a binding energy of 10498 cm^{-1}, which is slightly higher than the binding energy of neutral HOCO (9723 cm^{-1}).[25] For the same structure, the binding energy between the HO$\cdots$HOH$_2^+$ is calculated to be 7414 cm^{-1}. The *cis*-HOCO$\cdots$H$_3$O$^+$ structure is slightly higher in energy than the *trans*-structure by 842 cm^{-1}, and the binding energy between CO and the hydroxyl moiety also exceeds that of the HO$\cdots$HOH$_2^+$ bond. The third most stable structure is the *trans* HO$\cdots$HOH$_2^+$$\cdots$CO ion, which has a much higher total energy of $+$ 0.81 eV relative to the global minimum.[22]

4.6.   DISCUSSION

The main experimental findings from this work are that core-shell structures will form following the co-addition of water and a co-dopant into a helium droplet and that a core-shell structure consisting of an outer shell of a co-dopant molecule can alter the abundance of the $(H_2O)_n^+$ when compared to the $(H_2O)_n H^+$. In the experiments where C$_6$D$_6$, CO$_2$, O$_2$ and N$_2$ were used the results have shown that the abundance of the $(H_2O)_n^+$ will increase when compared to the $(H_2O)_n H^+$, whilst for CO and NO the opposite is observed. Argon was the only co-dopant to have no significant effect on the abundances of the water cluster ions.

In order for the amount of $(H_2O)_n^+$ to increase, the co-dopant must be able to stabilize the $(H_2O)_n^+$ following the ionization of water clusters by charge transfer. There are two ways that this can happen: (1) excess energy is rapidly carried away by the

evaporative loss of co-dopant molecules from the surface of the $(H_2O)_n^+$; (2) the co-dopant acts as a buffer and reduces the excess energy delivered into the system by charge transfer from the He^+. Consequently, the findings of the work shown here might be explained by an 'energy in' and 'energy out' mechanism (see section 4.6.3 below).[26]

4.6.1. Heat dissipation by evaporative loss of co-dopant molecules

Following the ionization of water clusters within a helium droplet, the excess energy deposited into the vibrational degrees of freedom of the $(H_2O)_n^+$ clusters can be quenched by the rapid evaporation of helium atoms from the droplet, which at a minimum will remove the binding energy (5 cm^{-1}) holding a helium atom to the droplet.[24] However, in addition to the evaporation of helium atoms the $(H_2O)_n^+$ cluster ions can also be cooled by the evaporation of co-dopant molecules.[11] The minimum amount of energy that can be dissipated by the evaporative loss of co-dopant molecules is the binding energy between the co-dopant and the charged water cluster cation. Unfortunately, this is difficult to estimate, as the binding energy will vary with the number of co-dopant molecules used, the water cluster size and the geometry of the charged cation. However, as the primary interaction between a positive charge and a non-polar neutral species will be the charged-induced dipole interaction, the dipole polarizability of the co-dopant can be used to estimate the strength of the interaction between the two species. The dipole polarizabilities of the co-dopants used in this study are shown in Table 4.3.

Table 4.3 Comparison of the ionization energies and the dipole polarizability for the co-dopants used in this work (au refers to atomic units).

	IE/eV[17]	Dipole polarizability/ au
Ar	15.76	10.75 [a]
N_2	15.58	11.57 [b]
O_2	12.07	10.66 [c]
CO_2	13.78	13.8 [d]
C_6D_6	9.25	67.48 [e]
H_2O	12.65	9.64 [f]
CO	14.01	13.08 [f]
NO	9.27	9.844 [g]

[a] Ref. 27 [b] Ref. 28 [c] Ref. 29 [d] Ref. 30 [e] Ref. 31 [f] Ref. 32 [g] Ref. 33

4.6.2. Effect of a core-shell structure on the charge transfer reactions

If a core-shell structure is formed with a water core and a co-dopant outer shell then the primary reactant with the He^{+} is expected be the co-dopant.[11] This will release an amount of energy determined by the difference in ionization energies of He and the outer shell material (E_i). If water has a lower ionization energy (IE_{H_2O}) than the outer shell material (IE_X), then it is likely that the charge will further hop from the shell species onto the water, generating further excess energy to fragment the water clusters. Consequently, the total energy that will need to be dissipated in order to stabilize the H_2O^+ can be expressed as $IE_X - IE_{H_2O} + E_i$. The ionization energies of the co-dopants used are shown in Table 4.3.

4.6.3. Softening effect of a co-dopant: The 'energy in' / 'energy out' mechanism

Of all of the co-dopants used in this study, argon was the only one that exhibited no significant effect on the relative abundances of the water cluster ions. The reason for this can be explained in terms of an 'energy in' and 'energy out' mechanism. From the previous discussion, it is expected that the initial reaction will be between argon and the He^+. As such, the amount of energy that will be deposited into the water clusters will be the difference between the ionization energies of argon and water, which is 3.11 eV. Of course this assumes that the initial high burst of energy, when charge is transferred from He^+ to Ar, has been successfully dissipated. In order for argon to stabilise the water molecules it must be able to dissipate this excess energy by the evaporative loss of argon atoms. However, as there was no significant difference between the relative abundances of the water cluster ions, in mass spectra recorded with and without the presence of argon, it implies that the amount of energy that is carried away by the evaporative loss of argon atoms is not sufficient to offer any stabilization of $(H_2O)_n^+$ above and beyond that provided by the evaporative loss of helium atoms alone.

In the case of N_2 and O_2, these species were found to exhibit a significant softening effect. From Table 4.2 it can be seen that the dipole polarizability of N_2 is larger than O_2, and therefore it is reasonable to expect that N_2 will have a larger binding energy to the water cluster cations than O_2. Consequently, the evaporation of N_2 from the surface of the water clusters should remove more energy than O_2. However, in practice it is observed that O_2 provides a stronger softening effect than N_2. Consequently, the amount of excess energy that remains in the water cluster cation following the evaporation of all of the co-dopant molecules must be the deciding factor. This is illustrated by the difference in the ionization energies of N_2 and O_2 relative to

water, 2.93 eV and 0.58 eV respectively, which implies that more energy will be deposited into the N_2/H_2O system when compared to the O_2/H_2O system.

The largest softening effect was observed for the CO_2/H_2O and the C_6D_6/H_2O systems. For these systems, as they have more vibrational degrees of freedom, they are able to carry away more excess energy in the form of vibrational excitation, with C_6D_6 having the potential to remove far more energy than CO_2 by this means. The ionization energy of C_6D_6 is much lower than water, meaning that far less energy can be deposited into the water clusters when C_6D_6 is the shell material. On the other hand, the ionization energy of CO_2 is larger than O_2, which should cause more energy to be deposited into the water clusters. However the dipole polarizability of CO_2 is much larger than O_2 and will be able to dissipate more energy by the evaporative loss of either co-dopant from the surface of the water clusters. C_6D_6 has the largest dipole polarizability of all of the other co-dopants used in this work and will therefore be able to dissipate much more energy by evaporation.

4.6.4. The effect of NO and CO following the ionization of water clusters

The co-addition of NO and CO with water has a very different response on the relative abundances of the water cluster ions. For example, in Figure 4.11 it is shown that the presence of CO and NO can increase the fragmentation of the $(H_2O)_n^+$ for some water cluster sizes (e.g. $n = 4$). The ionization energies of NO and CO are 14.01[17] and 9.27[17] eV, respectively. If the effect of CO and NO on the abundance of the $H_2O_n^+$ were to be explained in terms of the 'energy in' and 'energy out' mechanism proposed earlier, CO should have a reduced softening effect when compared to NO and a strong effect would be observed. However, in practice there is little difference between the two species. A contributing factor to the difference between CO and NO to the other species

used in this study is that they can both act as acceptors for OH radicals and form HOCO and HONO. In a recent study using infrared spectroscopy to investigate the structures of water cluster radical cations, Mizuse *et al*. observed an extra band, which they attributed to the stretching vibration of an OH radical in $(H_2O)_n^+$.[34] Mizuse *et al*. also suggested that the nominal structure of the $(H_2O)_n^+$ should be regarded as $H^+(H_2O)_{n-1}(OH)$ and will have a dangling OH bond at the surface of the water clusters.[34] If similar structures are formed in helium droplets then NO and CO may be able to react with the free OH radical and form stable complexes of HONO and HOCO.

The formation of HONO has been observed experimentally in a gas phase dissociation experiment of $NO^+(H_2O)_n$, in which NO was picked up by a cluster beam consisting of a water/argon mixture.[35] In this experiment the results showed that the reaction $NO^+(D_2O)_n + D_2O \rightarrow (D_2O)_nD^+ + DONO$ became the dominant reaction pathway for $n = 4$ and beyond.[35] From the findings of these experiments the reduction in the abundance of water cluster ions, in the experiments for CO and NO, might be explained by secondary ion molecule reactions to form HONO and HOCO, as shown below.

$$NO^+(H_2O)_n + H_2O \rightarrow (H_2O)_nH^+ + HONO \qquad (4.6)$$

$$CO^+(H_2O)_n + H_2O \rightarrow (H_2O)_nH^+ + HOCO \qquad (4.7)$$
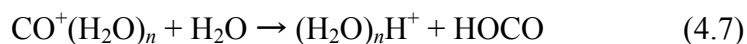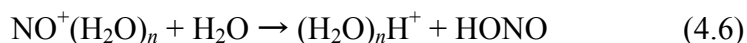
4.6.5. $(H_2O)_2/X$ clusters: ab initio interpretation

The results from the *ab initio* calculations performed on the $[X(H_2O)_2]^+$ for X = Ar, N_2, CO_2 and CO seem to support the above discussion. From Table 4.2 it is observed that for Ar, N_2 and CO_2 the binding energy between them and the $(H_2O)_2^+$ is always lower than the binding energy between the HO and HOH_2^+ moieties, regardless

of their structure. Consequently, it is likely that the lowest energy dissociation process would be the loss of X, a process which would cool the remaining $(H_2O)_2^+$ and increase the likelihood that the unprotonated water dimer cation will survive the ionization process. This should appear as an increase in the signal intensity of $(H_2O)_2^+$ relative to H_3O^+ in the mass spectra. A similar process is expected for the higher energy geometries of the $[CO(H_2O)_2]^+$, as the binding energies between CO and $(H_2O)_2^+$ are always lower than that between the HO and HOH_2^+ moieties. However, in practice an increase in the protonated water cluster ions is observed when CO is co-added with water clusters. In its lower energy forms the binding energy between the hydroxyl moiety and CO is much stronger than that between the HO and HOH_2^+ moieties. As a result, on purely energetic grounds, the lowest energy dissociation process would favour the cleavage of the $HO\cdots HOH_2^+$ bond, rather than the loss of CO. Consequently, the increase in the protonated water cluster ions suggests that CO will tend to form its lower energy forms, despite the fact that of there is a large excess energy available for the production of the higher energy structures following the initial charge transfer from He^+.[22]

4.7. CONCLUSION

In this chapter, electron impact ionization has been used to identify the formation of core-shell structures within helium nanodroplets. The use of a sequential pickup technique has demonstrated that core-shell structures can be tailored depending on the pickup order of the species used. The relative abundances of the water cluster cations, $(H_2O)_n^+$ and $(H_2O)_nH^+$, in the mass spectra recorded with and without a co-dopant have been used to indicate whether a co-dopant will have a softening effect on the ionization of water clusters by charge transfer. The ability of a co-dopant to soften the ionization

process has been explained in terms of an 'energy in' and 'energy out' mechanism. The key properties of the co-dopant that can contribute to the softening of the ionization process have been identified as the amount of energy that can be dissipated from the $(H_2O)_n^+$ by evaporative loss of the co-dopant molecules, the number of vibrational degrees of freedom of the co-dopant, and the amount of excess energy that remains in the vibrational degrees of freedom of the water clusters following the evaporative loss of all the co-dopant molecules. The difference in the response of the relative abundances of the water cluster cations when CO and NO were the co-dopant have been explained in terms of secondary ion-molecule reactions to form HONO and HOCO. This is possible as NO and CO can act as acceptors for the OH radical, which will be at the surface of the water cluster cations. This process has been suggested to explain the increase in the abundance of the protonated water cluster cations for some cluster sizes. The results form *ab initio* calculations support the interpretation of the experimental results. In the lowest energy structures of the $[CO(H_2O)_2]^+$ an HOCO moiety is formed with a HO-CO binding energy exceeding that of $HO\cdots HOH_2$. On purely energetic grounds, any bond fission would favor cleavage of the $HO\cdots HOH_2$ bond rather than the loss of CO. In the case of Ar, N_2 and CO_2, when these species are attached to water dimer cations, the binding energy between $HO\cdots HOH_2$ is always larger than the binding energy of $X\cdots(H_2O)_2^+$. Consequently, in these cases, the lowest energy dissociation process would be the loss of X, a process which would cool the remaining $(H_2O)_2^+$ and increase the likelihood that the unprotonated water dimer cation will survive the ionization process. It is expected that the results from these calculations will transfer to larger water cluster sizes and they quantitatively explain the differences in the relative abundances of the water cluster cations in helium droplet experiments when water is co-added with another species.

REFERENCES FOR CHAPTER 4

1. J. P. Toennies, A. F. Vilesov, *Annu. Rev. Phys. Chem.,* 1998, **49**, 1.

2. J. P. Toennies, A. F. Vilesov, *Angew. Chem. Inst. Ed*. 2004, **43**, 2622.

3. J. Higgins, W. E. Ernst, C. Callegari, J. Reho, K. K. Lehmann, G. Scoles, M. Gutowski, *Phys. Rev. Lett*., 1996, **77**, 4532.

4. J. Higgins, C. Callegari, J. Reho, F. Stienkemeier, W. E. Ernst, K. K. Lehmann, M. Gutowski, G. Scoles, *Science*, 1996, **273**, 629.

5. K. Nauta, R. E. Miller, *Science*, 1999, **283**, 1895.

6. K. Nauta, R. E. Miller, *Science*, 2000, **287**, 293.

7. A. M. Ellis, S. Yang, *Phys. Rev. A*., 2007, **76**, 032714.

8. B.E. Callicoatt, D. D. Mar, V. A. Apkarian, and K. C. Janda, *J. Chem. Phys.*, 1996, **105,** 7872.

9. M. Farnik, J. P. Toennies, *J. Chem. Phys*., 2005, **122**, 014307.

10. Y. Ren, V. V. Kresin, *J. Chem. Phys*., 2008, **128**, 074303.

11. W. K. Lewis, B. E. Applegate, J. Szta´ray, B. Szta´ray, T. Baer, R. J. Bemish, R. E. Miller, *J. Am. Chem. Soc*., 2004, **126**, 11283.

12. A. J. Stace, J. F. Winkel, R. B. Lopez Martens, J. E. Upham, *J. Phys. Chem*., 1994, **98**, 2012.

13. R. T. Jongma, Y. Huang, S. Shi, A. M. Wodtke, *J. Phys. Chem. A*, 1998, **102**, 8847.

14. S. Yang, S. Brereton, S. Nandhra, A. M. Ellis, B. Shang, L. Yuan, J. Yang, *J. Chem. Phys*., 2007, **127**, 134303.

15. S. Yang, S. M. Brereton, A. M. Ellis, *Rev. Sci. Instrum.*, 2005, **76**, 104102.

16. S. Yang, A. M. Ellis, *Rev. Sci. Instrum*., 2008, **79**, 016106.

17. NIST Chemistry WebBook, see http://webbook.nist.gov/chemistry/.

18. S. P. de Visser, L. J. de Koning, N. M. M. Nibbering, *J. Phys. Chem.*, 1995, **99**, 15444.

19. R. N. Barnett, U. Landman, *J. Phys. Chem. A* 1997, **101**, 164.

20. G. H. Gardenier, M. A. Johnson, A. B. McCoy, *J. Phys. Chem. A*, 2009, **113**, 4772.

21. C. J. Cramer, *Essentials of Computational Chemistry: Theories and Models*, 2nd Edition, Wiley, 2004.

22. B. Shepperson, J. Liu, A. M. Ellis, S.Yang, *J. Chem. Phys.*, 2012, **137**, 201102.

23. B.E. Callicoatt, D. D. Mar, V. A. Apkarian, K. C. Janda, *J. Chem. Phys.*, 1996, **105,** 7872.

24. J. P. Toennies, A. F. Vilesov, *Angew. Chem. Inst. Ed*. 2004, **43**, 2622.

25. B. Ruscic, M. Litorja, *Chem. Phys. Lett.*, 2000, **316**, 45.

26. J. Liu, B. Shepperson, A. M. Ellis, S. Yang, *Phys*. *Chem*. *Chem*. *Phys.*, 2011, **13**, 13920.

27. N. K. Rahman, A. Rizzo, D. L. Yeager, *Chem. Phys. Lett*., 1990, **166**, 565.

28. H. J. A. Jensen, P. Jørgensen, T. Helgaker, J. Olsen, *Chem. Phys. Lett*., 1989, **162**, 355.

29. A. C. Newell, R. C. Baird, *J. Appl. Phys.*, 1965, **36**, 3751.

30. A. Chrissanthopoulos, U. Hohm, U. Wachsmuth, *J. Mol. Struct*., 2000, **526**, 323.

31. S. P. Karna, G. B. Talapatra and P. N. Prassad, *J. Chem. Phys*.,1991, **95**, 5873.

32. A. Hu, D. M. York, T. K. Woo, *J. Mol. Struct.*, 2002, **591**, 255.

33. J. R. Hammond, W. A. de Jong, K. Kowalski, *J. Chem. Phys*., 2008, **128**, 224102.

34. K. Mizuse, J. Kuo and A. Fujii, *Chem. Sci*., 2011, **2**, 868.

35. A. J. Stace, J. F. Winkel, R. B. Lopez Martens, J. E. Upham, *J. Phys. Chem.*,

1994, **98**, 2012.

CHAPTER 5

HOT MOLECULES IN HELIUM NANODROPLETS: A NEW ROUTE TO

OPTICAL SPECTRA

This chapter presents details about a new technique to record optical spectra of dopant species within helium nanodroplets. The technique is applicable when optical excitation of a dopant species leads to the formation of a long-lived metastable state inside a helium droplet. If the dissipation of energy from this metastable state into the helium droplet is inefficient, then the optical spectrum can be recorded as a difference in the abundance of the ion fragments of the dopant species, as opposed to a difference in the ionization cross-section of the droplet. This technique was demonstrated by using the electronic excitation of toluene to its S_1 state as an example. Following excitation to the S_1 state toluene will undergo intersystem crossing to a long-lived T_1 state, with a high quantum yield. By monitoring the $C_5H_5^+$ and the $C_7H_7^+$ fragment ions optical spectra were obtained in an ion-enhancement and ion-depletion mode respectively.

5.1. INTRODUCTION

The use of helium droplets for the spectroscopic analysis of both individual molecules and molecular clusters has become increasingly popular over the past few decades.[1,2] This is largely due to the unique properties possessed by the droplets, which include an extremely low equilibrium temperature (0.37 K), high thermal conductivity and their ability to rapidly dissipate excess energy through the evaporative loss of weakly bound helium atoms. An added advantage of using helium droplets is that the surrounding liquid helium only weakly interacts with the dopant species, which makes assignments of spectral transitions much easier.

Optical spectra are typically recorded using a beam depletion technique, which relies on the efficiency of the non-radiative energy transfer from the optically excited dopant into the surrounding liquid helium. The energy transferred into the droplet is rapidly dissipated by the evaporative loss of helium atoms from the droplet surface, which causes a reduction in the size of the droplet. This reduction in droplet size can be monitored with the use of a quadrupole mass spectrometer, set to transmit the signal intensity of specific mass channels.[3] Alternatively, a bolometer can be used, which detects the reduction in droplet size as a decrease in the energy content of the droplet beam.[4,5]

Beam depletion spectroscopy is very effective for recording vibrational spectra within helium droplets. This is because vibrational excitations of molecules relax very efficiently in the droplets.[2] However, it is not always as effective for studying electronic transitions. Whilst vibrations in both the ground and excited electronic states relax very efficiently in the droplets, the electronic excitation itself may relax much more slowly.[6] In some cases the amount of energy that is transferred into the droplet can be significantly less than the photon energy absorbed, especially if the species under investigation has a large fluorescence quantum yield. In such cases, the reduction in droplet size will depend on the vibrational energy content of the molecule following fluorescence, which is often much less than the photon energy absorbed. Therefore, if molecules fluoresce from their electronic excited states, then laser-induced fluorescence (LIF) will be more efficient for recording optical spectra.[7] More recently resonance-enhanced multiphoton ionization (REMPI) spectroscopy has been applied to investigate electronically excited states of dopant species within helium droplets.[8]

For some species, non-radiative decay channels may compete very effectively with fluorescence. One possibility is the conversion of singlet excited states into triplet

states, which is commonly observed for aromatic molecules. For some aromatic species, intersystem crossing (ISC) is so efficient that it becomes the dominant decay process. If the difference in energy between the singlet and triplet state is relatively small, then only a small amount of energy will be available to be deposited into the droplet. Consequently, if the triplet state is long-lived on the timescale of the experiment, then beam depletion spectroscopy will not be able to record the electronic transition.

In this chapter, details of a new technique for recording optical spectra of a dopant species will be given. The technique, which we call the 'hot molecule' technique, is applicable when optical excitation of a dopant leads to the formation of a long-lived metastable state inside a helium droplet. If the dissipation of energy from this metastable state into the helium droplet is not very efficient, then the optical spectrum will be recorded as a difference in the abundance of the ion fragments of the dopant species, as opposed to a difference in the ionization cross-section of the droplet. The technique was demonstrated by using the electronic excitation of toluene to its S_1 state as an example. Toluene has been studied previously in helium droplets, when Boatwright *et al.* used beam depletion spectroscopy to investigate a range of substituted benzene molecules.[9] In the work presented here, it is shown that the hot molecule technique can also be used to record electronic spectra of toluene. This is possible because excitation of toluene to the S_1 state leads to efficient ISC into the T_1 state, which is sufficiently long-lived on the timescale of the experiment.

5.2.   EXPERIMENTAL

The experimental apparatus has been described in detail in Chapter 2, so only a brief description of the experimental setup will be given here. Helium droplets were

produced using a continuous source and were detected with the use of both a reflectron time-of-flight mass spectrometer (TOF-MS) and a quadrupole mass spectrometer (QMS). The TOF-MS was used to record mass spectra as it has a higher mass resolution than the QMS, whilst the QMS was used to monitor specific ion channels as a function of wavelength. The continuous source was operated with stagnation conditions of 11 K and 20 bars, which gave droplet sizes containing an average of $<N>$ = 11 000 helium atoms.[10]

As mentioned in the introduction, the most commonly used method to record an optical spectrum is by monitoring the reduction in the ionization cross-section of the helium droplet following relaxation of the photon energy absorbed by the dopant. As such, it is preferable to use smaller helium droplet sizes, $<N> = 5\ 000$, to give the best signal-to-noise ratio.[11,12] However, in this experiment, optical spectra were recorded by monitoring the relative abundances of specific ion fragments, following electron impact ionization of a toluene molecule in its T_1 state. As such, larger droplet sizes were deliberately employed so that contributions from conventional depletion spectroscopy would be minimised.

The amount of toluene added into the droplet was gauged by the ion signal of the $C_7H_8^+$ in the helium droplet mass spectrum. In order to minimise contributions from the toluene dimer and larger cluster fragments $((C_7H_8)_n^+)$, the amount of toluene added was carefully administered to ensure that the pickup of a single toluene molecule was by far the dominant process. A mass spectrum showing the pickup conditions is shown in Figure 5.1. The figure shows mass spectra recorded in the region of the toluene monomer and dimer and, in the inset, an expanded view showing the $C_5H_5^+$, $C_7H_7^+$ and $C_7H_8^+$ peaks. The primary peaks observed in the mass spectrum are the $C_7H_7^+$ and $C_7H_8^+$ (parent ion) peaks, which is similar to the electron impact mass spectrum of

toluene recorded in the gas phase.[13] The weak ion signal intensity of the $(C_7H_8)_2^+$ when compared to the $C_7H_8^+$ peak indicates that the pickup was successfully optimised for a single toluene molecule. It should be mentioned that the $C_7H_8^+$ might contain some contribution from the fragmentation of $(C_7H_8)_2^+$ and larger $(C_7H_8)_n^+$ clusters, although this effect is expected to be minimal given the low partial pressure of toluene employed in this study.
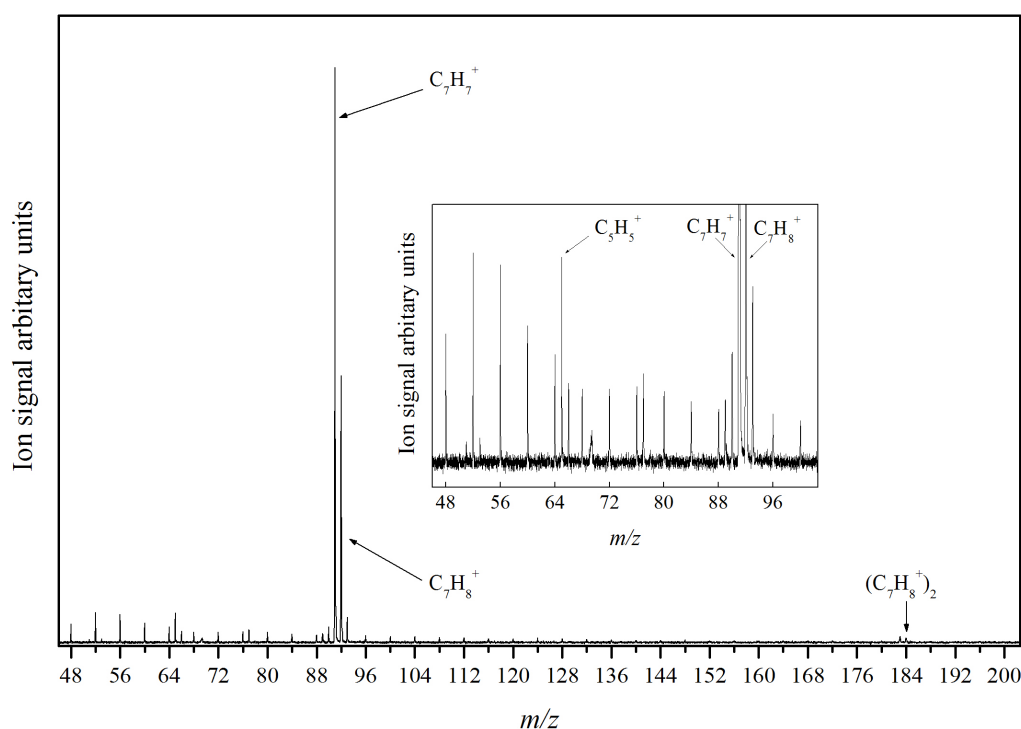
Figure 5.1. Mass spectra recorded in the region of the toluene dimer and, in the inset, an expanded view recorded in the region of the $C_5H_5^+$, $C_7H_7^+$ and $C_7H_8^+$ peaks. The mass spectra were recorded with the TOF-MS as it allows access to a wider mass range and provides a higher mass resolution than the QMS.

The electronic transitions of toluene were recorded by tuning the quadrupole mass spectrometer to transmit the $C_7H_8^+$ (*m/z* 92), $C_7H_7^+$ (*m/z* 91) or the $C_5H_5^+$ (*m/z* 65) ions and their respective intensities were monitored as a function of wavelength. It should be mentioned that whilst other ion fragments from toluene were investigated, due to their weak signal intensity in the mass spectrum an electronic spectrum could not be

115

recorded. In order to demonstrate whether conventional depletion spectroscopy could be used to record the electronic transitions, the helium dimer cation (He_2^+ (m/z 8)) and other He_n^+ ions were also monitored as a function of wavelength.

The near-ultraviolet light was generated using a combination of a Nd:YAG laser, a Continuum Surelite II-10 model, which was used to pump a Sirah dye laser equipped with a frequency doubling unit. The dye laser was operated using Coumarin 503, which allows access to wavelength ranges between 483-541 nm and generated a pulse energy of 3 mJ in the UV. The UV light was aligned counter-propagating to the helium droplet beam to achieve maximum spatial overlap of the two beams. The electronic spectrum was acquired with the collection method described in Chapter 2 and each point was averaged for 400 laser shots using a laser step size of 0.3 cm^{-1}.

5.3.   EXPERIMENTAL RESULTS

5.3.1. Electronic spectra of toluene recorded in the region of the S_1-S_0 0_0^0 electronic transition.

Figure 5.2 shows electronic spectra of toluene recorded in the region of the S_1-S_0 0_0^0 electronic transition, acquired by monitoring the $C_7H_7^+$ and $C_5H_5^+$ ion channels. The electronic spectra were recorded using the collection method described in Chapter 2, using a gate width of 2.5 ms for the background and signal gates. It should be mentioned that when the laser was tuned into the S_1-S_0 0_0^0 transition the $C_5H_5^+$ channel exhibited an increase '*enhancement*' in its ion signal, whilst for the $C_7H_7^+$ channel a decrease '*depletion*' was observed. When recording electronic spectra on the He_n^+ channels and the $C_7H_8^+$ channel no significant depletion effect on their ion channels was observed. The electronic spectra show a similar response to their corresponding depletion/enhancement signals, in that a mirror image of the electronic spectrum was

obtained. For the $C_5H_5^+$ channel an enhancement of ~ 15 % on resonance was observed whilst the $C_7H_7^+$ channel gave rise to a depletion of ~ 6 %. The observed transition frequency of the S_1-S_0 0_0^0 transition was blue shifted by *ca.* ~ 50 cm^{-1} relative to the gas phase, which is consistent with a previous study of the electronic transition of toluene in helium droplets.[9] The electronic spectrum of toluene was also attempted by monitoring the $C_7H_8^+$ channel, but no significant depletion was observed.
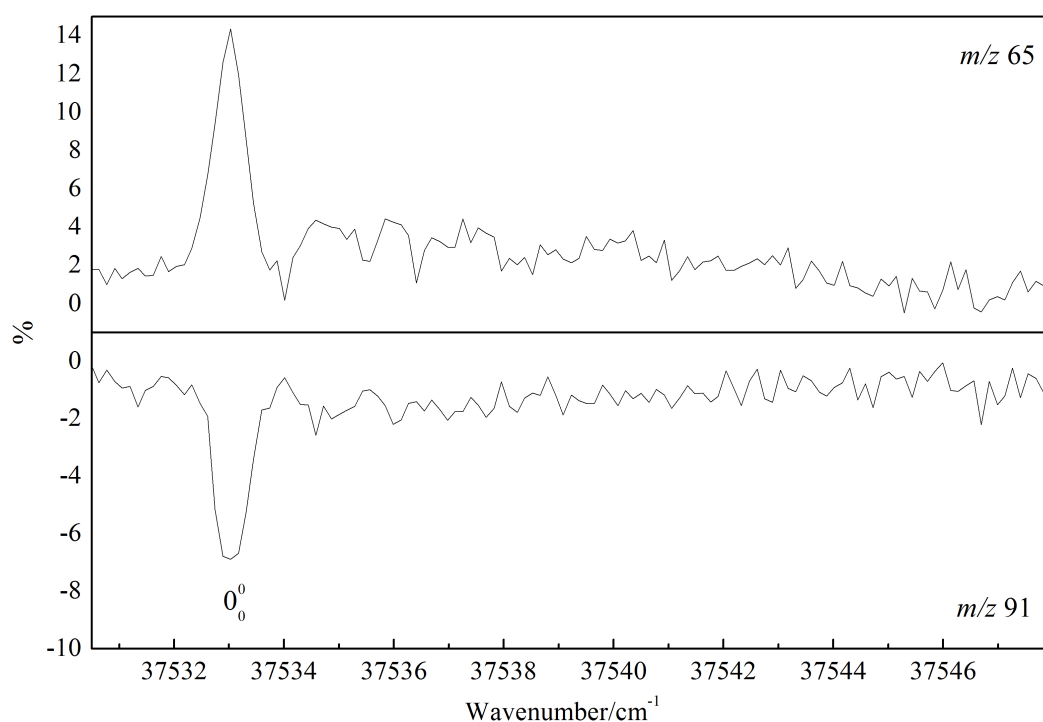
Figure 5.2. Electronic spectra of toluene recorded in the region of the S_1-S_0 0_0^0 electronic transition, acquired by monitoring the $C_7H_7^+$ and $C_5H_5^+$ ion channels.

Figure 5.3 shows the electronic spectrum of toluene recorded in the region of the S_1-S_0 0_0^0 electronic transition, acquired by monitoring the He_2^+ ion channel: the figure shows a ~ 0.02 % depletion in the He_2^+ ion signal. The observation of depletion in this channel implies that some of the energy absorbed by the toluene molecule is being dissipated into the droplet. Whilst efforts were made to record an electronic spectrum

on other He_n^+ channels, an electronic spectrum could not be obtained due to their low signal intensities. Since the depletion in the He_2^+ signal was much weaker than that observed for $C_7H_7^+$ it suggests that a conventional depletion process is not responsible for the electronic spectra shown in Figure 5.2, as heat dissipation into the droplet should give rise to a comparable depletion effect for all ion channels.
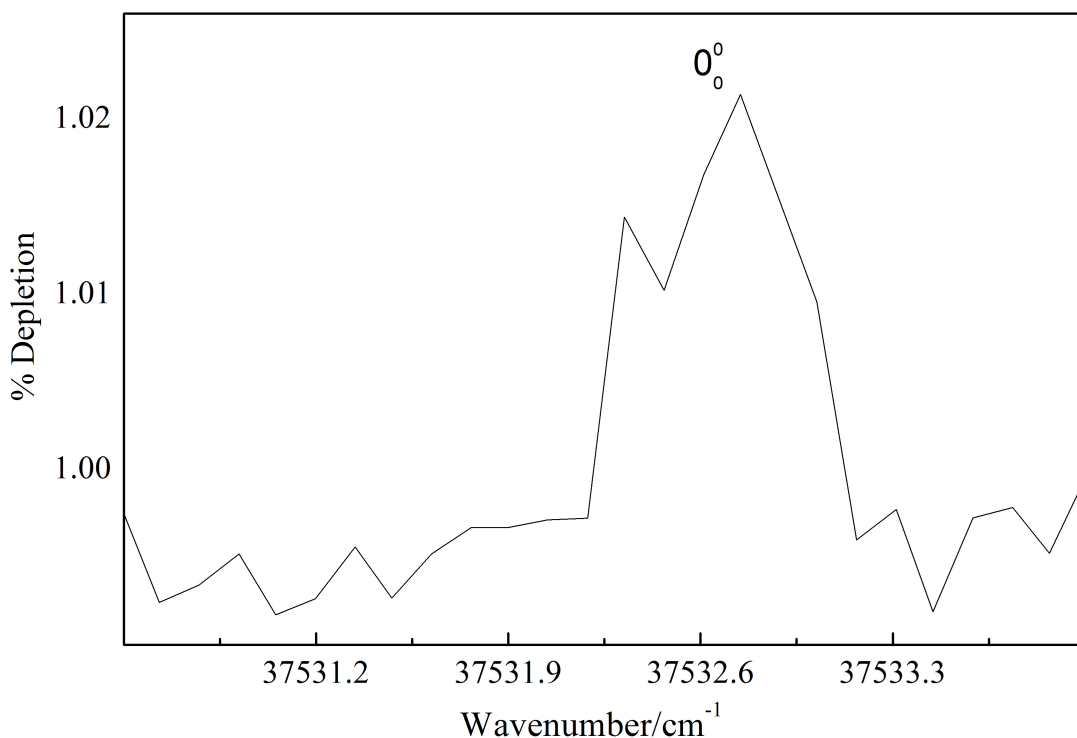
Figure 5.3. Electronic spectra of toluene recorded in the region of the S_1-S_0 0_0^0 electronic transition, acquired by monitoring the He_2^+ ion channel.

5.3.2. Selected vibrations in the electronic spectrum of toluene

Figure 5.4 shows electronic spectra recorded for the 0_0^0, 37_0^1 ($+530$ cm^{-1}), 10_0^1 ($+933$ cm^{-1}), 11_0^1 ($+964$ cm^{-1}) transitions. The transitions were readily assigned as they were all blue shifted by *ca.* ~ 50 cm^{-1} relative to the gas phase.[14] Due to relatively long acquisition times, > 2 hours per peak, data were only recorded in the region of the expected peak positions. The results show that exciting the toluene molecules into

vibrational levels other than the 0_0^0 level in the S_1 state has a similar response, in that electronic spectra were recorded by ion signal depletion and ion signal enhancement on the $C_7H_7^+$ and $C_5H_5^+$ channels respectively. When attempting to record electronic spectra of different vibrations using the He_2^+ channel and the $C_7H_8^+$ no significant spectral features could be observed.
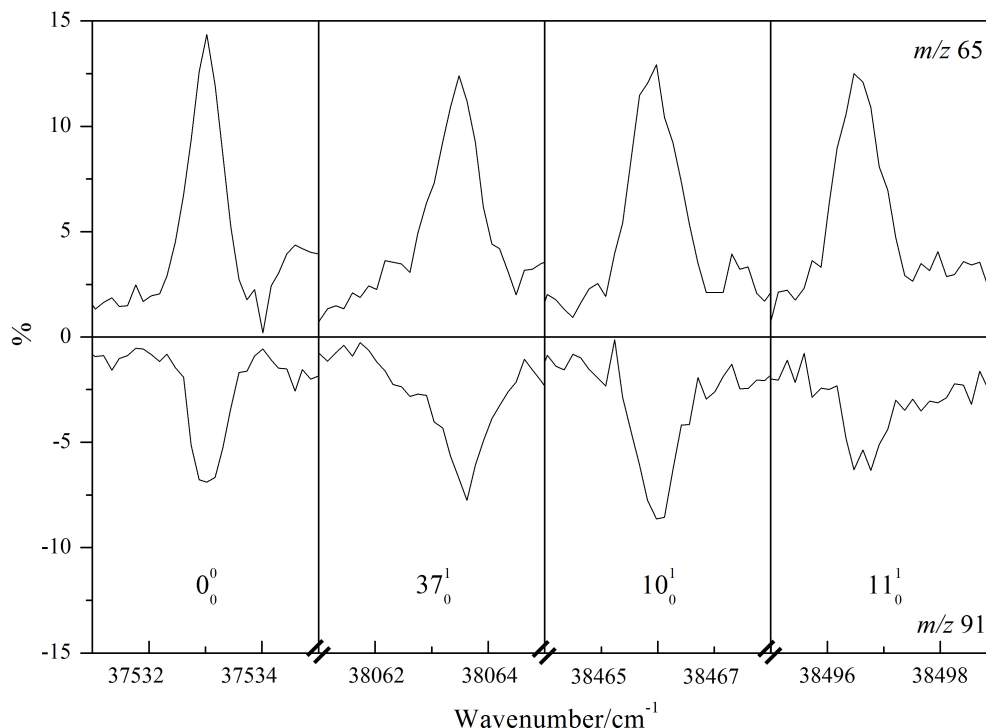
Figure 5.4. Electronic spectra of toluene recorded in the region of the S_1-S_0 electronic transition, acquired by monitoring the *m/z* 91 ($C_7H_7^+$), upper panels, and *m/z* 65 ($C_5H_5^+$), lower panels. The assignments were obtained from Ref.14.

5.4.   DISCUSSION

The experimental results have shown that the electronic spectrum of toluene can be recorded as either ion signal depletion or ion signal enhancement, by monitoring the $C_7H_7^+$ and $C_5H_5^+$ ion channels as a function of wavelength. The observation of weak depletion in the ion signals of the He_2^+ and the $C_7H_8^+$ channels, when the laser is tuned into the S_1-S_0 electronic transition, suggests that a conventional depletion process is not

responsible for the significant depletion in the ion signal of the $C_7H_7^+$ channel. This is confirmed by the enhancement of the $C_5H_5^+$ ion signal, which is unusual since an enhancement of an ion signal has not been reported previously in helium droplets. In order to interpret the experimental findings the proposed energy disposal processes that follow excitation of toluene into the S_1 state will be given before the results presented above are discussed.

5.4.1. Electronic excitation of toluene $S_1 – S_0$

Following excitation of toluene into the zero point level of the S_1 state it can undergo fluorescence, internal conversion or intersystem crossing (ISC) (see Figure 5.5). Results from experiments in the gas phase have determined that the quantum yields for fluorescence and intersystem crossing are 0.3 and 0.64 respectively and that internal conversion is a minor decay channel.[15] If the same is true for the electronic excitation of toluene within helium droplets then intersystem crossing will be the dominant process.
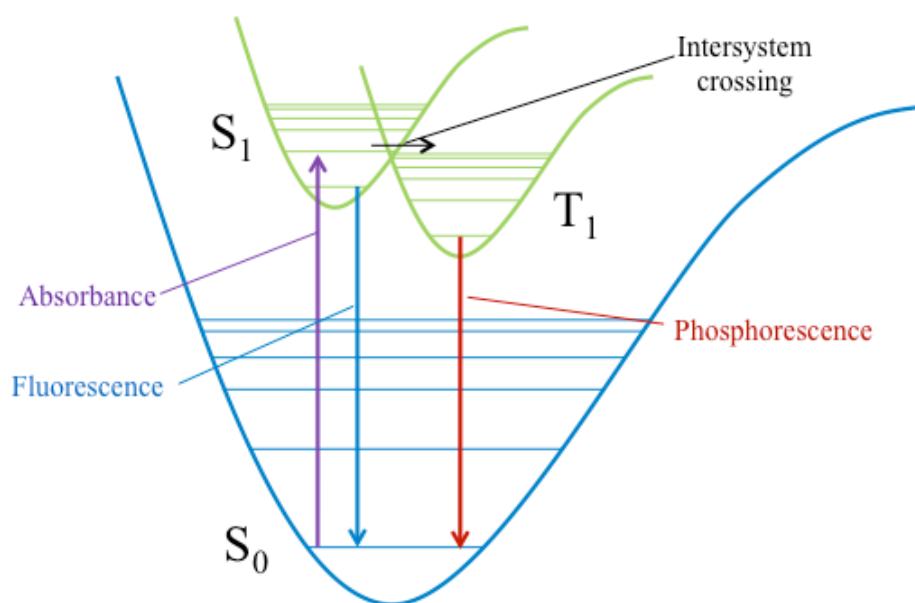
Figure 5.5. Schematic energy level diagram showing the photophysical processes following electronic excitation of toluene into the S_1 state.

The difference between the zero point levels of the S_1 and T_1 states of toluene is 8400 cm^{-1} and it is expected that ISC should convert this excess energy into vibrational energy in the toluene in the T_1 state. This would correspond to the evaporative loss of 1680 helium atoms, if it assumed that each helium atom removes 5 cm^{-1} of energy.[16] Therefore, if every toluene molecule were to decay by ISC then the evaporative loss of 1680 helium atoms, from droplets containing 11 000 helium atoms initially, will give rise to a 15 % depletion in the ionization cross-section of the droplets, assuming spherical helium droplets with cross sections dependent on $N^{2/3}$ where N is the number of helium atoms. This decrease in geometric cross section should lead to a comparable fall in the ionization cross section. Even if two thirds of the excited toluene molecules were to decay by ISC, as predicted by the ISC branching rate, a depletion of 10 % would be expected. However, in practice the experimental results have shown that the depletion on the He$_n^+$ channels and the toluene parent ion channel is < 1 %, which suggests that dissipation of the excess energy into the helium matrix is less efficient than that expected.

It should be mentioned that dissipation of some energy into the droplet is essential to prevent a second ISC from T_1 to S_0. The timescale of this second ISC will depend on the vibrational energy content of the T_1 state, which varies from ~ 10 µs for a vibrational energy content of 8400 cm^{-1} to several seconds when there is no excess vibrational energy.[17] If the rate information contained in Ref 17 is also applicable to helium droplets then in order for the toluene molecules to survive in the T_1 state from the point of laser excitation to the point of electron impact ionization, which takes approximately 1 ms, the toluene molecules must contain no more than *ca*. 1000 cm^{-1} of vibrational energy.
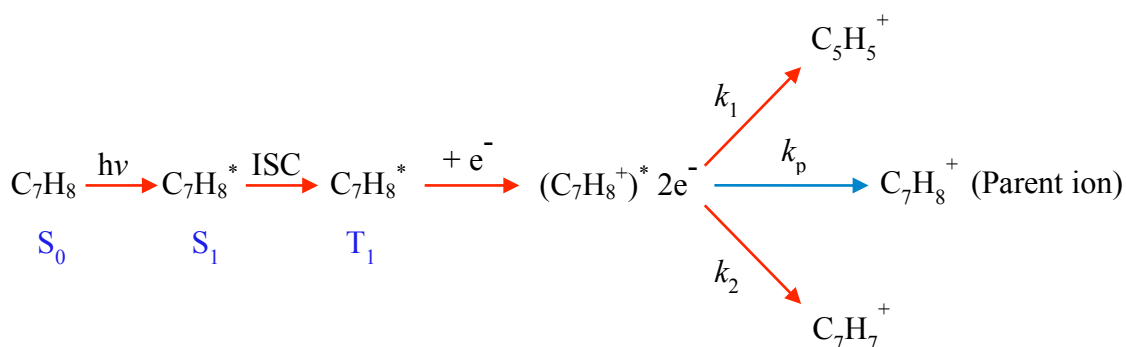
5.4.2. Hot molecule technique

From the above discussion, it is unlikely that the depletion observed in the $C_7H_7^+$ channel is a result of heat dissipation into the droplet, since a comparable depletion should have been observed on the $C_7H_8^+$ and He_n^+ channels. Instead, a different mechanism must cause the selective depletion. One possibility is that excitation of toluene to the S_1 state ultimately creates a 'hot' molecule in the T_1 state. If the dissipation of energy from this triplet state into the droplet is not very efficient, then it can be assumed that the toluene molecules will survive in this state until they arrive at the ionization region of the QMS. Electron impact ionization of toluene in its T_1 state may alter the cross-sections for some ionization channels. Whilst there was no observable difference for the $C_7H_8^+$ channel, ionization of toluene in its T_1 state might cause a reduction in the cross-section for forming the $C_7H_7^+$ fragment.

If this is the case, ionization of toluene in its T_1 state may also alter the branching ratios for other fragments, which could cause a reduction in the ionization cross-sections for some fragments whilst others might increase. The latter of these is illustrated by the enhancement of the $C_5H_5^+$. Since the formation of ion fragments following electron impact ionization will depend on their relative energetics of formation, knowledge of the structure of the ions will be important. Unfortunately in this study the identity of the ions has not been determined. However, the identities and the enthalpy of formation of the $C_5H_5^+$ and $C_7H_7^+$ has been listed in a previous study, which investigated the cross-sections of molecular ions and ionic fragments formed following electron impact ionization of toluene.[18] The $C_7H_7^+$ is likely to be the benzyl cation or the tropylium cation, whereas the $C_5H_5^+$ could be the cyclopentadienyl cation or the vinylcyclopropenyl cation. Regardless of the correct assignment of the $C_5H_5^+$ and

the $C_7H_7^+$, the enthalpy of formation of $C_5H_5^+$ always lies above the $C_7H_7^+$ with the minimum difference being between the benzyl and vinylcyclopropenyl cation ~ 1 eV.[18]

If it is assumed that the ions are formed by a simple unimolecular decay process, then ionization of toluene in its T_1 state might increase the rate of decay of $C_7H_8^+$ into $C_5H_5^+$ whilst the formation of $C_7H_7^+$ decreases, which would account for the observed enhancement/depletion effects on these channels. Consequently, the electronic spectrum is obtained by monitoring the relative change of the branching ratios $\Delta k_1 / k_p$ or $\Delta k_2 / k_p$, depending on the fragment mass channel monitored. The key processes for recording electronic spectra of toluene using the hot molecule technique are summarised in Figure 5.6.

Figure 5.6. Schematic showing the suggested mechanism for the 'hot' molecule technique. Following excitation of toluene to its S_1 state it undergoes ISC to its T_1 state with a high quantum yield. The toluene molecules will remain in the T_1 state until they arrive at the ionization region of the QMS. Electron impact ionization of toluene molecules in the triplet state alters the branching ratios of $C_5H_5^+$ and $C_7H_7^+$, which leads to an increase in the rate of formation of $C_5H_5^+$ and a decrease for $C_7H_7^+$. The optical spectrum is recorded as either ion signal enhancement or depletion, respectively.

Since the droplet sizes used were made deliberately large to minimize the contribution from conventional depletion spectroscopy, the weak signals observed on the $C_6H_8^+$ and He_n^+ would be expected given the small amount of excess vibrational energy available to be dissipated. Consequently, if smaller droplet sizes were employed

the depletion effect for these ions would be much more predominant. In contrast to conventional depletion spectroscopy the 'hot' molecule technique offers a potential advantage in that it allows for the use of slightly larger droplet sizes. This is because the depletion/enhancement is not a result of heat dissipation into the droplet, but instead relies on a change in the ionization cross-section of specific ion fragments following optical excitation and subsequent formation of a molecule in a metastable state. However, a potential limitation of the technique is that molecular ions, formed after charge transfer ionization, must to be able to escape from the droplet. Results from previous investigations have suggested that this limit will be reached for droplet sizes containing between $<N> = 4 \times 10^4$ and $<N> = 6 \times 10^4$ helium atoms.[19,20]

5.5.   CONCLUSION

In this chapter, a new technique for recording optical spectra has been reported. The technique relies on a change in the ionization cross-section of specific ion fragments following optical excitation and subsequent formation of a molecule in a metastable state. In the current study the technique has been successfully applied to record electronic spectra of toluene in its T_1 state, which was populated by intersystem crossing following excitation to its S_1 state. It was found that by monitoring either the $C_5H_5^+$ or the $C_7H_7^+$ ion as a function of wavelength the optical spectrum could be obtained as either ion signal enhancement or depletion, respectively.

The limitations of the technique are that it requires that molecules remain in an excited state when they arrive at the ionization region of the QMS and that molecular ions, formed after charge transfer ionization, are able to escape from the droplet. The former of these is important to alter the cross-sections of specific ion fragments and the latter will depend on the droplet size. However, the technique has the potential to be

very effective for investigating spectroscopic transitions of other species that remain in a long-lived metastable state within helium droplets. This will include the further study of other aromatic molecules, which undergo ISC and potentially for the study of some diatomic molecules that remain in long-lived vibrational states in helium droplets.[21]

REFERENCES FOR CHAPTER 5

1. J. P. Toennies, A. F. Vilesov, *Annu. Rev. Phys. Chem.,* 1998, **49**, 1.

2. J. P. Toennies, A. F. Vilesov, *Angew. Chem. Inst. Ed*. 2004, **43**, 2622.

3. R. Frochtenicht, J.P. Toennies, A. Vilesov, *Chem. Phys. Lett.*, 1994, **229**, 1.

4. S. Goyal, D. L. Schutt, G. Scholes, *Phys. Rev. Lett*., 1992, **69**, 933.

5. K. Nauta, R. E. Miller, *Phys. Rev. Lett.*, 1999, **82**, 4480.

6. M. Hartmann, A. Lindinger, J. P. Toennies and A. F. Vilesov, *J. Phys. Chem. A*, 2001, **105**, 6369.

7. S. Kuma, H. Goto, M. N. Slipchenko, A. F. Vilesov, A. Khramov, T. Momose, *J. Chem. Phys*., 2007, **127**, 214301.

8. E. Loginov, D. Rossi and M. Drabbels, *Phys. Rev. Lett*., 2005, **95**, 163401.

9. A. Boatwright, N. A. Besley, S. Curtis, R. R. Wright, A. J. Stace, *J. Chem. Phys.*, 2005 **123**, 021102.

10. A. V. Kanaev, L. Museur, T. Laarman, M. C. Castex, S. Monticone, K. von Haeften and T. Möller, *J. Chem. Phys.*, 2001, **115**, 10248.

11. J. P. Toennies, A. F. Vilesov, *Annu. Rev. Phys. Chem.,* 1998, **49**, 1.

12. J. P. Toennies, A. F. Vilesov, *Angew. Chem. Inst. Ed*. 2004, **43**, 2622.

13. NIST Chemistry WebBook, see http://webbook.nist.gov/chemistry/

14. C. G. Hickman, J. R. Gacokke, W. D. Lawrence, *J. Chem. Phys*., 1996, **104**, 4887.

15. T. G. Dietz, M. A. Duncan, R. E. Smalley, *J. Chem. Phys.*, 1982, **76**, 1227.

16. J. P. Toennies, A. F. Vilesov, *Angew. Chem. Inst. Ed*. 2004, **43**, 2622.

17. H. G. Löhmannsröben, K. Luther, M. Stuke, *J. Phys. Chem.*, 1987, **91**, 3499.

18. J. R. Vacher, F. Jorand, N. Blin-Simiand, S. Pasquiers, *Chem. Phys. Lett.*, 2007, **434**, 188.

19. W. K. Lewis, B. A. Applegate, J. Sztaray, B. Sztaray, T. Baer, R. J. Bemish, R. E. Miller, *J. Am. Chem. Soc.*, 2004, **126**, 11283.

20. S. Yang, S. M. Brereton, M. D. Wheeler, A. M. Ellis, *J. Phys. Chem. A*, 2006, **110**, 1791.

21. C. M. Lindsay, W. K. Lewis, R. E. Miller, *J. Chem. Phys.*, 2004, **121**, 6095.

CHAPTER 6

INFRA-RED DEPLETION SPECTROSCOPY OF WATER-METHANE

BINARY CLUSTERS: CH$_4$(H$_2$O)$_n$ (n = 1-3)

This chapter presents details of a preliminary study of the infrared spectrum of water-methane binary clusters within helium droplets. Infrared spectra were recorded for CH$_4$, H$_2$O and a mixture of both. The experimental spectra were compared with the vibrational frequencies of CH$_4$, H$_2$O and CH$_4$(H$_2$O)$_n$ predicted from *ab initio* calculations in order to identify possible structures for the complexes (n = 1-3) based on their vibrational transitions.

6.1. INTRODUCTION

Since the infrared spectrum of SF$_6$ in helium droplets was successfully recorded, using infrared beam depletion spectroscopy,[1] considerable progress has been made in the spectroscopic analysis of isolated molecules within helium droplets.[2,3] For example, with the use of infrared beam depletion spectroscopy, Hartmann *et al*. found that captured molecules are cooled to the equilibrium temperature of the droplets, 0.37 K, and that they rotate freely within their interior.[4] More recently, Miller *et al*. have used infrared spectroscopy to demonstrate that the dopant pickup process can create unique structures, such as the cyclic hexamer of water[5] and linear chains of HCN molecules.[6]

The very low equilibrium temperature of the droplets makes them ideal for studying the interactions between weakly bound intermolecular complexes. This is particularly useful when attempting to model the chemistry in the upper atmosphere and interstellar medium. Recently, Vilesov *et al*. investigated the interactions between water in complexes with N$_2$, O$_2$ and Ar within helium droplets.[7,8] From a combination of

theoretical and experimental data they were able to determine infrared intensities and possible structures for the H_2O-X (X = Ar, N_2, O_2) complexes. The ability to model the interactions between weakly bound species is important as it provides a basis for understanding the interactions between molecules in larger systems.

In this work, infrared spectroscopy was used to investigate water/methane complexes within helium droplets. Knowledge of the interactions between water and methane is important in understanding the formation of water methane ices in the interstellar medium and the formation of methane hydrates. Methane hydrates are crystalline solids composed of methane and water molecules that form as a result of their physical force of attraction.[9] One of the main interests in methane hydrates is their potential to be used as an alternative energy resource, as it is estimated that more methane is trapped in methane hydrates than any other fossil fuel.[10]

The water-methane dimer (CH_4-H_2O) has been investigated previously by Dore *et al.*, who used far infrared spectroscopy to observe vibration-rotation tunnelling bands.[11] Various theoretical investigations have suggested two possible structures for CH_4-H_2O.[12-14] In the first structure, the CH_4 acts as a proton donor and the two molecules are linked by CH_4 donating a hydrogen atom to the oxygen atom. In the other structure the carbon atom acts as a proton acceptor for one of the hydrogen atoms from the water.[12] From a perturbation theory analysis carried out by Szczesniak *et al.*, the contributions to the attractive forces (electrostatic, induction, dispersion) favour the proton donor structure and repulsion favours the proton acceptor form, with the repulsion being decisive therefore the proton acceptor structure is the global potential energy minimum.

Whilst the water dimer has been the focus of both experimental and theoretical investigations there have been no experimental investigations of $CH_4(H_2O)_n$ complexes

for $n \geq 2$. However, these complexes have been the focus of a couple of theoretical studies. Ruckenstien *et al*. have carried out MP2 calculations on $CH_4(H_2O)_n$ complexes for n = 1, 4, 6, 8, 10.[15] For n = 10 they found that the structure is highly influenced by the hydrogen bonding amongst the water molecules and the water tends to form a cage around the methane molecule. Kryachko *et al*. have also used MP2 calculations to investigate the $CH_4(H_2O)_2$ complex and identified three possible structures, all with similar energies.[16]

In this chapter infrared spectra were recorded for pure water, pure methane and $CH_4(H_2O)_n$ complexes for $2 \leq n \geq 5$. The spectral features have been interpreted with the use of *ab initio* calculations and suggest that the CH_4 molecule will reside at the surface of a water cluster rather than be solvated in the interior.

6.2. EXPERIMENTAL

The experimental apparatus has been described in detail in Chapter 2, so only a brief description of the experimental setup will be provided here. Helium droplets were produced using a continuous source and were detected with the use of a reflectron time-of-flight mass spectrometer (TOF-MS) and a quadrupole mass spectrometer (QMS). The TOF-MS was used to record most mass spectra, as it has a higher mass resolution than the QMS, whilst the QMS was used to monitor specific ion channels as a function of wavelength. The nozzle was operated with helium stagnation conditions of 15 K and 20 bars, which gave droplet sizes containing an average of $<N>$ = 2300 helium atoms.[17]

In order to assign the spectral transitions arising from water and methane, pure samples of methane and water were recorded prior to the mixed methane/water experiment. In the pure methane experiment the amount of methane added was

carefully controlled to ensure the pickup of a single molecule. For the pure water experiment the amount of water added was controlled so that the droplets picked up no more than five water molecules. In the mixed methane/water experiment the partial pressure of water was made deliberately higher than that of methane so that at most no more than one methane molecule would interact with water clusters ranging from $n = 2$-5. Unlike the experiments described in Chapter 4, methane and water were added into a single pickup cell. In all cases the amount of species added was gauged using the ion signal intensity of parent ion of either CH_4 or H_2O in the electron impact mass spectrum. The corresponding mass spectra for methane, H_2O and mixed methane/H_2O are shown in Figures 6.1, 6.2 and 6.3 respectively.
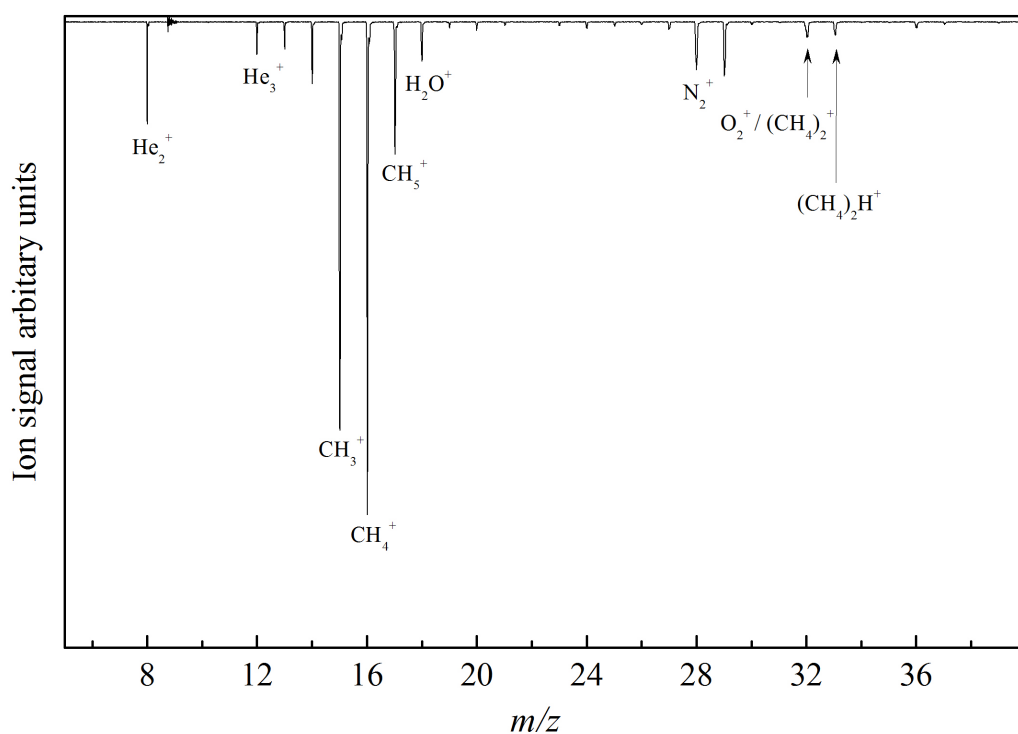
Figure 6.1. Mass spectra recorded in the region of the methane monomer (CH_4^+) and dimer (($CH_4)_2^+$).

The weak ion signal intensity of the methane dimer when compared to the monomer peak indicates that the pickup was optimised for a single methane molecule.
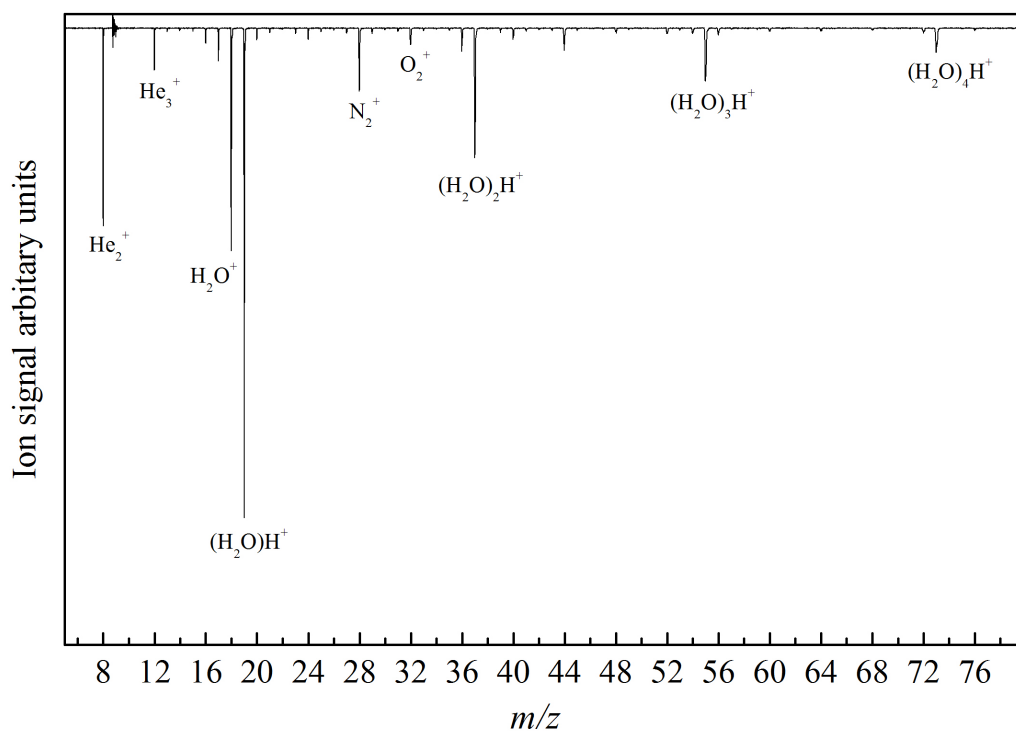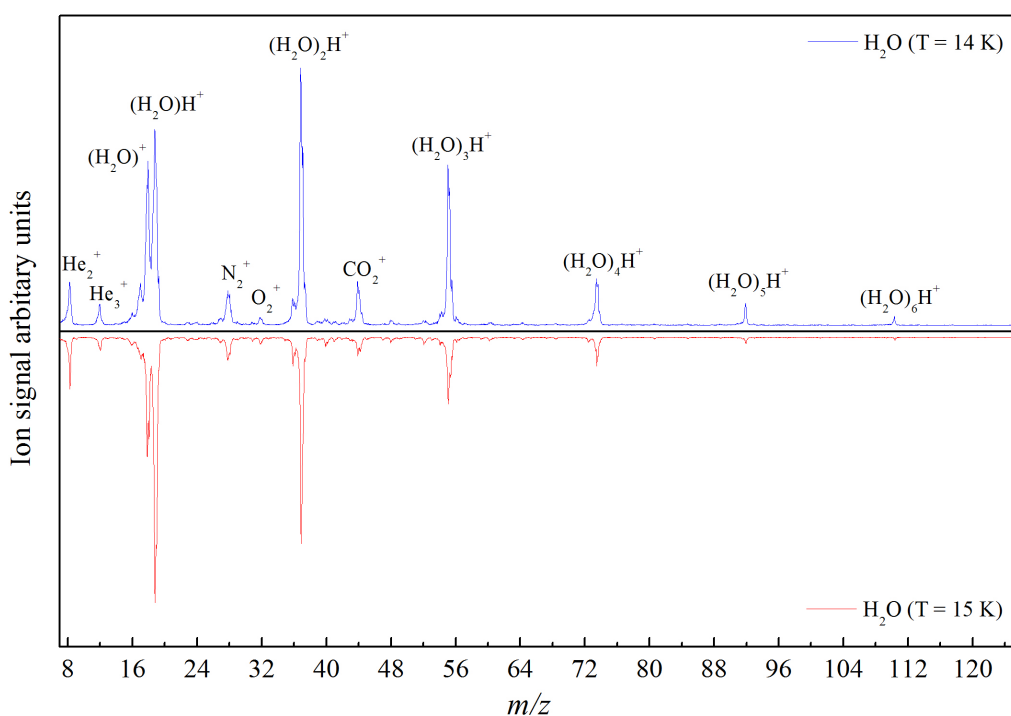
Figure 6.2. Mass spectrum showing the pickup of pure water clusters.
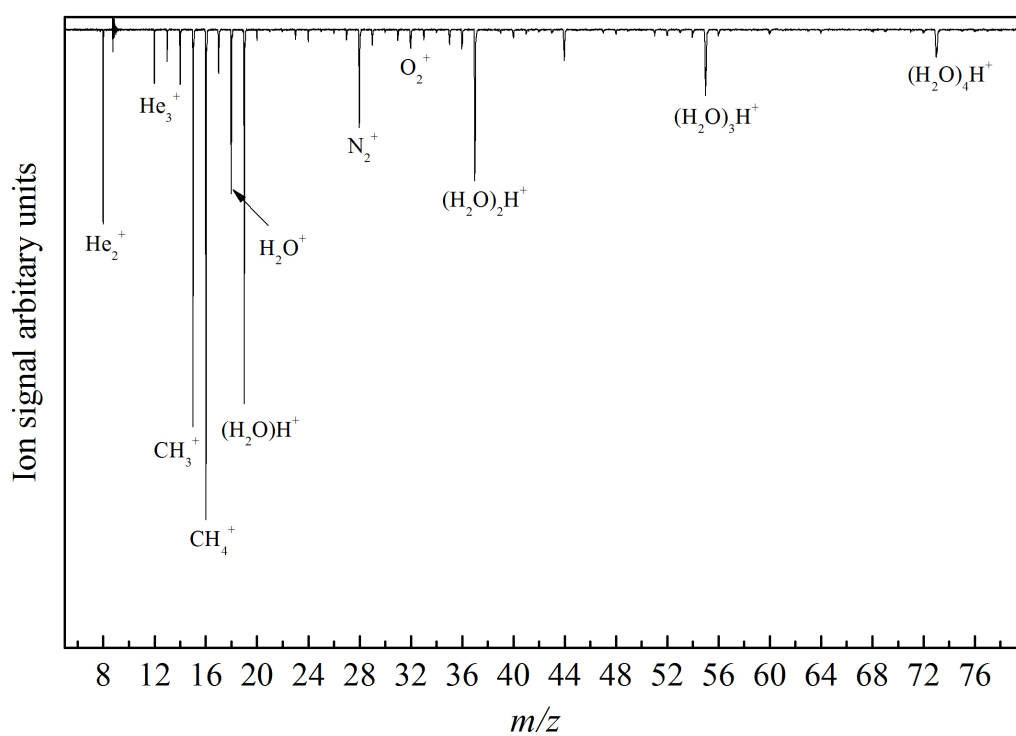

Figure 6.3. Mass spectrum showing the pickup of a mixture of methane and water.

132

In addition to the water-methane work, infrared spectra were also recorded on a variety of water cluster ions, $(H_2O)_n^+$ (n = 2, 3, 4, 5, 6, 7), to investigate the response of the infrared spectra to various partial pressures of water and to determine which ion channels would give the best signal-to-noise ratio. For the smaller water cluster ions, n = 2-3, stagnation conditions of 15 K and 20 bars were used. For the larger cluster ions, n = 4-7, slightly larger droplet sizes were employed as the signal intensities of these ions were very weak even when a high partial pressure of water was used. The mass spectra recorded under the different stagnation conditions ($<N>$ = 3300 helium atoms) are shown in Figure 6.4.

Figure 6.4. Mass spectra showing the pickup of water clusters under stagnation conditions of 14 K and 20 bars (upper panel), and 15 K and 20 bars (lower panel), recorded using the QMS.

Infrared spectra were recorded by tuning the quadrupole mass spectrometer to the He_2^+ (m/z = 8), CH_4^+ (m/z = 15) and various protonated water cluster ion channels, $(H_2O)_nH^+$ (n = 1, 2, 3, 4, 5, 6). Protonated water cluster ions were used as their ion signal intensities was much larger than the corresponding un-protonated water cluster ions. Since the fragmentation of water cluster ions will most likely occur by the following process:

$$(H_2O)_n + He^+ \rightarrow H^+(H_2O)_{n-1} + OH + He$$
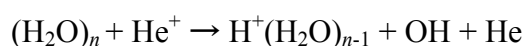
infrared spectra recorded on the H_3O^+ (19 m/z), $(H_2O)_2H^+$ (m/z = 37), $(H_2O)_3H^+$ (m/z = 55), $(H_2O)_4H^+$ (m/z = 73), $(H_2O)_5H^+$ (m/z = 91) and $(H_2O)_5H^+$ (m/z = 108) ion channels were taken to represent contributions from mostly the water dimer, trimer, tetramer, pentamer, hexamer and heptamer, respectively. However, it is recognised that contributions from larger neutral clusters are distinctly possible.

The infrared beam was generated using a combination of a Nd:YAG, Continuum Surelite laser and an optical parametric oscillator-amplifier (LaserVision; repetition rate 10 Hz; bandwidth 2-3 cm^{-1}, pulse energy 5 mJ as it enters the spectrometer via a sapphire window), which was aligned counter-propagating to the helium droplet beam to achieve maximum spatial overlap of the two beams. The infrared depletion spectrum was acquired with the collection method described in Chapter 2 and each point was averaged for 400 laser shots using a laser step size of 0.06 cm^{-1}.

6.3.   COMPUTATIONAL DETAILS

In order to aid the interpretation of the experimental results *ab initio* calculations

were performed using MP2 methodology along with an aug-cc-pVTZ basis set. The aim of the calculations was to determine structures and vibrational frequencies of $CH_4(H_2O)_n$ complexes for n = 1-3. To determine the accuracy of the results, calculations were also performed on CH_4 and $(H_2O)_m$ clusters. For the CH_4-H_2O dimer, calculations were performed on both the proton donor and acceptor structures as reported by Szczesniak et al.[12] For the $CH_4(H_2O)_2$ complex, similar structures to those reported by Kryachko et al.[16] were used. As there were no previous studies of the $CH_4(H_2O)_3$ complex, attempts were made to find possible isomers by starting from a variety of initial structures. In order to verify if a true minimum had been found, vibrational frequencies calculations were carried out on the optimised structures. The vibrational frequency calculations were also used to predict infrared spectra. All of the calculations presented here were performed using GAUSSIAN 03[17] and were run on ALICE, the high performance computing (HPC) cluster, at the University of Leicester.

6.4. EXPERIMENTAL RESULTS

6.4.1. Water clusters

Figure 6.5 shows a selection of infrared spectra recorded in the region of the O-H stretching vibrations for pure water clusters. Spectra were recorded using the He_2^+, H_3O^+ and $(H_2O)_2H^+$ ion channels. The spectra shown in panels (d) and (c) were recorded with pickup conditions optimised for the addition of two and five water molecules, respectively. Panels (a) and (b) were recorded with pickup conditions optimised for six water molecules. The band assignments of the water dimer through to the hexamer were taken from previous studies of water clusters in helium droplets.[5,19] The He_2^+ channel was used to record an infrared spectrum with the lowest partial pressure of water, as this channel will represent the overall change in droplet size and

will include contributions from the water monomer, which would otherwise be absent by monitoring water cluster ion channels for $n > 1$.
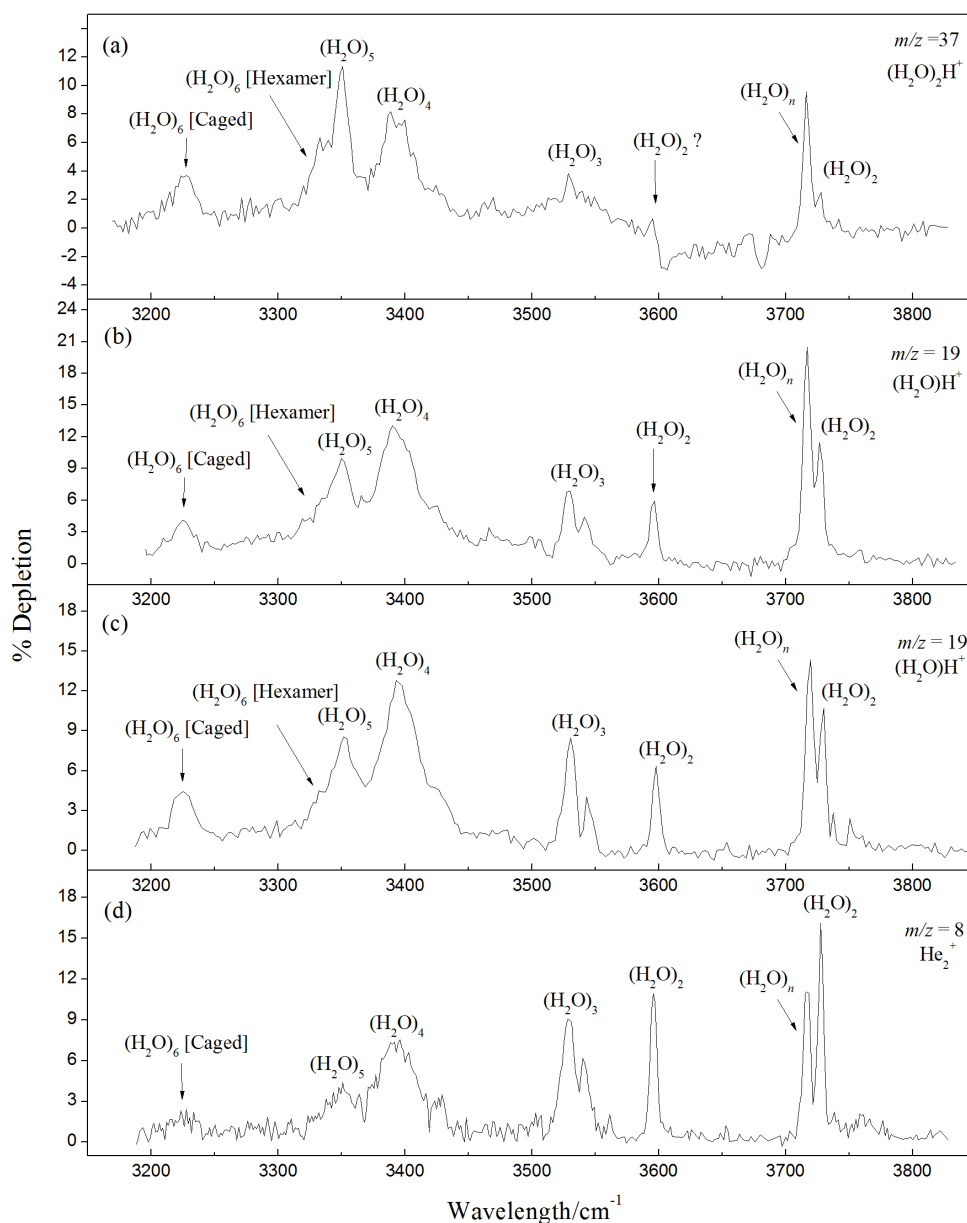
Figure 6.5. Infrared spectra of water recorded in the OH stretching region. Spectra were recorded with a relatively low water partial pressure to minimize contributions from large water clusters. The assignments were taken from previous studies of water clusters in helium droplets.[5,19] The bands assigned to $(H_2O)_2$ and $(H_2O)_n$, at 3729 cm^{-1} and 3717 cm^{-1} respectively, arise from the free O-H stretch of a donor molecule from the water dimer and larger water cluster sizes respectively. The band assignments of $(H_2O)_2$ through to $(H_2O)_6$ [caged], between 3620 – 3190 cm^{-1}, arise from the bonded O-H stretch of a donor molecule.

Attempts were made to record an infrared spectrum on the water monomer channel, H_2O (*m/z* 18), but the depletion was very weak in comparison to that obtained on the protonated water channels. This was presumably due to the contribution of background H_2O in the system to this channel. The bands assigned to $(H_2O)_2$ and $(H_2O)_n$, at 3729 cm^{-1} and 3717 cm^{-1} respectively, arise from the free O-H stretch of a donor molecule from the water dimer and larger water cluster sizes respectively. The band assignments of $(H_2O)_2$ through to $(H_2O)_6$ [caged], between $3620 - 3190$ cm^{-1}, arise from the bonded O-H stretch of a donor molecule. In agreement with previous studies of water clusters in helium droplets, the relative intensity of the $(H_2O)_n$ band is much larger in Panel (b) when compared to (c), which indicates that it must arise from larger water cluster sizes.[5,19]

Whilst spectra recorded on the He_2^+ and H_3O^+ channels compared very well with other studies in helium droplets,[5,19] the spectrum recorded on the $(H_2O)_2H^+$ channel, *m/z* 37, exhibits some unusual features. This includes the disappearance of the bands attributed to the water dimer. In a previous study that investigated infrared spectra of water clusters recorded on different ion channels, mass selection was used as way of assigning spectral transitions.[20,21] Consequently, the disappearance of bands attributable to the dimer would be expected since the water dimer cannot contribute to the trimer channel (as represented by the $(H_2O)_2H^+$ channel mas channel).

Figure 6.6 shows a selection of infrared spectra recorded with stagnation conditions of 14 K and 20 bars in the region of the OH-stretch vibrations. In contrast to Figure 6.5 slightly larger droplets, containing $<N> = 3300$ helium atoms, were used to increase the ion signals of larger water cluster cations in the mass spectrum. Spectra were recorded on $(H_2O)_nH^+$ ion channels for $n = 3$-6. The spectra shown in panels (a)-(d) were recorded with pickup conditions optimised for large water cluster sizes $n \geq 7$.

In contrast to the data shown in Figure 6.5 the spectra have become broader as a result of the pickup conditions. Consequently it is difficult to extract any useful information about water clusters for $n \geq 7$.
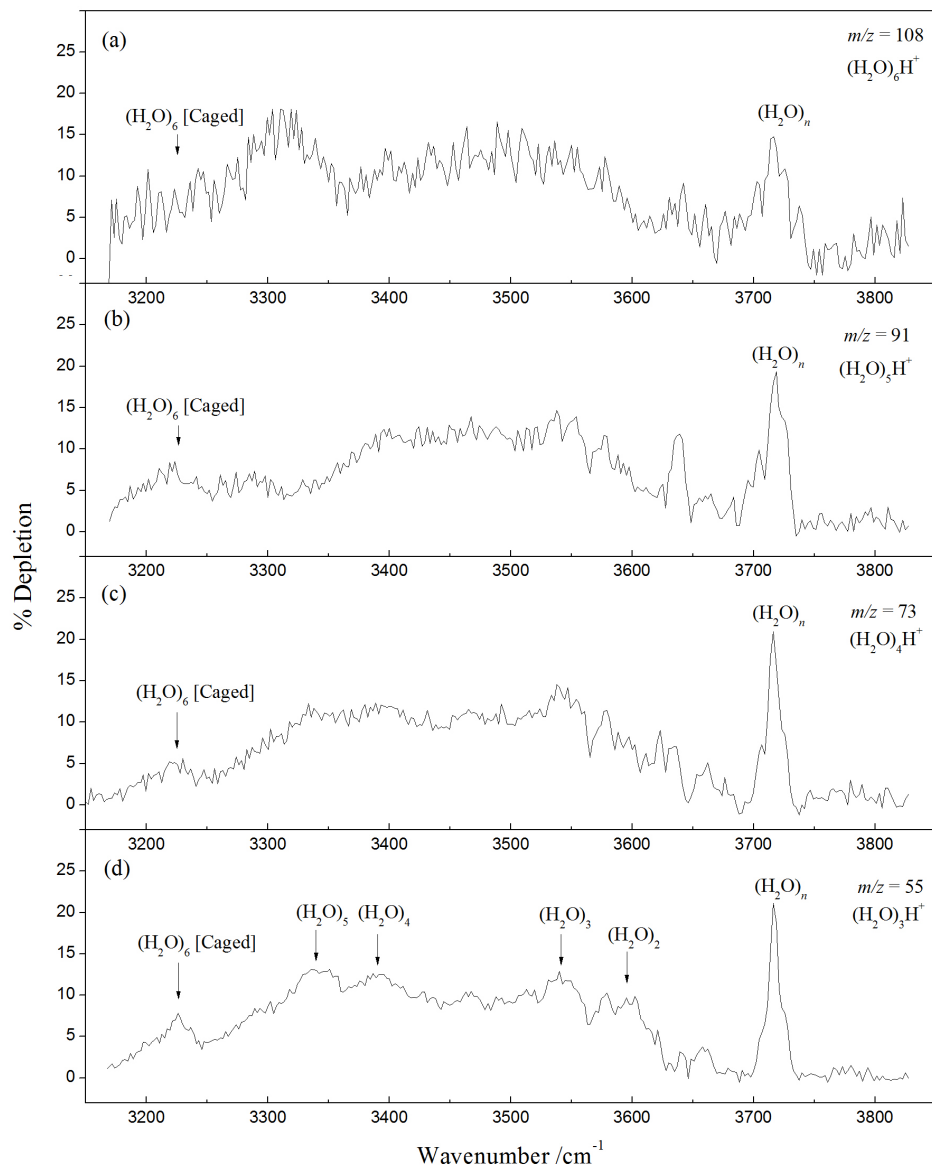
Figure 6.6. Infrared spectra of water recorded in the OH stretching region. Spectra were recorded with stagnation conditions of 14 K and 20 bars. The pickup conditions were optimized for large water cluster sizes.

6.4.2. Water clusters: experiment vs ab initio calculations

Figure 6.7 shows an expanded view of the spectrum shown in panel c of Figure 6.5, which covers the region of the water dimer and trimer. The band assignments were
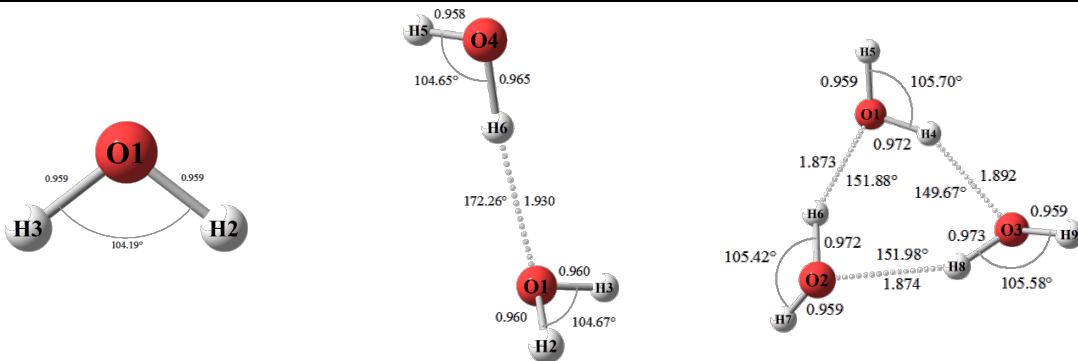
138

taken from a previous study of the water dimer in helium droplets and represent four types of vibrations, which depend on whether the monomer molecule acts as a proton donor (hydrogen bond donor) or the oxygen atom acts as a proton acceptor.[22]
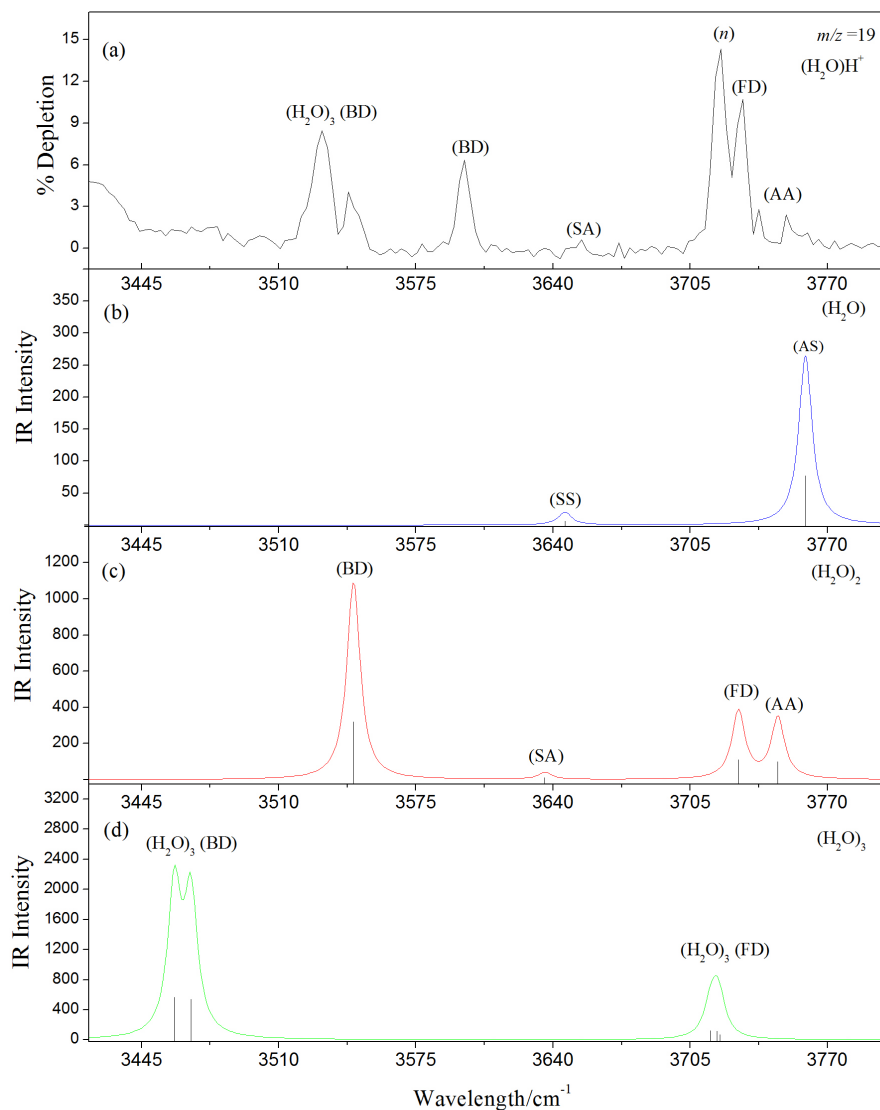
Figure 6.7. (a) Expanded view of the IR spectrum of water clusters. The band labels BD, SA, FD and AA apply to the water dimer. The BD label for $(H_2O)_3$ is also shown and the band labeled "n" is thought to arise from overlapping contributions from FD vibrations of the trimer and larger clusters. Panels (b), (c) and (d) show simulations derived from *ab initio* calculations for the water monomer, dimer and trimer, respectively. The calculated harmonic vibrational frequencies were scaled by a factor of 0.948 (see text for further details) and the vibrational lines were fitted to Lorentzian profiles with a full-width at half maximum of 4 cm^{-1}.

The four types of bands are: (i) the free O-H stretch of a donor molecule (FD); (ii) the

bonded O-H stretch of a donor molecule (BD); asymmetric stretch vibrations of

acceptor molecules (AA); (iv) symmetric stretch of an acceptor molecule (SA). To

demonstrate the quality of the *ab initio* calculations used in this work the predicted

infrared spectra of the water monomer, dimer and trimer are included in panels (b), (c)

and (d), respectively. The optimized geometries of H_2O, $(H_2O)_2$ and $(H_2O)_3$ are shown

in Table 6.1.

Table 6.1 Geometries of H_2O, $(H_2O)_2$ and $(H_2O)_3$ optimized at the MP2/aug-cc-pVTZ level. The values in parentheses are from a previous study of the water trimer optimized at the MP2/aug-cc-pVTZ level.[23]

Water monomer	Water dimer	Water trimer
0.959 Å	0.958 Å	0.959 Å (0.961 Å)
$r(H3\cdots O1) = r(H2\cdots O1)$	$r(H5\cdots O4)$	$r(H5\cdots O1) = r(H9\cdots O3) =$
		$r(H7\cdots O2)$
104.19°	0.965 Å	0.972 Å (0.975 Å)
$\angle$H3O1H2	$r(H6\cdots O4)$	$r(H4\cdots O1) = r(H6\cdots O2)$
	104.19°	0.973 Å (0.975 Å)
	$\angle$H5O4H6	$r(H8\cdots O3)$
	1.930 Å	0.5° (0.5°)
	$r(H6\cdots O1)$	τH8O3O1O2
	0.960 Å	-5.1° (-4.7°)
	$r(H2\cdots O1) = r(H3\cdots O1)$	τH4O1O2O3
	104.67°	0.3° (0.2°)
	$\angle$H2O1H3	τH6O2O3O1

Since water clusters for $3 \leq n \geq 6$ are known to form cyclic structures within helium droplets the water trimer was calculated in its cyclic form as opposed to a water chain.[5] The calculated harmonic frequencies were scaled by a factor of 0.948, so that the band labelled FD of the water dimer was in agreement with the experimental value. The main features observed in the experimental spectrum in panel (a) are predicted in the calculations, but unfortunately the scaling factor does not produce a good agreement for all of the band positions (see Table 6.2). The largest discrepancy occurs for the BD bands of the dimer and trimer, which are predicted ~50 cm^{-1} below their experimental values. A similar discrepancy was also reported in *ab initio* calculations carried out by Kuyanov-Prozument *et al.*[22] using MP2 methodology with a smaller basis set.

Table 6.2 Experimental and theoretical O-H stretching frequencies (cm^{-1}) for $(H_2O)_2$ and $(H_2O)_3$. The theoretical values for FD and BD for the trimer were taken from the peak maxima of the Lorentzian profiles.

Band	$(H_2O)_2$		$(H_2O)_3$	
	Expt	Theory	Expt	Theory
AA	3749	3746		
FD	3729	3728	3719	3717
SA	3654	3636		
BD	3598	3545	3530	3460

6.4.3. Methane monomer

Figure 6.8 shows the infrared spectrum of the v_3 vibrational band of the methane monomer in helium droplets. The partial pressure of methane was made deliberately low so that the pickup of a single methane molecule would dominate. The band assignments of the P(1), Q(0), R(0) and R(1) transitions were taken from a previous

study of methane in helium droplets by Miller *et al.*[24] Unfortunately, with the current

spectral resolution it is difficult to separate contributions from the dimer and larger

methane clusters, which appear as satellite bands next to the P(1), Q(0), R(0) and R(1)

transitions of the monomer.[24] Consequently, to confirm the absence of larger methane

cluster we noted the weak signal intensity of the methane dimer in the electron impact

mass spectrum.
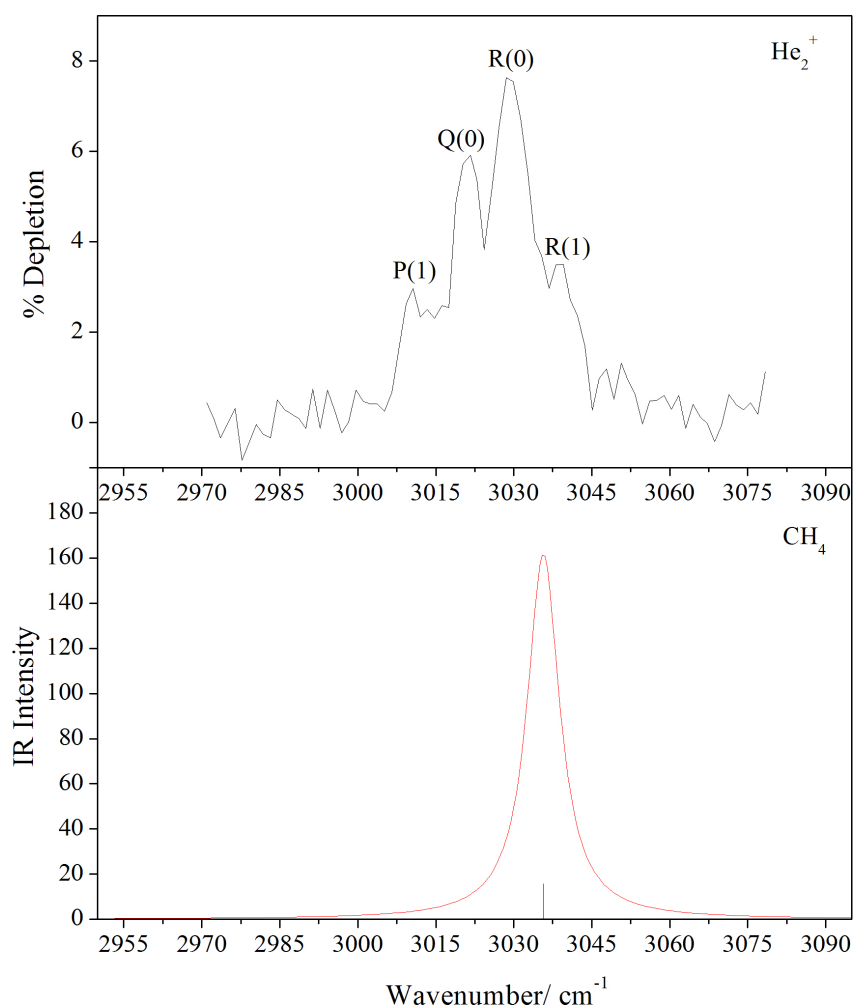
Figure 6.8. IR spectrum of the v_3 vibrational band of the methane monomer in helium droplets (upper

panel) and the simulated vibrational spectrum of CH_4 optimized at the MP2/Aug-cc-pVTZ level (lower

panel). The calculated harmonic vibrational frequencies were scaled by a factor of 0.948 and the

vibrational lines were fitted to Lorentzian profiles with a full-width at half maximum of 4 cm^{-1}. The mass

channel used for recording depletion spectra is also included in the upper panel.

The values of the experimental and simulated vibrational transitions of the methane monomer are shown in Table 6.3. The predicted value of the v_3 vibrational band of the methane monomer was scaled by the same scaling factor as that used for the OH stretching region to bring the predicted value into agreement with the experiment. The CH bond lengths and HCH bond angles were calculated to be 1.084 Å and 109.47° respectively.

Table 6.3 Experimental and theoretical C-H stretching frequencies (cm^{-1}) of CH_4.

	CH_4	
Band	Expt	Theory
v_3		3039
R(1)	3039	
R(0)	3029	
Q(0)	3020	
P(1)	3010	

6.4.4. $CH_4(H_2O)$

Table 6.4 shows the *ab initio* predictions for the two structures of the water-methane dimer. The predictions match the results reported previously by Szczesniak *et al.*[12] and have been given the labels proton acceptor and donor, depending on whether methane donates or accepts a proton. The proton acceptor form has the lowest energy of the two complexes, lying 68 cm^{-1} below the donor form.

Table 6.4 Geometries of CH_4-H_2O in its proton accepter (PA) and donor (PD) forms optimized at the MP2/aug-cc-pVTZ level. The relative energies shown (in cm^{-1}) include the zero point energy.
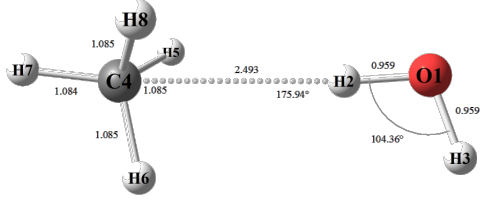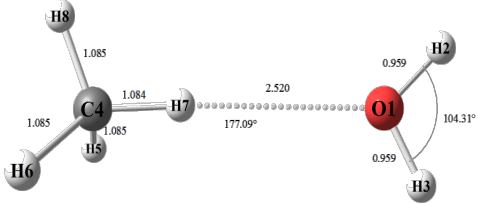

|	$CH_4(H_2O)$ (PA) +0 cm^{-1}	$CH_4(H_2O)$ (PD) 68 cm^{-1}
	$CH_4(H_2O)$ (PA)	**$CH_4(H_2O)$ (PD)**
r(H2···O1) = r(H3···O1)	0.959 Å	0.959 Å
∠O1H2C4	175.24°	177.09° ∠O1H7C4
r(H2···C4)	2.493 Å	2.520 Å
r(H5··· C4) = r(H6··· C4) =r(H8··· C4)	1.085 Å	1.085 Å
r(H7···C4)	1.084 Å	1.084 Å
∠H8 C4H6 = ∠H5 C4H6	109.87°	109.28°
∠H8 C4H7	109.01°	109.59°

Figure 6.9 shows a comparison of infrared spectra recorded in the region of the OH stretching vibrations with and without methane. The spectra were recorded on the He_2^+, m/z 8, channel and the pickup of conditions were optimised so that at most one methane molecule would interact with water clusters $(H_2O)_n$ for n =1-5. The spectra were recorded using the He_2^+ channel because bands associated with the water monomer would be absent from spectra recorded on $(H_2O)_nH^+$ channels for $n > 1$. Unfortunately, due to the current spectral resolution and the pickup conditions used, it is difficult to identify bands associated with the water monomer in the pure water spectrum (panel (a)), which should appear between 3730 – 3800 cm^{-1}.[25] When methane is co-added to the water doped droplets the bands associated with the water dimer and trimer become broader and the noise level increases. The increase in the noise level is a result of a decrease in the intensity of the He_2^+ channel following the pickup of CH_4.

Consequently, it is difficult to identify bands from the methane-water dimer. The predicted vibrational frequencies of the proton acceptor and donor forms of $CH_4(H_2O)$ are shown in panels (c) and (d), respectively.

Figure 6.10 shows infrared spectra recorded in the C-H stretching region under the same pickup conditions as for Figure 6.9. In the O-H stretching region the bands are well separated, which helps in the assignment of bands from various $CH_4(H_2O)_n$ complexes. However in the C-H stretching region the assignment of bands arising from different cluster sizes is difficult with the current spectral resolution. The experimental spectrum of the mixed water-methane experiment is shown in panel (c) and shows a red-shift relative to the pure methane spectrum. Panels (d) and (e) show the predicted spectrum for the proton accepter and donor forms respectively: both show a slight red shift relative to pure CH_4. At the current resolution it is difficult to confidently predict the structure of the water-methane dimer in helium droplets. However based on energetics the proton acceptor form would be favoured in the droplets.
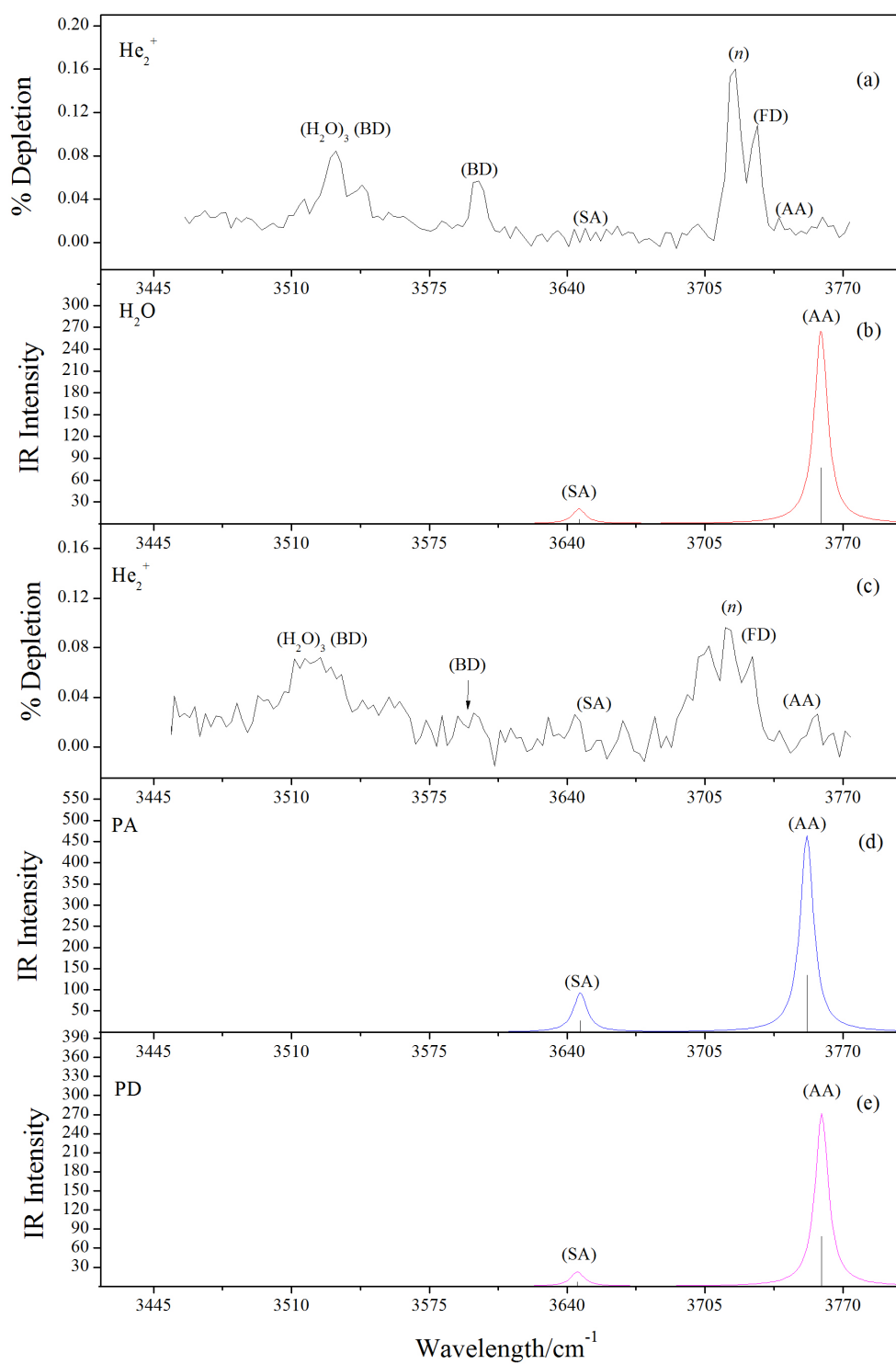
Figure 6.9. Comparison of (a) the experimental IR spectrum for pure water clusters and (b) the MP2 prediction for $(H_2O)_2$ with the experimental spectrum obtained with the addition of a small quantity of methane (c). Also shown in panels (d) and (e) are MP2 simulations for the proton acceptor and donor forms, respectively. The same scaling factor as applied for Figure 6.7, namely 0.948, was applied here.
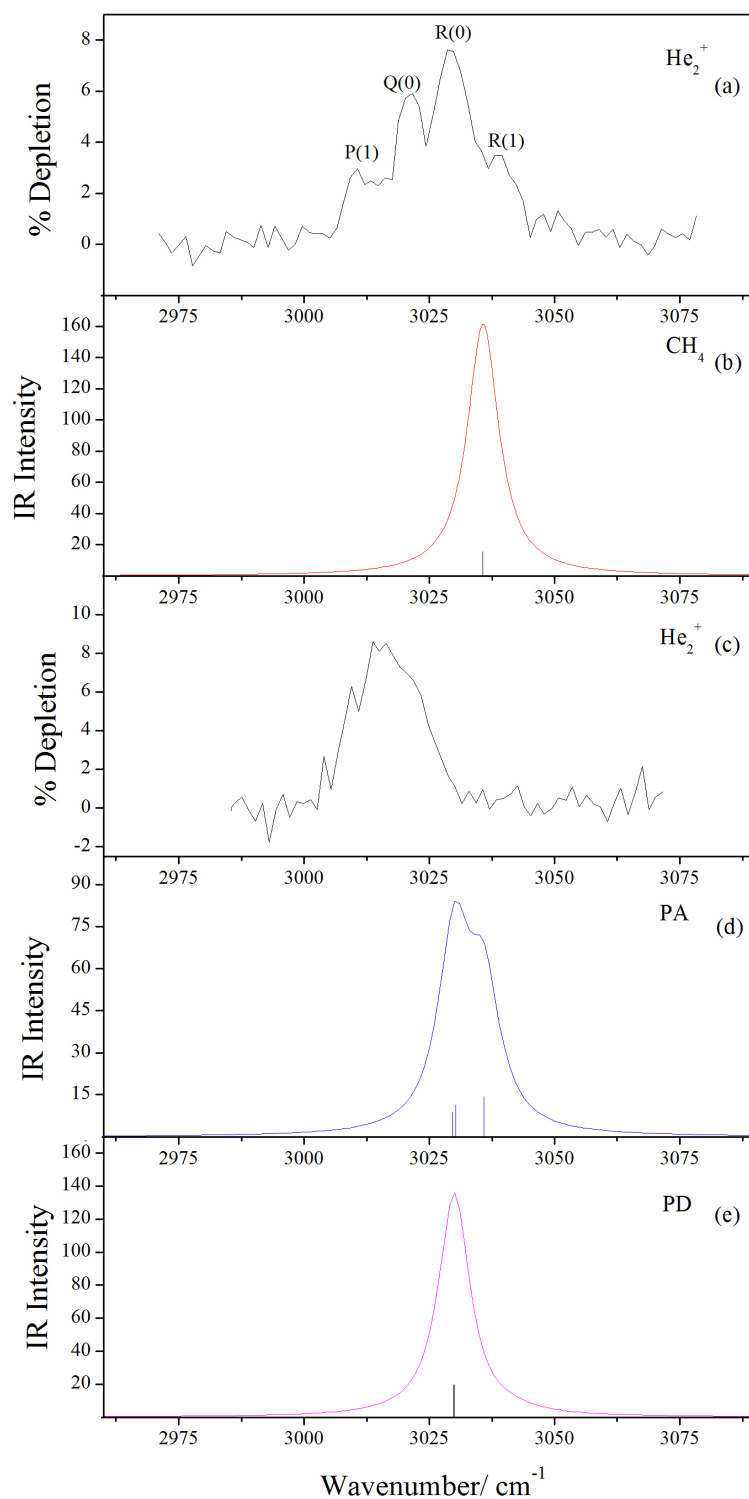
Figure 6.10. Comparison of (a) the experimental IR spectrum for pure methane and (b) the MP2 prediction for CH_4, (c) the CH_4 spectrum obtained with the addition of 3-5 water molecules. The partial pressure of methane was optimized for the pickup of a single methane molecule. Also shown in panels (d) and (e) are MP2 simulations for the proton acceptor and donor form, respectively. The same scaling factor as applied for Figure 6.7, namely 0.948, was applied here.
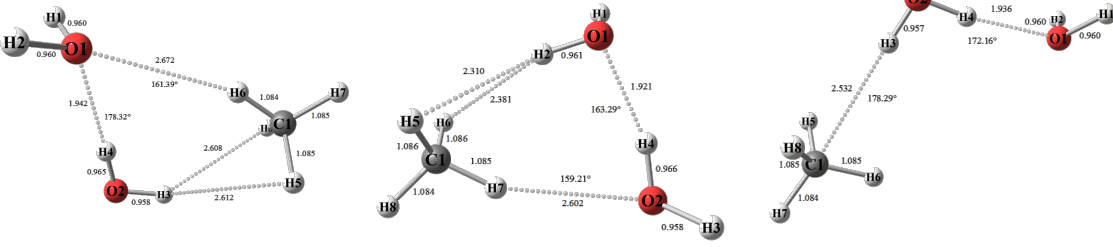
6.4.5. CH$_4$(H$_2$O)$_2$

Table 6.5 shows *ab initio* predictions for the CH$_4$(H$_2$O)$_2$ complex. Three potential energy minima were identified and are given the labels complex 1,2 and 3. Complexes 1 and 2 match two of the complexes reported previously by Kryachko *et al.*[16] Complex 3 differs from the third structure reported by Kryachko *et al.* in that it is an open chain structure in which the methane is linked to one of the water molecules in the water dimer by the CH$_4$ acting as a proton acceptor. In the work reported by Kryachko *et al.* a similar structure was reported with the difference being the methane acts as a proton donor. The other two complexes are cyclic species and the CH$_4$ can be described as acting as both a proton acceptor and donor. Complex 2 is the more compact cyclic structure and has the lowest energy of all the complexes, 183 cm^{-1} below complex 3 and 238 cm^{-1} below complex 1. At the very low temperature of the helium droplet complex 2 would be expected to be the sole constituent if energetics alone governed the outcome. However previous studies have shown that long-range electrostatic forces between the dopants can steer and orientate the dopants such that the molecules form metastable aggregates. Once a certain structure has formed, it is unlikely that rearrangements will be possible at the very low temperature of the droplet. Consequently, the exclusive formation of complex 2 in helium droplets cannot be determined by energetics alone.

Figure 6.11 shows a comparison of infrared spectra recorded in the region of the OH stretching vibrations, with and without methane. The spectra were recorded for the *m/z* 19 channel and the pickup of methane was optimised so that contributions from larger (CH$_4$)$_m$ for $m \geq 1$ were minimised. The pickup of water was optimized so that at least 5 water molecules were added into the droplets.

Table 6.5 Geometries of the three structures calculated for $CH_4(H_2O)_2$ optimized at the MP2/aug-cc-pVTZ level. The relative energies shown (in cm^{-1}) include the zero point energy.

	Complex 1 +183 cm^{-1}	Complex 2 0 cm^{-1}	Complex 3 +238 cm^{-1}
	Complex 1	**Complex 2**	**Complex 3**
r(H6···O1)	2.672 Å	2.602 Å	2.532 Å r(H7···O2)
∠C1H6O1	161.39°	159.21° ∠C1H7O2	178.29° ∠C1H3O2
r(H4···O1)	1.942 Å	1.921 Å	1.935 Å
∠O2H4O1	178.32°	163.29°	172.16°
τH6O1H2H1	-160.682°	85.98° τH7O2H4H3	0.00° τC1H3O2H4
τH4O1H2H1	124.39°	120.75°	117.76°

From a comparison of the methane-water spectrum shown in panel 6.11(c) to the pure water spectrum shown in 6.11(a) there are some observable differences. The first is the appearance of a new band to the red of the BD band of $(H_2O)_2$, which is assigned to the BD band of $CH_4(H_2O)_2$ for reasons discussed below. Secondly a broadening of the BD band assigned to H_2O_3 is also observed, which is presumably due to contributions from the BD band of $CH_4(H_2O)_3$.
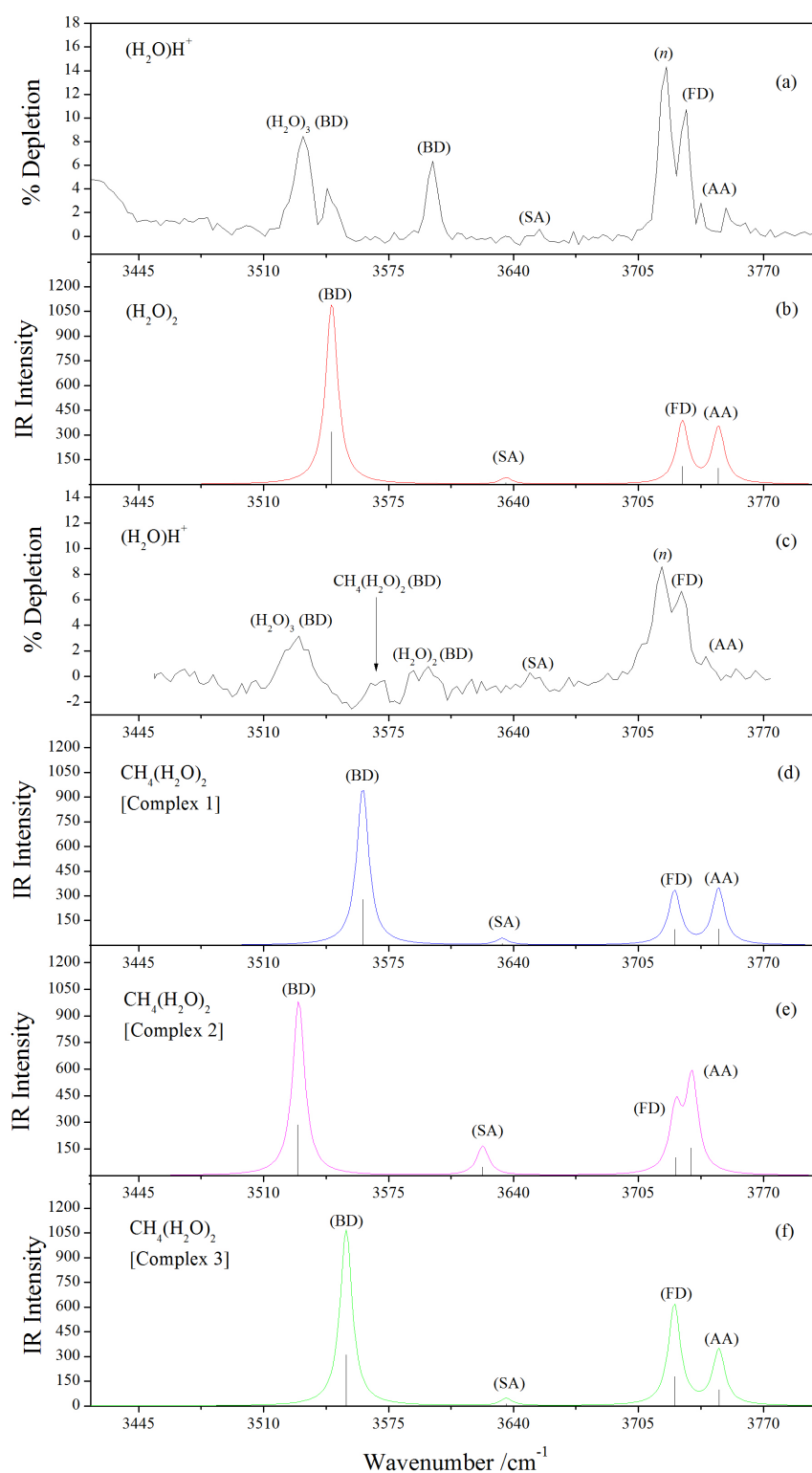
Figure 6.11. Comparison of (a) the experimental IR spectrum for pure water clusters, (b) the MP2 prediction for $(H_2O)_2$, and (c) the experimental spectrum obtained with the addition of a small quantity of methane. The partial pressure of methane was optimized for the pickup of a single methane molecule. Also shown in panels (d)-(f) are MP2 simulations for the three different calculated structures of $CH_4(H_2O)_2$. The same scaling factor as applied for Figure 6.7, namely 0.948, was applied here.

150

Simulated IR spectra for the predicted complexes 1-3 are shown in panels (d)-(f), respectively, and a list of the experimental and theoretical O-H stretching frequencies is shown in Table 6.6.

Table 6.6 Experimental and theoretical O-H stretching frequencies (cm^{-1}) for $(H_2O)_2$ and $CH_4(H_2O)_2$.

Band	(H₂O)₂		CH₄(H₂O)₂			
	Expt	Theory	Expt	Theory Complex 1	Theory Complex 2	Theory Complex 3
AA		3746		3747	3732	3747
FD	3729.3	3728	3727.4	3724	3724	3724
SA		3636		3634	3624	3636
BD	3597.7	3545	3568	3561	3527	3553

Complexes 1 and 3 do not match the experimental data for two reasons. The first is that the relatively strong AA bands predicted to the blue of the FD band are not observed in the spectrum. The other reason is that the calculations predict that the BD band will be blue shifted relative to $(H_2O)_2$, whereas the experimental spectrum only shows a new band that is red shifted by 26 cm^{-1} relative to the BD band of $(H_2O)_2$. However, the predicted OH stretches of complex 2 are in reasonably good agreement with the experimental values as the BD band is red shifted by a calculated 18 cm^{-1} relative to $(H_2O)_2$. Consequently, the band observed at 3568 cm^{-1} can be confidently assigned to the cyclic complex (complex 2) of $CH_4(H_2O)_2$. Since there is no evidence in the experimental spectrum for the blue shifted BD bands of complexes 1 and 3, it suggests that these complexes are not formed within the droplets.

It should also be mentioned that the predicted O-H stretching vibrations of the AA and FD bands in complex 2 are close together and are unlikely to be resolved at the

current resolution. However, the bands labelled n and FD in the mixed water methane spectrum (panel (c)) are much broader than they are in the pure water spectrum (panel (a)), which could be caused by a broadening of the FD and AA bands of $CH_4(H_2O)_2$ as predicted by the calculations.

Figure 6.12 shows a comparison of experimental and predicted infrared spectra recorded in the C-H stretching region using the same pickup conditions used for the spectra shown in Figure 6.11. In the O-H stretching region the BD and FD bands are well separated, which helps in the assignment of bands from various $CH_4(H_2O)_n$ complexes. However in the C-H stretching region the assignment of bands arising from different cluster sizes is difficult with the current spectral resolution. Consequently, if the spectrum were to be recorded at a higher resolution it might be possible to resolve individual bands. Panels 6.12(d)-(f) show the predicted spectra from the MP2 calculations of the $CH_4(H_2O)_2$ complexes 1-3, respectively. Although the experimental spectrum in panel 6.12(c) might contain contributions from various $CH_4(H_2O)_n$ cluster sizes, the simulated spectrum of complex 2 is in reasonably good agreement with the experimental spectrum, which is predicted to exhibit a significant red-shift relative to free CH_4 when compared to complexes 1 and 3.
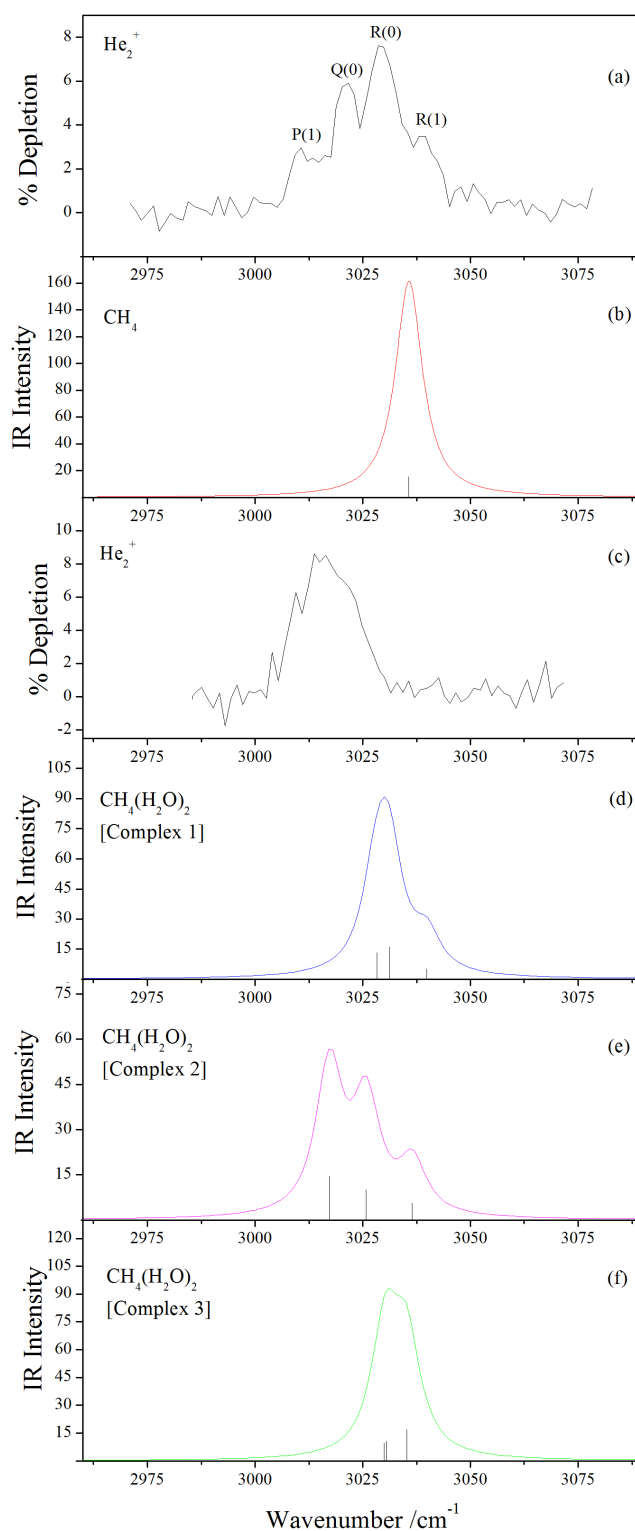
Figure 6.12. Comparison of (a) the experimental IR spectrum for pure methane, (b) the MP2 prediction for CH_4, (c) the experimental spectrum obtained with the addition of 3-5 water molecules (c). The partial pressure of methane was optimized for the pickup of a single methane molecule. Also shown in panels (d)-(f) are MP2 simulations for the three different complexes of $CH_4(H_2O)_2$. The same scaling factor as applied for Figure 6.7, namely 0.948, was applied here.

6.4.6. CH₄(H₂O)₃

Table 6.7 shows the *ab initio* predictions for two structures of the water-methane trimer, $CH_4(H_2O)_3$. The results presented here are only preliminary studies of the water trimer and whilst only two structures are considered here there may be other stable structures, which we have not managed to locate. The starting structures used consisted of a methane molecule attached to side, surface and to one of the three free OH bonds of the water trimer. The calculation where the methane molecule was attached to the side of the water trimer did not converge and tended to orientate the methane molecule into a position above the centre of the water trimer ring. Of the starting structures used only two potential energy minima were identified and have been named complex 1 and complex 2. Complex 1 consists of a methane molecule residing above centre of a water trimer ring and can be thought of as both a proton acceptor and donor. Complex 2 consists of a methane molecule acting as a proton accepter to a specific water molecule in the water ring. Complex 1 has the lowest energy of the two structures and at the very low temperature of the helium droplet complex 1 would be expected to be the sole constituent, if energetics alone governed the outcome.

Figure 6.13 shows a comparison of infrared spectra recorded in the region of the O-H stretch vibrations with and without methane. The experimental spectra are the same as those shown in panels (a) and (c) of Figure 6.11 and the predicted spectra for complex 2 and 1 of the water trimer are shown in panels (d) and (e) respectively. Following the addition of methane the BD and FD bands associated with the water trimer become broader, which makes assignment of the transitions difficult. Both of the predicted structures for the water trimer predict a similar broadening of the BD bands, with complex 1 being slightly more red shifted than complex 2.

Table 6.7 Geometries of the two structures calculated for $CH_4(H_2O)_3$ optimized at the MP2/aug-cc-pVTZ level. The relative energies shown (in cm^{-1}) include the zero point energy.


	Complex 1	Complex 2
	0 cm^{-1}	+ 99 cm^{-1}

	Complex 1	Complex 2
r(H6⋯O1)	1.893 Å	1.888 Å
r(H8⋯O2)	1.857 Å	1.859 Å
r(H4⋯O3)	1.896 Å	1.895 Å
∠C10H11O1	134.97°	174.59° ∠C10H7O1
∠C10H12O3	135.32°	-0.015° τH8O2O1O3
∠H13C10H7	170.12°	0.429° τH8O1O3O2

For the $CH_4(H_2O)_3$ FD band (labelled as *n* in panel (c) of Figure 6.13) the calculations predict a slight broadening and red shift of the band, which cannot be resolved at the current spectral resolution.
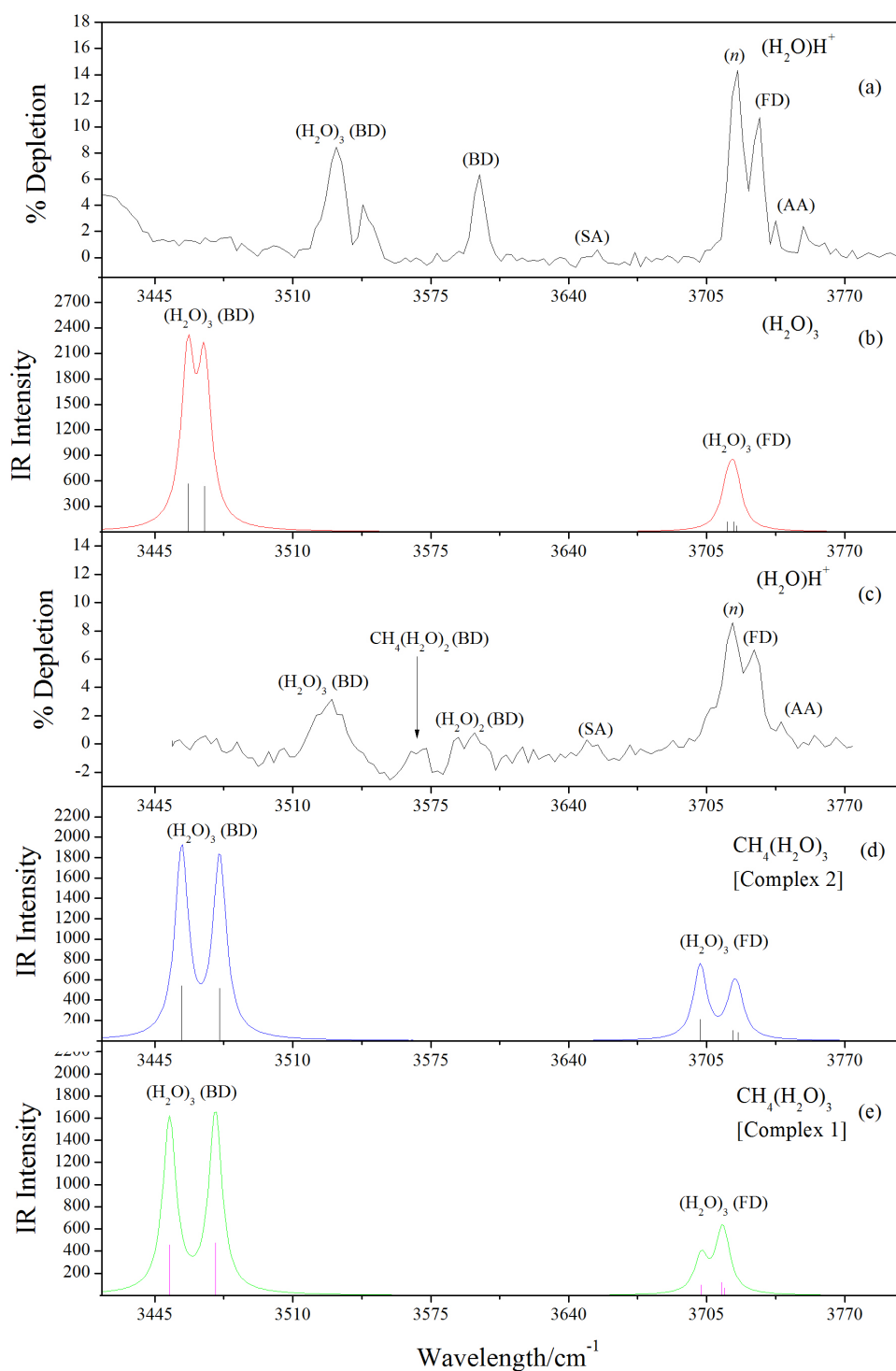
Figure 6.13. Comparison of (a) the experimental IR spectrum for pure water clusters, (b) the MP2 prediction for $(H_2O)_3$ and (c) the experimental spectrum obtained with the addition of a small quantity of methane. The partial pressure of methane was optimized for the pickup of a single methane molecule. Also shown in panels (d) and (e) are MP2 simulations for complexes 2 and 1 of $CH_4(H_2O)_3$, respectively. The same scaling factor as applied for Figure 6.7, namely 0.948, was applied here.

Figure 6.14 shows a comparison of infrared spectra recorded in the region of the C-H stretch vibrations with and without methane. As described previously the assignments of bands in this region cannot be made at the current resolution. However on comparison of the simulated spectra, complex 1 is in reasonably good agreement with the experimental spectrum, as it predicts a broader band for the C-H stretch vibrations when compared to complex 2. In support of complex 1 the methane molecule resides on the surface of the water trimer, which is in agreement with the predicted structures of $CH_4(H_2O)_n$ reported by Ruckenstien *et al.*[15]
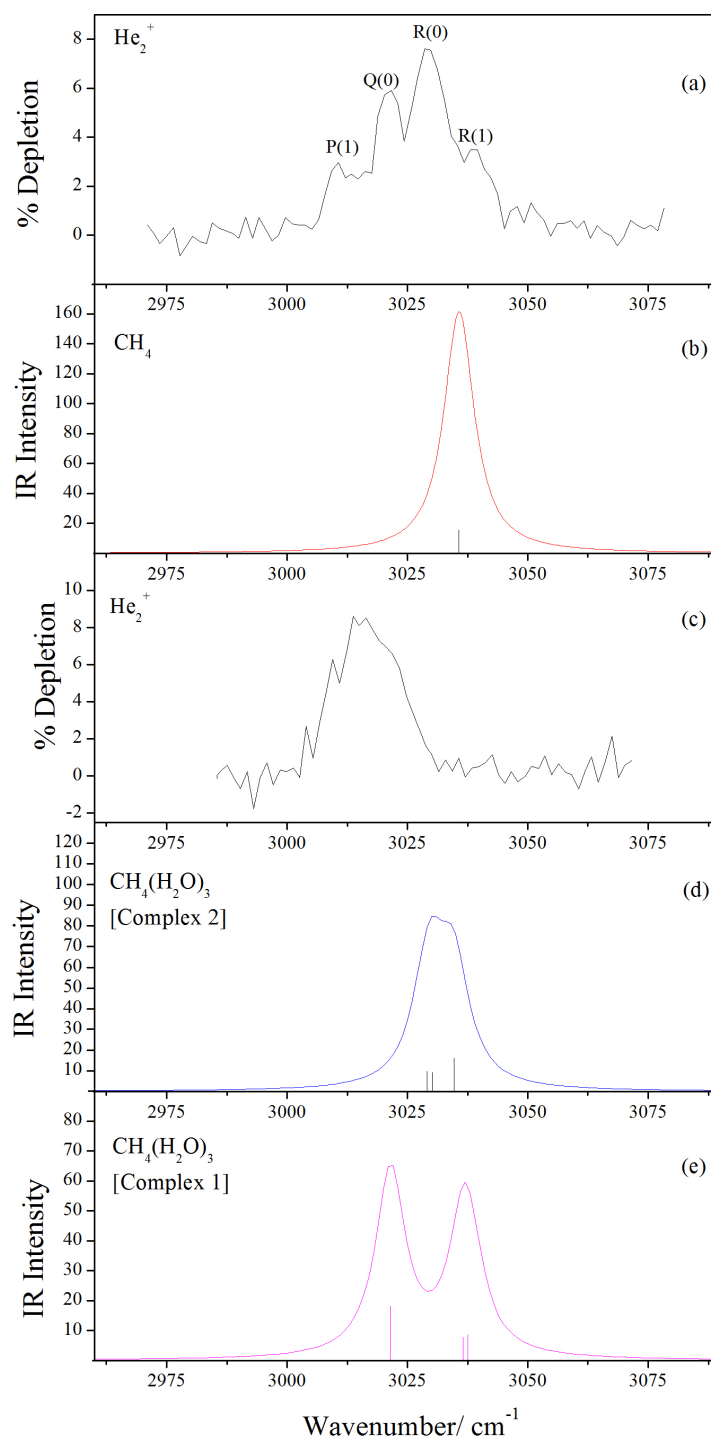
Figure 6.14. Comparison of (a) the experimental IR spectrum for pure methane, (b) the MP2 prediction for CH_4, and (c) the experimental spectrum obtained with the addition of 3-5 water molecules. The partial pressure of methane was optimized for the pickup of a single methane molecule. Also shown in panels (d) and (e) are MP2 simulations for complexes 2 and 1 of $CH_4(H_2O)_3$, respectively. The same scaling factor as applied for Figure 6.7, namely 0.948, was applied here.

6.5. SUMMARY

The results from infrared spectra recorded for pure water and mixed $CH_4(H_2O)_n$ clusters, for n = 1-3, in helium droplets have been interpreted with the use of *ab initio* calculations. The main differences between the experimental spectra recorded with and without methane are that the bands associated with free O-H stretches and the bonding O-H stretches became broader and a new feature was observed around 3568 cm^{-1}. From a comparison of the predicted vibrational frequencies of three structures of $CH_4(H_2O)_2$ the new band was assigned to the bonding O-H stretch of the water dimer in complex 2 of $CH_4(H_2O)_2$. Unfortunately with the current resolution bands associated with $CH_4(H_2O)$ and $CH_4(H_2O)_3$ could not be confidently assigned. The broadening of the $(H_2O)_3$ (BD) and $(H_2O)_3$ (FD) bands is presumably due to contributions from $CH_4(H_2O)_3$, but a complete *ab initio* study of this complex is required before a complete analysis of its structure can be made. However, based on energetics it is predicted that the water methane dimer will exist in its proton donor form and the $CH_4(H_2O)_3$ will likely form a structure where the methane resides at the surface of the water trimer.

Spectra recorded in the C-H region showed a significant red-shift of the ν_3 band following the addition of water. A similar red-shift of the ν_3 band was also predicted in the *ab initio* calculations for the $CH_4(H_2O)_n$ complexes. A significant red-shift was observed for complex 2 of $CH_4(H_2O)_2$, which was taken to confirm the presence of this complex within the droplets. At the current resolution precise assignments of the bands could not be made and the broadening of the bands is presumably due to the superposition of peaks corresponding to various $CH_4(H_2O)_n$ cluster sizes. Consequently, a further study recorded at a higher resolution is necessary to identify the $CH_4(H_2O)_n$ complexes.

REFERENCES FOR CHAPTER 6

1. S. Goyal, D. L. Schutt, G. Scholes, *Phys. Rev. Lett.*, 1992, **69**, 933.

2. J. P. Toennies, A. F. Vilesov, *Annu. Rev. Phys. Chem.,* 1998, **49**, 1.

3. J. P. Toennies, A. F. Vilesov, *Angew. Chem. Inst. Ed*. 2004, **43**, 2622.

4. M. Hartmann, R. E. Miller, J. P. Toennies, A. F. Vilesov, *Phys. Rev. Lett.*, 1995, **75**, 1566.

5. K. Nauta, R. E. Miller, *Science*, 2000, **287**, 293.

6. K. Nauta, R. E. Miller, *Science*, 1999, **283**, 1895.

7. S. Kuma, M. N. Slipchenko, K. E. Kuyanov, T. Momose, A. F. Vilesov, *J. Phys. Chem. A*, 2006, **110**, 10046.

8. S. Kuma, M. N. Slipchenko, T. Momose, A. F. Vilesov, *J.Phys. Chem. A*, 2010, **114**, 9022.

9. A. Vysniauska, P. R. Bishnoi, *Chem. Eng. Sci.*, 1983, **38**, 1061.

10. A.M. Davis, S. J. Teague, *Angew. Chemie Int. Ed.*, 1999, **38**, 736.

11. L. Dore, R. C. Cohen, C. A. Schmuttenmaer, K. L. Busarow, M. J. Elrod, J. G. Loeser, R. J. Saykally, *J. Chem. Phys.*, 1994, **100**, 863.

12. M. M. Szczesniak, G. Chalasinski, S. M, Cybulski, P. Cieplak, *J. Chem. Phys.*, 1993, **98**, 3078.

13. B. Raghavendra, E. Arunan, *Chem. Phys. Lett.*, 2008, **467**, 37.

14. K. L. Kopeland, G. S. Tschumper, *J. Chem. Theory Comput.*, 2012, **8**, 1646.

15. E. Ruckenstein, I. L. Shulgin, J. L. Tilson, *J. Phys. Chem. A*, 2003, **107**, 2289.

16. E. S. Kryachko, T. Zeegers-Huyskens, *J. Phys. Chem. A*, 2003, **107**, 7546.

17. M. J. Frisch *et al*., Gaussian 03, ReVision C.02; Gaussian, Inc.: Wallingford, CT, 2004.

18. A. V. Kanaev, L. Museur, T. Laarman, M. C. Castex, S. Monticone, K. von Haeften and T. Möller, *J. Chem. Phys.*, 2001, **115**, 10248.

19. K. Kuyanov-Prozument, M. Y. Choi, A. F. Vilesov, *J. Chem. Phys*., 2010, **132**, 014304.

20. F. Huisken, M. Kaloudis, A. Kulcke, *J. Chem. Phys*., 1996, **104**, 17.

21. R. Fröchtenicht, M. Kaloudis, M. Koch, F. Huisken, *J. Chem. Phys.*, 1996, **105**, 6128.

22. K. Kuyanov-Prozument, M. Y. Choi, A. F. Vilesov, *J. Chem. Phys*., 2010, **132**, 014304.

23. B. Tremblay, B. Madebène, M. E. Alikhani, J. P. Perchard, *Chem. Phys*., 2010, **378**, 27.

24. K. Nauta, R. E. Miller, *Chem. Phys. Lett.*, 2001, **350**, 225.

25. K. E. Kuyanov, M. N. Slipchenko, A. F. Vilesov, *Chem. Phys. Lett.*, 2006, **427**, 5.

This section includes additional information for Chapter 4. The mass spectra recorded for water clusters co-added with Ar, N_2, O_2, CO_2, C_6D_6, NO and CO are shown in Figures A.1-7 respectively. Figures A. 8-13 show the geometries of the calculated structures for the $[X(H_2O)_2]^+$ where X = Ar, N_2, CO_2 and CO.
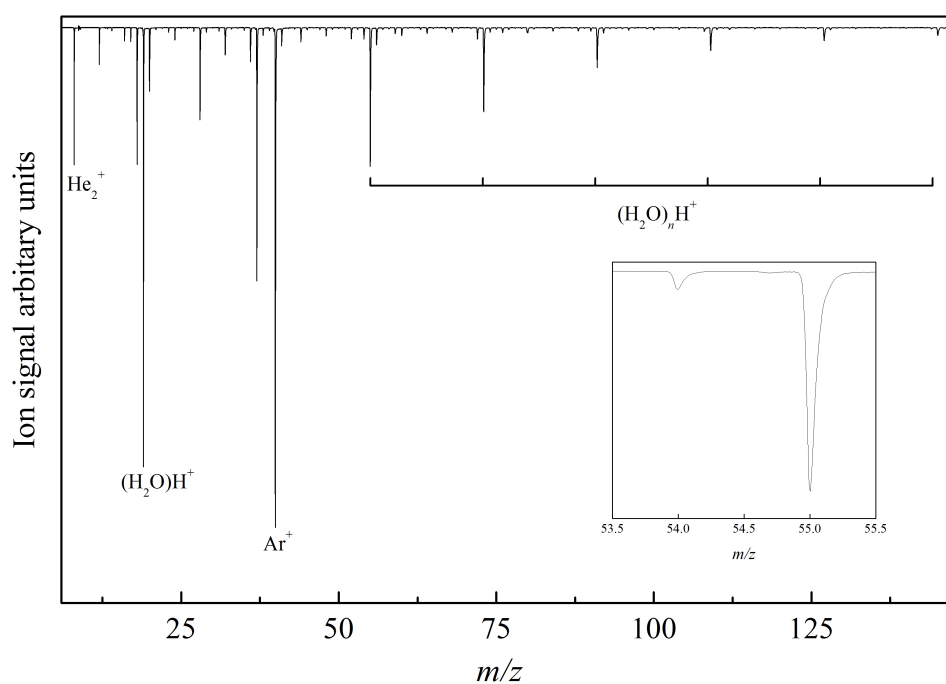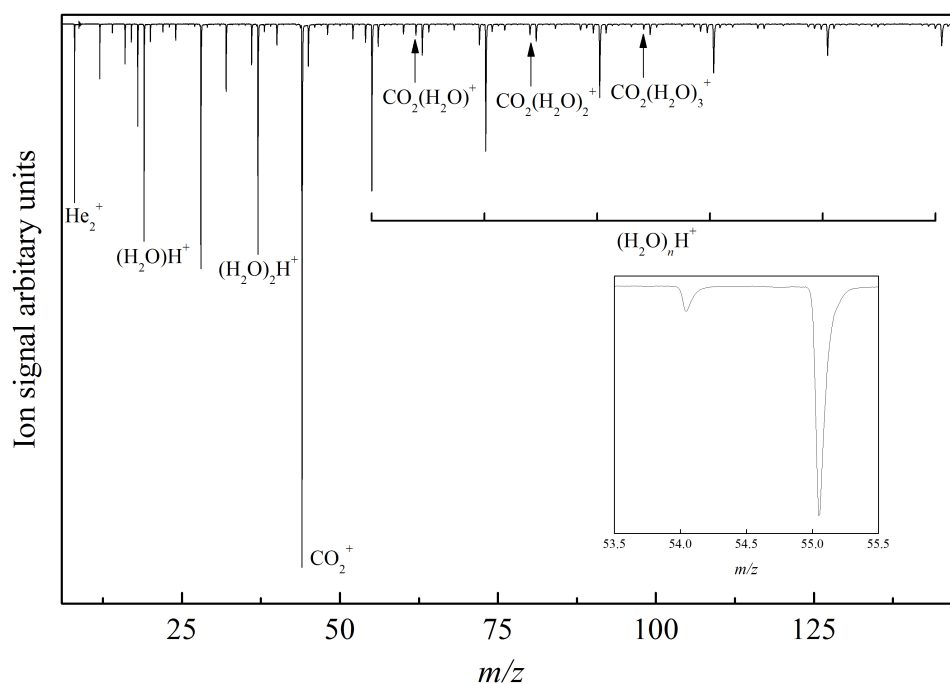

Figure A.1 Electron impact mass spectrum of helium droplets doped with water and Ar. Pure water cluster ions $((H_2O)_n^+$ and $(H_2O)_nH^+)$ and peaks corresponding to binary cluster ions, consisting of Ar and water $(Ar-(H_2O)_n^+)$, are observed in the spectrum.
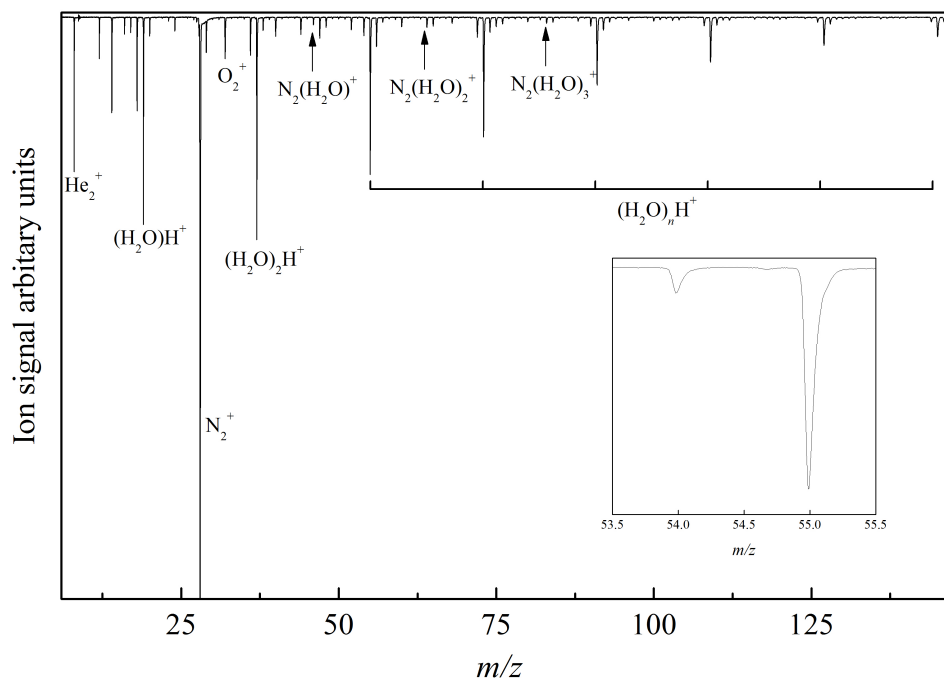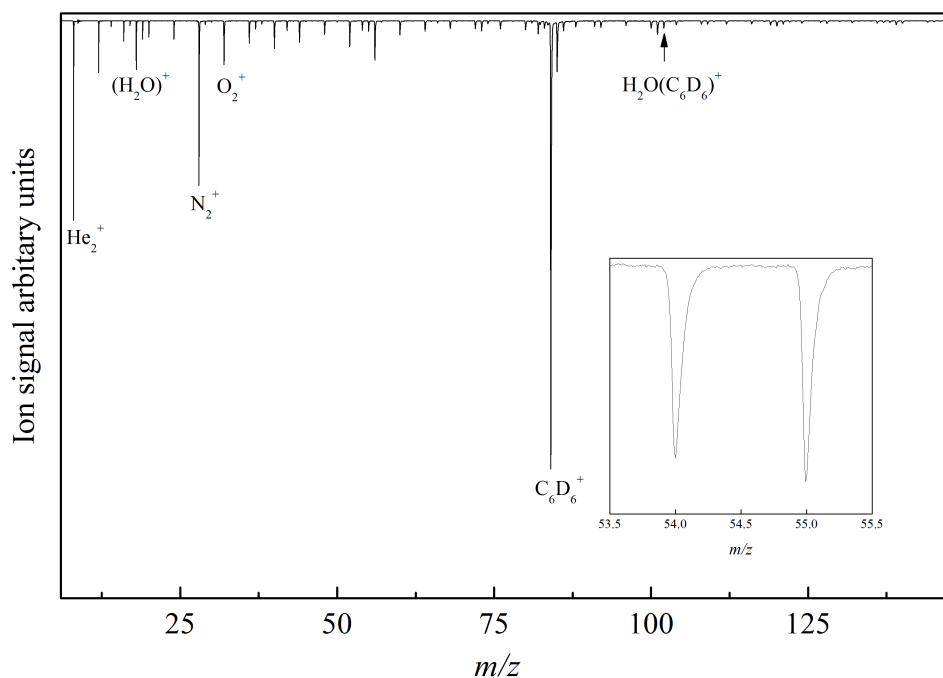
Figure A.2. Electron impact mass spectrum of helium droplets doped with water and N_2. Pure water cluster ions ($(H_2O)_n^+$ and $(H_2O)_nH^+$) and peaks corresponding to binary cluster ions, consisting of N_2 and water (N_2-$(H_2O)_n^+$), are observed in the spectrum.
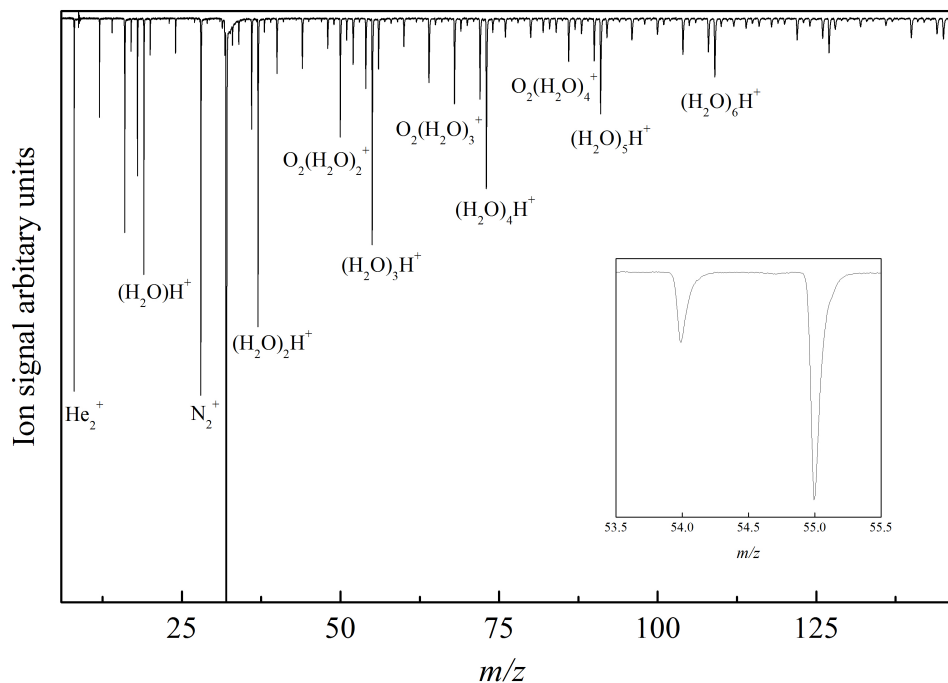
Figure A.3. Electron impact mass spectrum of helium droplets doped with water and O_2. Pure water cluster ions ($(H_2O)_n^+$ and $(H_2O)_nH^+$) and peaks corresponding to binary cluster ions, consisting of O_2 and water (O_2-$(H_2O)_n^+$), are observed in the spectrum.
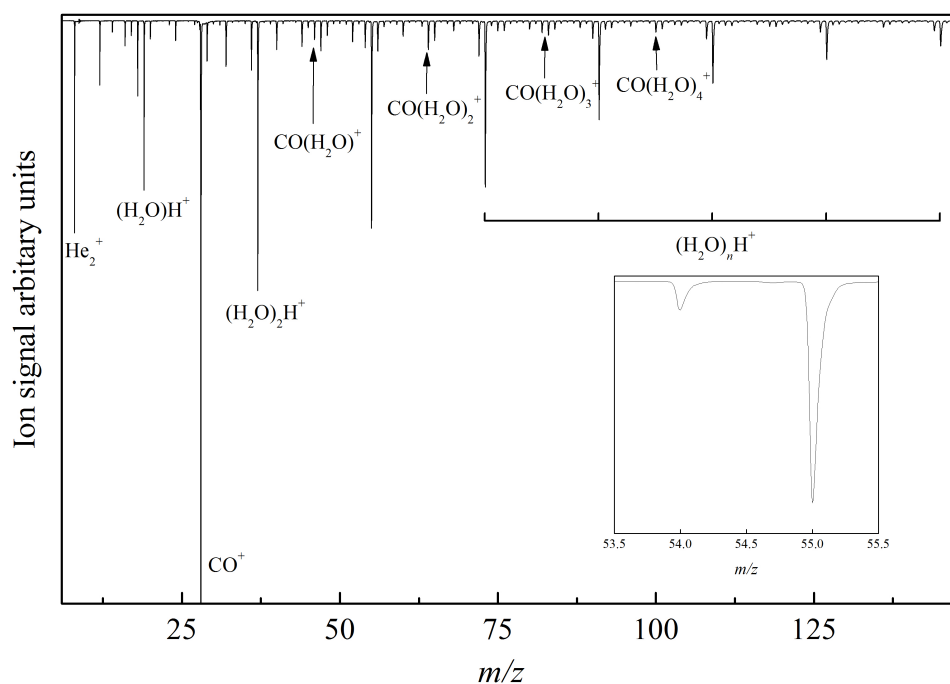
Figure A.4. Electron impact mass spectrum of helium droplets doped with water and CO_2. Pure water cluster ions ($(H_2O)_n^+$ and $(H_2O)_nH^+$) and peaks corresponding to binary cluster ions, consisting of CO_2 and water (CO_2-$(H_2O)_n^+$), are observed in the spectrum.

Figure A.5. Electron impact mass spectrum of helium droplets doped with water and C_6D_6. Pure water cluster ions ($(H_2O)_n^+$ and $(H_2O)_nH^+$) and peaks corresponding to binary cluster ions, consisting of C_6D_6 and water (C_6D_6-$(H_2O)_n^+$), are observed in the spectrum.
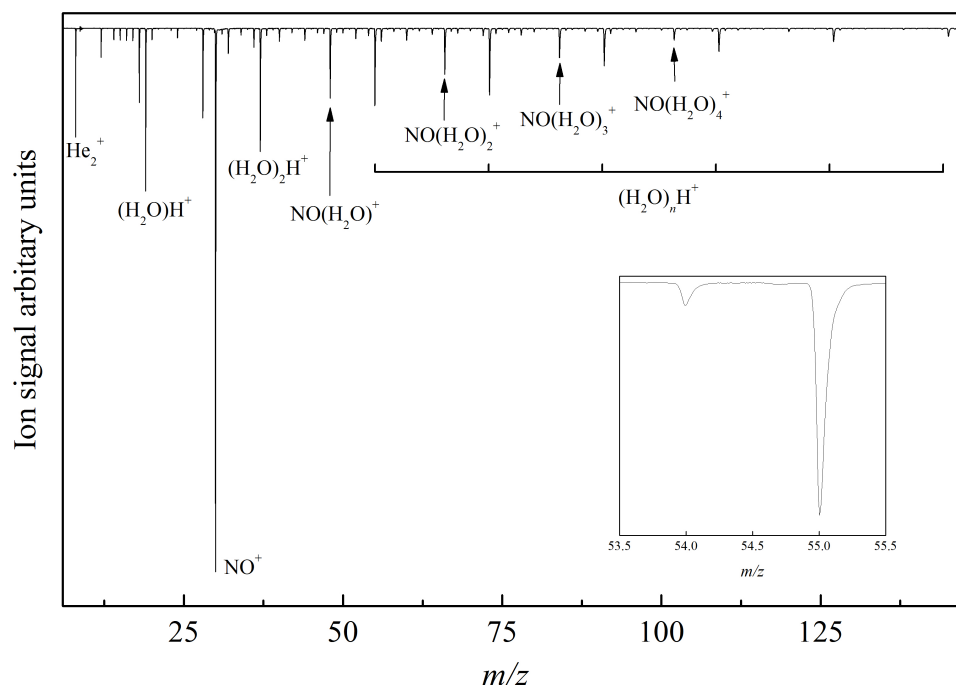
Figure A.6. Electron impact mass spectrum of helium droplets doped with water and CO. Pure water cluster ions (($H_2O)_n^+$ and $(H_2O)_nH^+$) and peaks corresponding to binary cluster ions, consisting of CO and water (CO-$(H_2O)_n^+$), are observed in the spectrum.


Figure A.7. Electron impact mass spectrum of helium droplets doped with water and NO. Pure water cluster ions (($H_2O)_n^+$ and $(H_2O)_nH^+$) and peaks corresponding to binary cluster ions, consisting of NO and water (NO-$(H_2O)_n^+$), are observed in the spectrum.
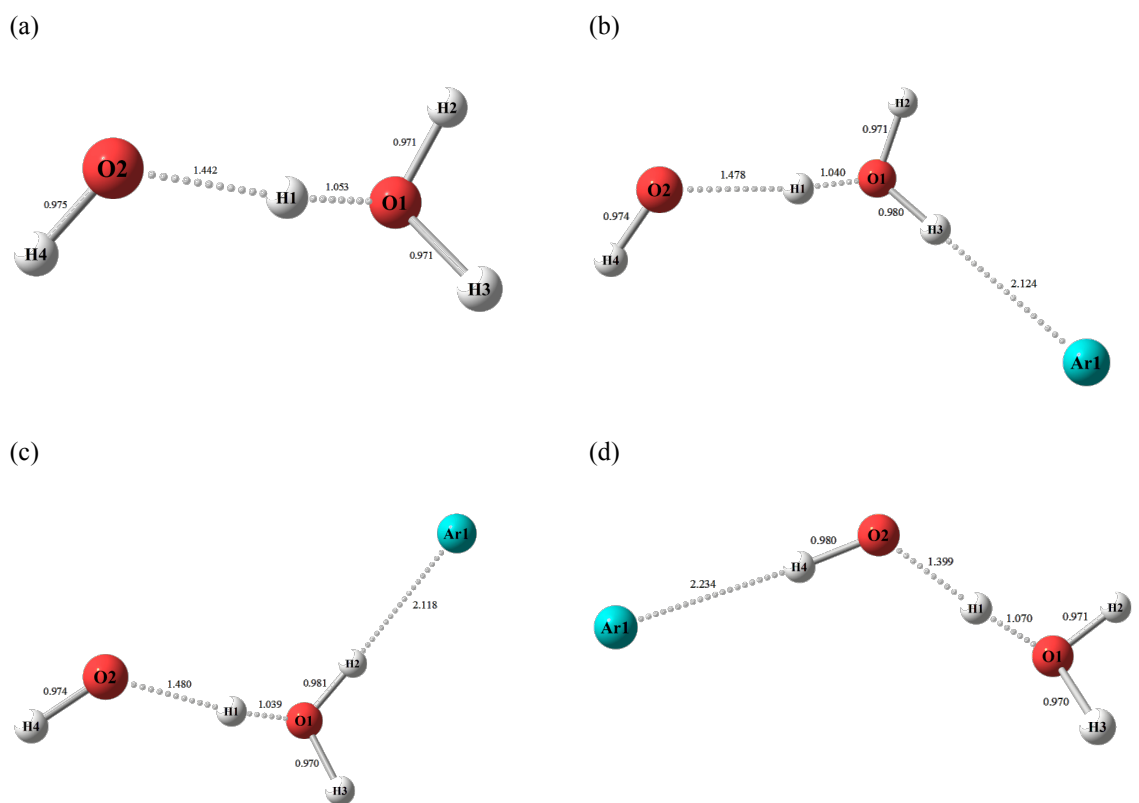
|	HO$\cdots$HOH$_2^+$	cis-(H$_2$O$_2$)$^+$Ar	trans-(H$_2$O$_2$)$^+$Ar	Ar$\cdots$(H$_2$O$_2$)$^+$
r(H4$\cdots$O2)	0.975 Å	0.974 Å	0.974 Å	0.980 Å
r(H1$\cdots$O2)	1.442 Å	1.478 Å	1.480 Å	1.399 Å
r(H1$\cdots$O1)	1.053 Å	1.040 Å	1.039 Å	1.070 Å
r(H2$\cdots$O1)	0.971 Å	0.971 Å	0.981 Å	0.971 Å
r(H3$\cdots$O1)	0.971 Å	0.980 Å	0.970 Å	0.970 Å
r(H3$\cdots$Ar1)	-	2.124 Å	2.118 Å r(H2$\cdots$Ar1)	2.234 Å r(H4$\cdots$Ar1)
$\angle$O2H1O1	172.81°	173.10°	172.56°	172.85°
$\angle$O1H3Ar1	-	176.5°	176.29° $\angle$O1H2Ar1	176.17° $\angle$O2H4Ar1
$\angle$H2O1H3	110.09°	110.35°	110.4°	109.85°

Figure A.8. Optimised geometries for (a) HO$\cdots$HOH$_2^+$; (b) cis-(H$_2$O$_2$)$^+$Ar; (c) trans-(H$_2$O$_2$)$^+$Ar; and (d) Ar$\cdots$(H$_2$O$_2$)$^+$. The *trans*-geometry of [Ar(H$_2$O)$_2$]$^+$, shown in (c), is the global minimum.

(a)

(b)

(c)
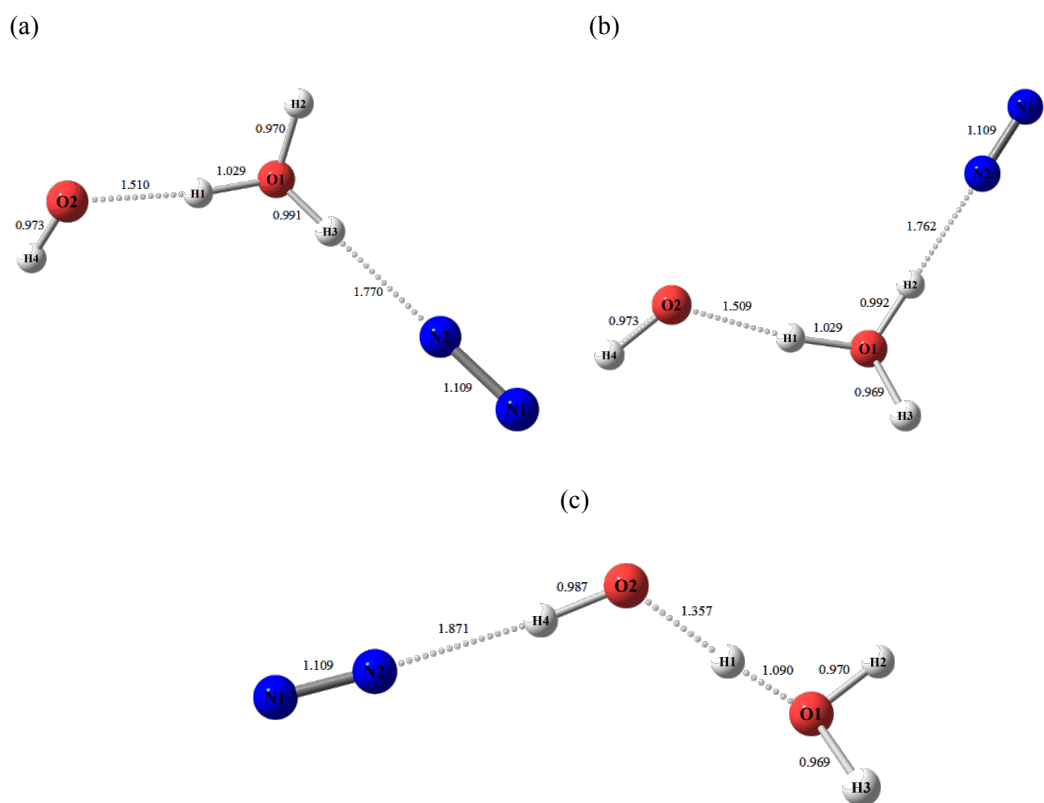
	cis-$(H_2O_2)^+N_2$	trans-$(H_2O_2)^+N_2$	$N_2\cdots(H_2O_2)^+$
r(H4$\cdots$O2)	0.973 Å	0.973 Å	0.987 Å
r(H1$\cdots$O2)	1.510 Å	1.509 Å	1.357 Å
r(H1$\cdots$O1)	1.029 Å	1.029 Å	1.090 Å
r(H2$\cdots$O1)	0.970 Å	0.992 Å	0.970 Å
r(H3$\cdots$O1)	0.991 Å	0.969 Å	0.969 Å
r(H3$\cdots$N2)	1.770 Å	1.762 Å r(H2$\cdots$N2)	1.871 Å r(H4$\cdots$N2)
∠O2H1O1	173.38°	172.12°	173.10°
∠O1H3N2	176.006°	176.19° ∠O1H2N2	174.84° ∠O2H4N2
∠H2O1H3	110.84°	111.08°	109.57°

Figure A.9. Optimised geometries for (a) cis-$(H_2O_2)^+N_2$; (b) trans-$(H_2O_2)^+N_2$; and (c) $N_2\cdots(H_2O_2)^+$. The *trans*-geometry of $[N_2(H_2O)_2]^+$, shown in (b), is the global minimum.

(a)

(b)

(c)
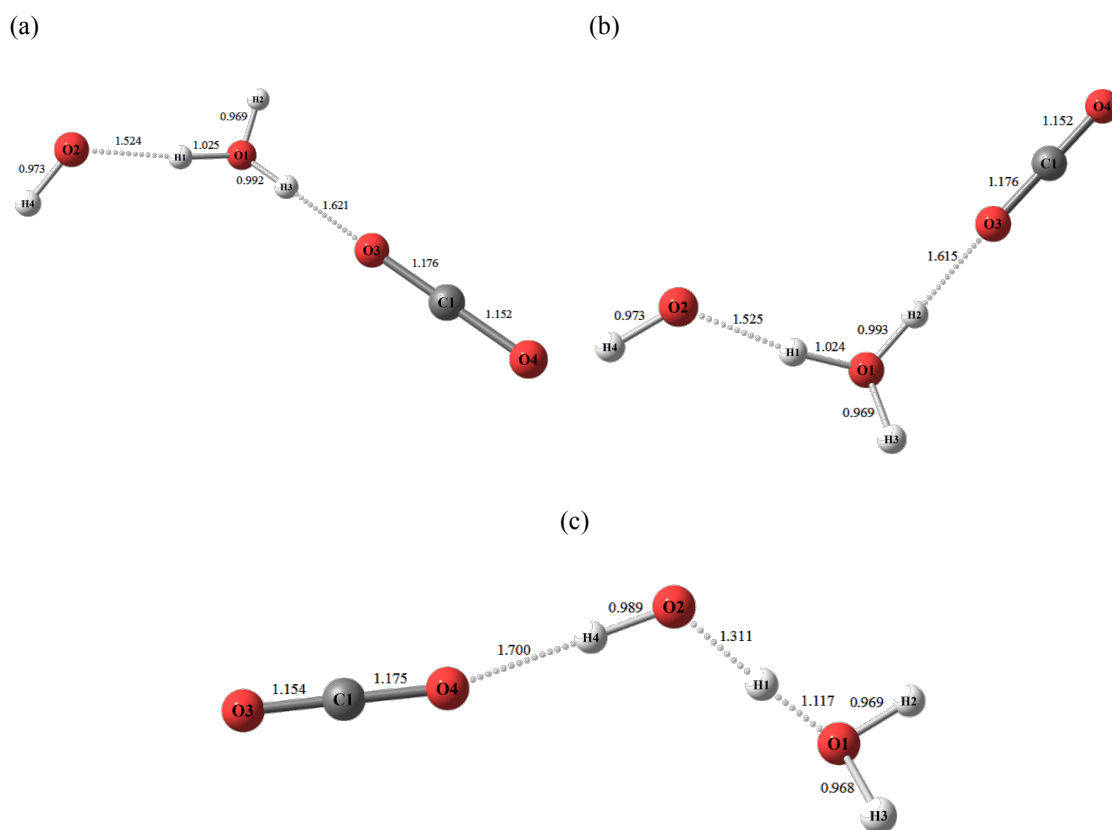
	cis-$(H_2O_2)^+CO_2$	trans-$(H_2O_2)^+CO_2$	$CO_2\cdots(H_2O_2)^+$
$r(H4\cdots O2)$	0.973 Å	0.973 Å	0.989 Å
$r(H1\cdots O2)$	1.524 Å	1.525 Å	1.311 Å
$r(H1\cdots O1)$	1.025 Å	1.024 Å	1.117 Å
$r(H2\cdots O1)$	0.969 Å	0.993 Å	0.969 Å
$r(H3\cdots O1)$	0.992 Å	0.969 Å	0.968 Å
$r(H3\cdots O3)$	1.621 Å	1.615 Å $r(H2\cdots O3)$	1.700 Å $r(H4\cdots O4)$
$\angle O2H1O1$	173.59°	172.16°	173.51°
$\angle O1H3O3$	178.45°	178.55° $\angle O1H2O3$	179.34° $\angle O2H4O4$
$\angle H2O1H3$	110.57°	110.71°	109.32°

Figure A.10. Optimised geometries for (a) cis-$(H_2O_2)^+CO_2$; (b) trans-$(H_2O_2)^+CO_2$; and (c) $CO_2\cdots(H_2O_2)^+$. The *trans*-geometry of $[CO_2(H_2O)_2]^+$, shown in (b), is the global minimum.

	cis-$(H_2O_2)^+OC$	trans-$(H_2O_2)^+OC$	$CO\cdots(H_2O_2)^+$
r(H4$\cdots$O2)	0.974 Å	0.973 Å	0.981 Å
r(H1$\cdots$O2)	1.495 Å	1.509 Å	1.379 Å
r(H1$\cdots$O1)	1.034 Å	1.029 Å	1.079 Å
r(H2$\cdots$O1)	0.970 Å	0.969 Å	0.970 Å
r(H3$\cdots$O1)	0.983 Å	0.992 Å	0.970 Å
r(H3$\cdots$O3)	1.746 Å	1.761 Å	1.847 Å r(H4$\cdots$O3)
∠O2H1O1	173.19°	172.06°	172.90°
∠O1H3O3	175.19°	176.14°	173.40° ∠O2H4O3
∠H2O1H3	110.64°	111.08°	109.73°
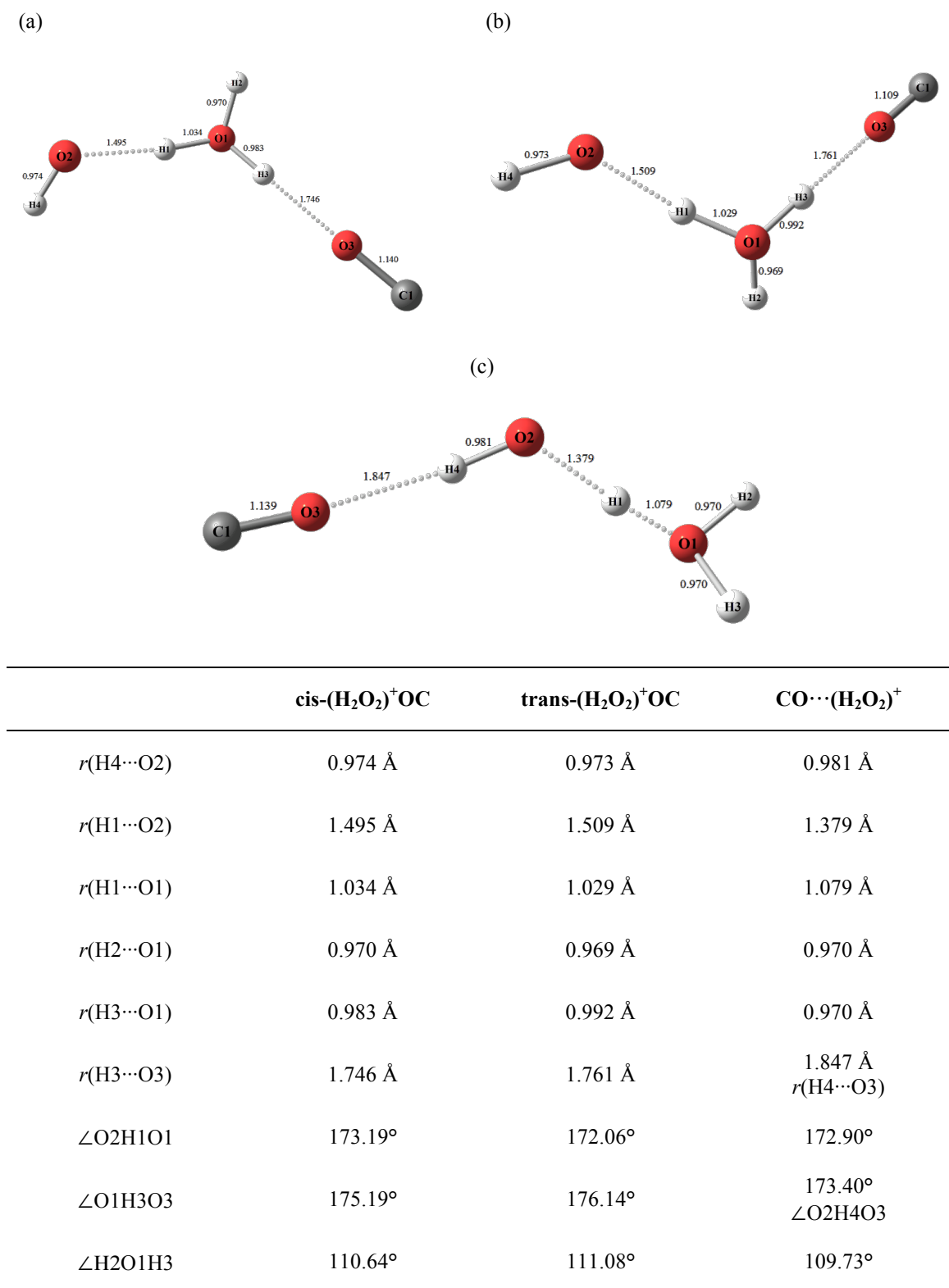
Figure A.11. Optimised geometries for (a) cis-$(H_2O_2)^+OC$; (b) trans-$(H_2O_2)^+OC$; and (c) $CO\cdots(H_2O_2)^+$.

	cis-$(H_2O_2)^+CO$	trans-$(H_2O_2)^+CO$	$OC \cdots (H_2O_2)^+$
$r(H4 \cdots O2)$	0.973 Å	0.973 Å	1.002 Å
$r(H1 \cdots O2)$	1.540 Å	1.540 Å	1.294 Å
$r(H1 \cdots O1)$	1.021 Å	1.020 Å	1.128 Å
$r(H2 \cdots O1)$	0.969 Å	0.969 Å	0.969 Å
$r(H3 \cdots O1)$	1.01 Å	1.012 Å	0.968 Å
$r(H3 \cdots C1)$	1.769 Å	1.758 Å	1.859 Å $r(H4 \cdots C1)$
$\angle O2H1O1$	173.77°	172.0°	173.639°
$\angle O1H3C1$	175.79°	176.31°	174.54° $\angle O2H4C1$
$\angle H2O1H3$	111.0°	111.38°	109.12°
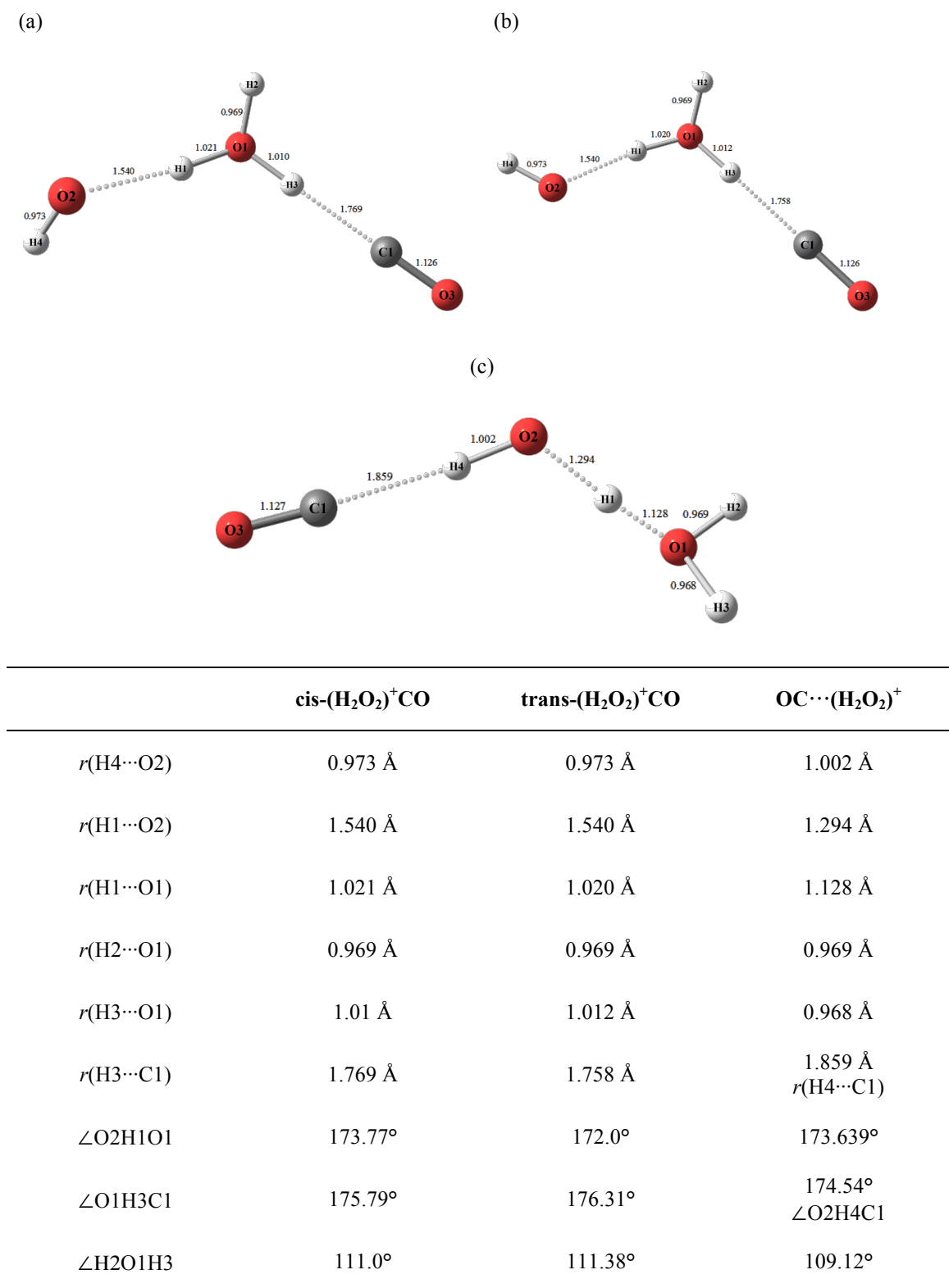
Figure A.12. Optimised geometries for (a) cis-$(H_2O_2)^+CO$; (b) trans-$(H_2O_2)^+CO$; and (c) $OC \cdots (H_2O_2)^+$.

(a)

(b)

	cis-HOCO⋯H$_3$O$^+$	*trans*-HOCO⋯H$_3$O$^+$
r(H4⋯O2)	0.976 Å	0.969 Å
r(H1⋯O2)	1.422 Å	1.483 Å
r(H1⋯O1)	1.052 Å	1.034 Å
r(H2⋯O1)	0.971 Å	0.973 Å
r(H3⋯O1)	0.971 Å	0.973 Å
r(O2⋯C1)	1.380 Å	1.376 Å
∠O2H1O1	173.77°	177.59°
τH4O2C1O3	0.0°	180.0°
∠H2O1H3	110.12°	109.79°
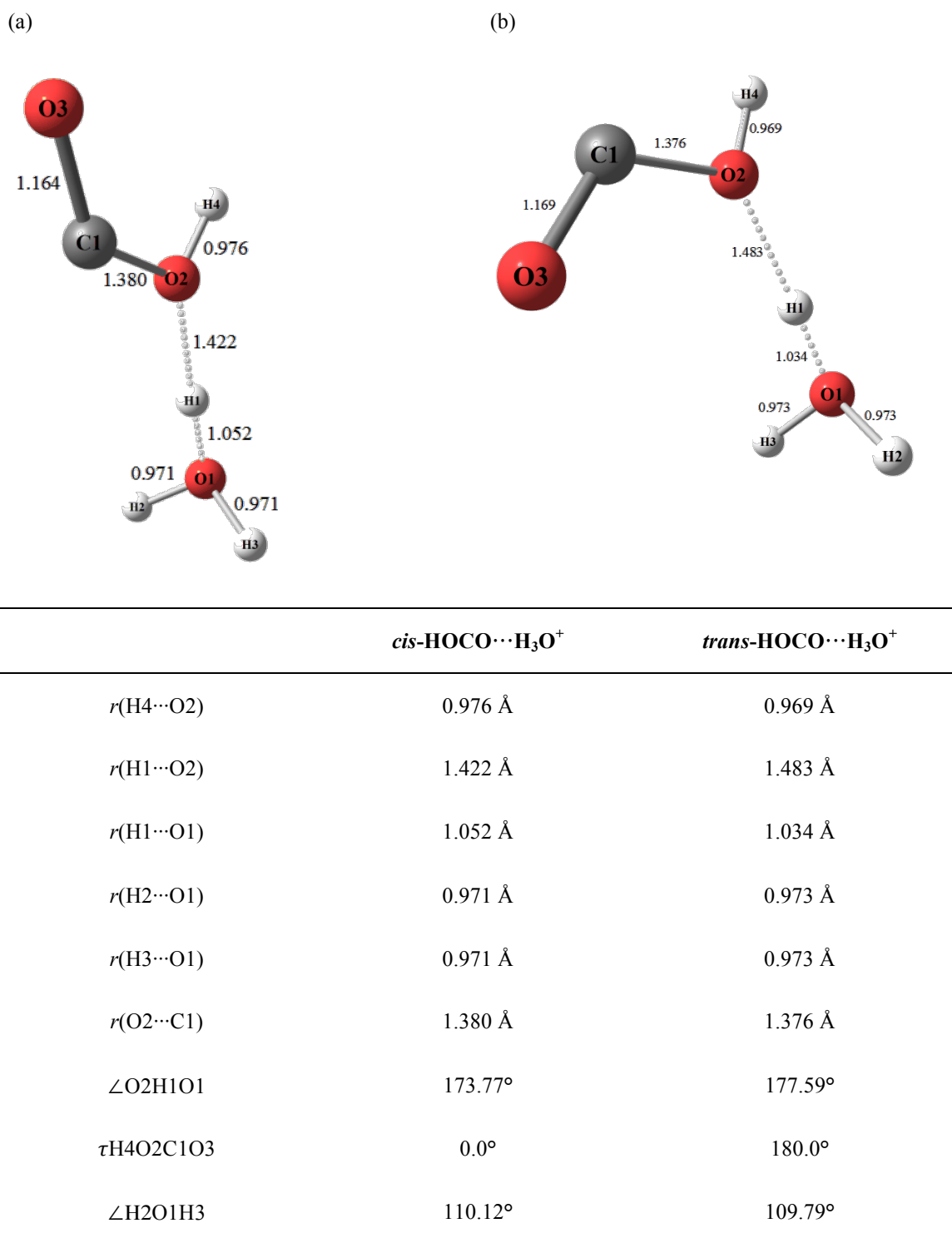
Figure A.13. Optimised geometries for (a) *cis*-HOCO⋯H$_3$O$^+$ and (b) *trans*-HOCO⋯H$_3$O$^+$. The lowest energy configuration is the *trans*-HOCO⋯H$_3$O$^+$ geometry shown in (b).